



Research Article

Heart failure detection using deep learning and Gradient Boosting classifier

Ahmad Mahmoud Ahmad ^{1a}

¹ Department of Computer Systems and Networks, Faculty of Informatics Engineering, Tishreen University, Latakia, Syria.

ahmad.m.ahmad@tishreen.edu.sy

DOI : 10.31202/ecjse.1476222

Received: 03.05.2024 Accepted: 14.01.2025

How to cite this article:

Ahmad Mahmoud Ahmad, " Heart failure detection using deep learning and Gradient Boosting classifier ", El-Cezeri Journal of Science and Engineering, Vol: 12, Iss: 1, (2025), pp.(1-8).

ORCID: "0009-0006-6571-636X".

Abstract : Heart failure (HF) is marked by a diminished capacity of the heart to effectively pump blood. Traditionally, the electrocardiogram (ECG) has served as a non-invasive diagnostic tool, gauging the heart's electrical activity and rhythm. Recent advancements have leveraged machine learning (ML) and deep learning (DL) techniques to automate the identification and classification of HF types from ECG data. This study introduces a novel deep learning architecture, blending the efficacy of a convolutional neural network (CNN) for feature extraction with an eXtreme Gradient Boosting (XGBoost) layer for final classification. The first CNN model operates on ECG segments in the time domain, while the second CNN processes the Continuous Wavelet Transform (CWT) of the same segments. This composite model offers superior automatic HF detection, particularly with 2-second ECG fragments, by capturing intricate features from both time and frequency domains. Training and testing utilize datasets from the MIT-BIH, BIDMC, and PTB Diagnostic ECG databases. Through 10-fold cross-validation, the proposed approach attains remarkable accuracy, sensitivity, and F1-score, all surpassing 99.9%. This modality represents a significant stride in DL applications for ECG diagnosis, holding promise for enhanced clinical utility.

Keywords : Convolutional neural network, deep learning, electrocardiogram, eXtreme Gradient Boosting, heart failure.

1 Introduction

Heart failure (HF) is characterized by a diminished capacity of the heart to pump blood [1]. This condition commonly arises from reduced left ventricular function and structural or functional defects within the myocardium, impeding either ventricular filling or blood ejection. Factors such as increased hemodynamic overload and ischemia-related dysfunction also contribute significantly to HF pathogenesis. Furthermore, HF stands as a principal cause of morbidity and mortality [2]. For decades, the electrocardiogram (ECG) has served as a pivotal non-invasive diagnostic tool for assessing the heart's electrical and rhythmic activity [3]. Its sensitivity to detecting HF renders it indispensable for predictive monitoring. However, cardiologists face a significant challenge in swiftly and accurately interpreting ECG signals, especially during prolonged monitoring sessions [4]. To surmount this challenge, various clinical decision support systems (CDSS) have emerged over the past decade, ranging from rudimentary rules-based systems to sophisticated algorithms rooted in machine learning (ML) and deep learning (DL) [5]–[7]. ML algorithms are primarily categorized into supervised, unsupervised, and reinforcement learning, depending on how they are initialized and trained [8]. Unsupervised learning leverages unlabeled datasets, while supervised learning relies on labeled data, where training samples and datasets are pre-classified and categorized. The Convolutional Neural Network (CNN), a type of deep learning neural network, is employed to classify data. Within a CNN, deep features are extracted from input images using convolution and pooling, computational load is reduced through downsampling, and final predictions are generated by fully connected layers [9]. Recent endeavors have focused on utilizing ML and DL methodologies to automatically identify and classify different types of HF from ECG data [10]–[12].

Asyali [13] explored the discriminatory power of nine commonly used long-term HRV measures, aiming to develop Bayesian classifiers. Sensitivity and specificity rates of 81.8% and 98.1% were achieved, respectively, depending on all normal-to-normal beat intervals' standard deviations. Jin et al. [14] proposed a wearable, cell phone-based platform capable of continuous real-time monitoring and recording of ECG data to immediately recognize abnormal cardiovascular disease (CVD) conditions. Their approach integrates an adaptive artificial neural network (ANN)-based hybrid strategy, combining patient-specific training

methods with established medical database training techniques. The results demonstrated 99% accuracy in detecting normal heartbeats and 92% accuracy in identifying premature ventricular contractions (PVCs). Chen et al. [15] utilized RR interval segments and sparse auto-encoders (SAE) to detect heart failure (HF), achieving an accuracy of 72.44%, a sensitivity of 50.93%, and a specificity of 80.93%. Masetic et al. [16] presented a method involving auto-regressive parish feature extraction and subsequent classification, resulting in 100% accuracy, sensitivity, and specificity in detecting HF. Liu and Kim [17] proposed employing Long Short-Term Memory (LSTM) and Symbolic Aggregate approximation (SAX) for categorizing heart disease using ECG signals, achieving 98.4% accuracy. Wang et al. [18] integrated a CNN module and LSTM network for HF detection, obtaining 86.42% accuracy, 74.91% sensitivity, and 91.21% specificity. Acharya et al. [18] categorized ECG signals using an 11-layer CNN, achieving 99.99% accuracy, 98.87% sensitivity, and 99.01% specificity. Cheng et al. [19] combined a 24-layer DCNN with Bidirectional LSTM for hierarchical and time-sensitive feature mining in ECG data, achieving an F1 score of 89% and an accuracy of 89.3% with 10-fold cross-validation. Padmavathi et al. [20] introduced an 11-layer CNN for HF detection, with a specificity rate of 79.30%, sensitivity of 81%, and accuracy of 80.10%. Lih et al. [21] developed a 16-layer CNN-LSTM design, achieving 97.89% specificity, 99.3% sensitivity, and 98.5% accuracy. Zhang et al. [22] enhanced the DenseNet model for HF detection using 2-second ECG fragments, achieving 89.38% sensitivity, 99.50% specificity, and 94.97% accuracy. Kusuma and Jothi [23] identified congestive heart failure (CHF) using an automated diagnosis system based on LSTM architecture and Deep CNN, achieving 99.52% accuracy. Botros et al. [24] proposed a CNN with a Support Vector Machine (SVM) layer and an integrated classification layer, achieving over 99% accuracy, sensitivity, and specificity with blindfold cross-validation. Rawi et al. [25] introduced a CNN with eXtreme Gradient Boosting (XGBoost) feature extraction, achieving 99.38% accuracy and 98.36% F1-score. Wang et al. [26] suggested a continuous wavelet transform (CWT) and CNN-based automatic ECG classification method, achieving 67.47% sensitivity, 68.76% F1-score, and 98.74% accuracy overall. Mogili and Narsimha [27] proposed a hybrid model combining a CNN for automatic ECG feature extraction with XGBoost for arrhythmia classification. Tested on the MIT-BIH Arrhythmia database, the model achieved an accuracy of 99.84% for 11 arrhythmia types and 99.69% for 5 AAMI standard classes, demonstrating its robustness with high sensitivity and specificity. Premalatha and Bai [28] developed a deep CNN-based model to classify cardiac dysrhythmia using oversampled datasets to address class imbalance. Coupled with XGBoost for structured prediction, their approach was validated on a real-time IoT dataset of elderly heart patients, achieving a recall of 100%, an F1-score of 94.8%, a precision of 98%, and an accuracy of 98%, outperforming traditional classifiers like decision trees, random forests, and SVM. Khan et al. [29] employed the MIT-BIH ARR dataset and a 1-D ResNet model, achieving an impressive accuracy of 98.63%. However, they noted that the performance of the F class still requires improvement. Al-Jibreen et al. [30] utilized the MIT-BIH Arrhythmia dataset for signal segmentation and classification using cosine wavelet transforms and a lightweight CNN with depth-wise separable convolution. Their approach achieved a classification accuracy of 99.28% for normal beats and 93.81% for abnormal beats. Majhi and Kashyap [31] proposed tree-based classifiers, Random Forest (RF) and XGBoost, for heart disease detection using three major ECG datasets: Physionet Challenge 2016, PASCAL Challenge, and MIT-BIH. Pre-processing techniques like filtering and denoising were applied, followed by feature extraction using DWT, IDWT, and EWT. SHAP analysis identified critical features impacting model predictions. Their results showed EWT with XGB achieving superior AUCs of 97.44% and 98.25% on the Physionet and MIT-BIH datasets, respectively, outperforming other feature-model combinations.

The synthesis of existing literature underscores the pivotal role of robust models and effective feature extraction in creating comprehensive feature extraction and classification systems. Recent studies have highlighted the efficacy of deep neural networks in interpreting ECG signals within both the time and time-frequency domains. However, challenges persist, particularly concerning the low sensitivity observed when employing CWT as input for CNNs.

In response to these challenges, this paper proposes a novel deep learning model that capitalizes on the strengths of CNNs for feature extraction and leverages the XGBoost classifier for end-of-model classification. The proposed model integrates two CNNs: the first processes ECG segments in the time domain, while the second operates on the CWT of the same segments. By combining features extracted from both temporal and spectral ECG data, the proposed model achieves enhanced accuracy in automatic HF detection using 2-second ECG fragments. The evaluation of the proposed model utilizes three prominent ECG databases—MIT-BIH, BIDMC, and PTB Diagnostic—for both training and testing purposes. The paper meticulously outlines the methodologies and materials employed, detailing the database descriptions, preprocessing procedures, and the proposed approach's implementation. Additionally, the results and discussion section thoroughly analyze the obtained outcomes using various performance metrics, providing valuable insights into the model's efficacy and potential areas for improvement.

2 Materials and Methods

2.1 Databases Description

Three ECG databases sourced from literature were utilized in this study:

- 1) BIDMC Database [32]: This database comprises ECG signals from 15 patients diagnosed with Congestive Heart Failure (CHF). The patients include 11 men and 4 women aged between 54 and 63 years. The signals were sampled at a

frequency of $f_s = 250\text{Hz}$.

- 2) MIT-BIH Database [33]: This dataset consists of ECG signals from 18 healthy individuals exhibiting Normal Sinus Rhythm (NSR). The cohort includes 13 women aged between 20 and 50 years and 5 men aged between 26 and 45 years. The signals were recorded using ambulatory Holter and ECG recorders, with a sampling frequency of $f_s = 360\text{Hz}$. Each segment of the signals spans approximately 20 hours and has a resolution of 250 points.
- 3) Physionet PTB Diagnostic ECG Database [34]: This database comprises 549 recordings obtained from 290 individuals aged between 17 and 87 years. Each recording contains 15 signals measured simultaneously. The sampling frequency for each signal is $f_s = 1000\text{Hz}$, and they are represented with a 16-bit resolution ranging around $\pm 16.384\text{ mV}$.

2.2 Pre-Processing

To maintain uniformity in sampling frequency across all ECG indicators, the recordings from the BIDMC database undergo initial down-sampling to 250 Hz. Subsequently, an ordinary filter with a 20-millisecond window is applied to smooth the signals. These ECG signals are then partitioned into small labeled segments, each sized 2 seconds, for subsequent processing with the CNN model. In total, the dataset comprises 500,000 segments, with half belonging to the HF group and the other half to the healthy (good) group. The overall properties are summarized in Table 1

2.3 Proposed Approach

The suggested approach is depicted in Fig. 1. The methodology begins with loading the combined dataset and subsequently implementing the requisite pre-processing steps. The deep learning model comprises two CNN models—one for processing the raw ECG signal and the other for its CWT profile. The proposed DL model synergizes the effectiveness of CNNs as feature extraction tools with the XGBoost layer for classification at the model's conclusion. Each component of the proposed model is elaborated in the following subsections. The pseudo-code of proposed approach is provided in Algorithm 1.

Algorithm 1. Algorithmic workflow for the proposed method

1. Load the combined dataset.
 2. Implement the following preprocessing steps:
 - a. Preprocess the data as required.
 - b. Segment the ECG signals into 2-second segments comprising 250 points each.
 3. Define the structure of the CNN models for feature extraction:
 - a. Construct two separate CNN models: one for processing ECG segments in the time domain and the other for segments represented in CWT form.
 - b. for each CNN model:
 - i. Initialize the CNN model.
 - ii. for each convolutional layer in the model:
 - Add convolutional layer with specified parameters.
 - iii. Add max-pooling layer with specified parameters.
 - iv. Add another convolutional layer with specified parameters.
 - v. Repeat convolutional and pooling layers as needed to achieve desired depth or feature richness.
 4. Extract deep features:
 - a. for each CNN model:
 - i. for each pooled feature map:
 - Pass through additional convolutional layers followed by pooling operations.
 - Repeat this process until desired depth or feature richness is achieved.
 5. Combine the outputs of the final pooling layers from different CNN models:
 - a. Initialize an empty array to store combined deep features.
 - b. for each CNN model:
 - i. Extract deep features obtained from the final pooling layer.
 - ii. Concatenate or average the feature vectors obtained from each model.
 - iii. Append the combined deep features to the array.
 6. Use the XGBoost layer for classification based on the deep features obtained from the combined CNN models.
 7. Train and evaluate the DL model.
 8. Optionally, fine-tune the model based on performance evaluation.
-

2.4 Continuous Wavelet Transform (CWT)

In order to improve feature extraction for efficient use of CNN model, the ECG signal can be transformed to the time-frequency domain because it is made up of various frequency components. The most widely used time-frequency research tool is CWT, which decomposes a signal over the course of time by using different wavelet functions. CWT develops and inherits the short-

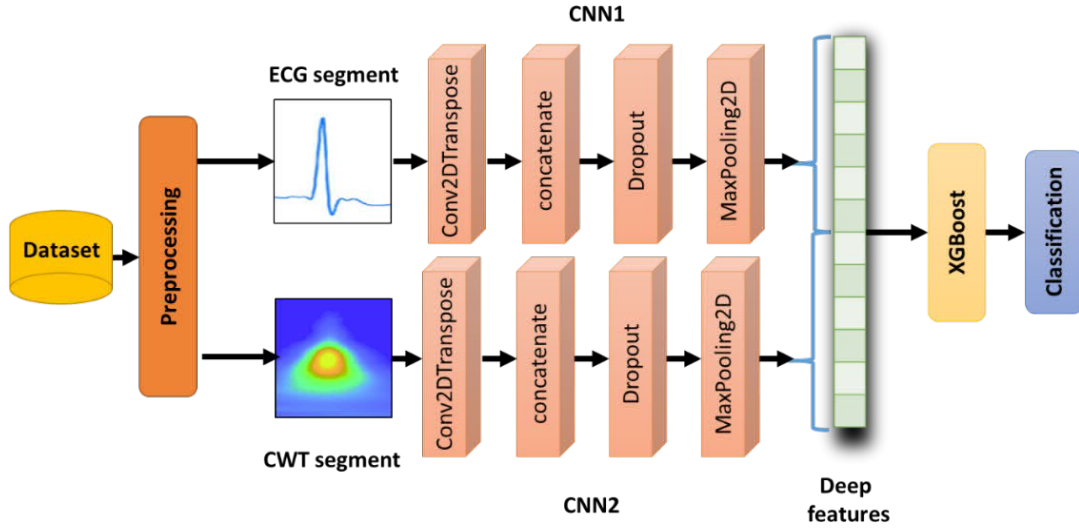


Figure 1: Proposed DL approach for ECG diagnosis

Table 1: Attribute definitions of datasets before and after pre-processing.

Dataset	Original Attributes	Pre-Processing Steps	Attributes After Pre-Processing
BIDMC [32]	- 15 patients with CHF - 11 men, 4 women - Sampling frequency: 250 Hz	- Signals partitioned into 2-second segments - Smoothing with 20 ms filter	- Down-sampled to 250 Hz - 2-second segments - 250 points/segment
MIT-BIH [33]	- 18 healthy individuals with NSR - 13 women, 5 men - Sampling frequency: 360 Hz	- Down-sampling to 250 Hz - Signals segmented into 2-second windows	- Down-sampled to 250 Hz - 2-second segments - 250 points/segment
Physionet PTB [34]	- 290 individuals, 549 recordings - Sampling frequency: 1000 Hz - 15 signals/recording - Resolution: ±16.384 mV	- Down-sampling to 250 Hz - Signals segmented into 2-second windows	- Down-sampled to 250 Hz - 2-second segments - 250 points/segment
Combined Dataset	-	-	Total: 500,000 segments (balanced)

time Fourier transform’s (STFT) localization concept. The CWT of $x(t)$ signal is computed using Eq. 1 [26]:

$$C_a(b) = \frac{1}{\sqrt{a}} \int_{-\infty}^{+\infty} x(t) \cdot \phi\left(\frac{t-b}{a}\right) dt \tag{1}$$

Where the wavelet function is $\phi(t)$, the translation parameter is b , and the scale parameter is a . To convert the scale into frequency, Eq. 2 is implemented where F_c is the mother wavelet’s center frequency and f_s is the sampling frequency of signal $x(t)$. The wave coefficients of the signal at various scales are obtained by using various CWT scale factors. A 2D scalogram of an ECG signal in the time-frequency site can be created using these wave coefficients.

$$F = \frac{F_c * f_s}{a} \tag{2}$$

2.5 Deep Feature Extraction Using CNN

In this study, two CNN models [32-34] are proposed for deep feature extraction, each consisting of three convolutional layers and one pooling layer. Given the focus on ECG segments within both the time and time-frequency domains, two separate CNN models are employed—one for processing ECG segments in the time domain and the other for segments represented in CWT form. Each CNN model receives a 2-second ECG segment comprising 250 points. Both CNN models share the same structural configuration, detailed as follows:

- 1) The first convolutional layer (CL) utilizes five 1x14 filters with a stride of 1.
- 2) The subsequent CL employs three 9x9 filters, also with a stride of 1.
- 3) The convolution stage produces three feature maps by combining various filters with the 250-point ECG signal.

- 4) Following the convolution stage, the max-pooling layer reduces the dimensions of the feature maps. It employs a pool size of two and a stride of four, enhancing the model's resilience to changes in feature position.
- 5) Subsequently, another CL is applied with ten filters of size 1x9 and a stride of 1.
- 6) After multiple convolutional and pooling layers, deep features are extracted by passing the pooled feature maps through additional convolutional layers followed by pooling operations. This process continues until the desired depth or feature richness is achieved.
- 7) Finally, the outputs of the final pooling layers from different CNN models are combined into a row of deep features. This combination can be achieved by concatenating or averaging the feature vectors obtained from each model.

2.6 XGBoost Classifier

XGBoost is a potent regression-and-classification technique [35]. Based on the gradient improving framework, XGBoost continuously enhances learner performance and efficiency by adding new decision trees to fit a value with leftover multiple iterations. In contrast to Friedman's curve boosting [36], XGBoost approximates the loss function using a Taylor expansion. The model also has better tradeoff bias and variance and typically uses fewer decision trees to achieve higher accuracy. A second-order Taylor expansion is carried out on the square loss function in XGboost, a more potent version of the Gradient Boosting Decision Tree (GBDT) algorithm, to improve accuracy. The following is the main definition of XGBoost [37]:

$$XG^{(t)} \cong \sum_{i=1}^n [g_i f_i(x_i) + \frac{1}{2} h_i f_i^2(x_i)] + \Omega(f_i) \tag{3}$$

$$\Omega(f_i) = \gamma T + \frac{1}{2} \lambda \sum_{j=1}^T \omega_j^2 \tag{4}$$

First and second-order gradient statistics for the loss function are shown here as g_i and h_i . The sample numbers are represented by n . The regression tree functions at the t -th iteration are represented by $f_t(x_i)$. The number of leaves on a tree is represented by t . L2 average of leaf scores is represented by w_{2j} . Based on the model's complexity, the regularization term $\omega(f_t)$ effectively avoids overfitting. To increase the algorithm's statement and learning speed, XGboost uses shrinking and column subsampling techniques.

2.7 Performance Metrics

Since the proposed approach is dedicated to classifying ECH into healthy or HF cases, the performance of the method is measured using the formula of accuracy (Eq. 5), sensitivity (Eq. 6) and F1-score (Eq. 7). Where True Positive (TP) refers to the number of correctly classified data as HF indicating the actual HF case; False Positive (FP): The number of incorrectly categorized data as HF that is not indicative of the correct case; True Negative (TN): The number of data classified as healthy case and indicating that actual healthy case; False Negative (FN): The number of data classified as healthy not where the actual one is HF.

$$Accuracy = \frac{TP + TN}{TP + TN + FP + FN} \tag{5}$$

$$Sensitivity = \frac{TP}{TP + FN} \tag{6}$$

$$F1 - score = \frac{2 \cdot Precision \cdot Sensitivity}{Precision + Sensitivity} \tag{7}$$

Where:

$$Precision = \frac{TP}{TP + FP} \tag{8}$$

3 Results and Discussion

The rigorous evaluation of the proposed model necessitated a meticulous approach to dataset partitioning and model assessment. Firstly, the entire dataset was stratified into three distinct subsets: the training set, employed for training the CNN model; the validation set, utilized for fine-tuning hyperparameters; and the testing set, crucial for evaluating the ultimate performance of the model. In order to ensure the robustness and reliability of the implemented approach, 75% of the 2-second healthy segments, alongside an equivalent proportion of 75% of HF segments, were randomly selected for inclusion in the training and validation

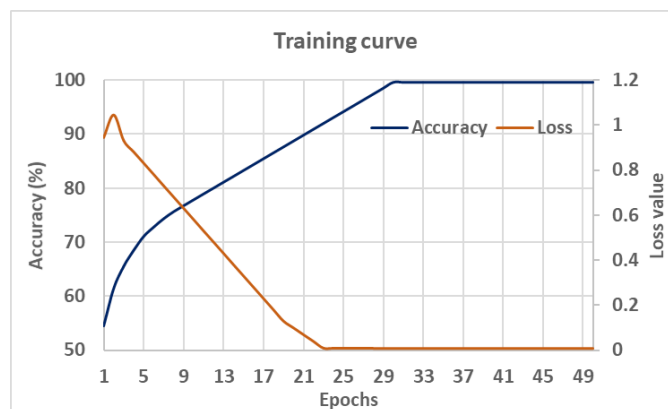


Figure 2: Training performance of CNN model.

sets. Subsequently, the validation and testing sets were constructed from the remaining data through a randomized selection process. Furthermore, to mitigate potential biases and ensure an equitable distribution of data across training and validation folds, the dataset was stratified into equal-sized folds. This stratification facilitated the proportional representation of each class within every fold, as necessitated by the principles of stratified cross-validation. In each iteration of the training process, one-fold was designated for validation while the remaining folds were utilized for model training. This iterative approach enabled comprehensive model evaluation across different subsets of the data, ensuring robustness and generalizability. Specifically, a 10-fold stratified cross-validation methodology was adopted in this study to systematically assess the performance of the proposed model. The training process of the CNN model, depicted in Figure 2, showcases the progression of model performance over epochs. Notably, the optimal performance metrics were attained after 30 epochs of training, indicating the convergence of the model towards an optimal solution. This meticulous methodology not only enhances the rigor of our experimental design but also underscores the reliability and validity of the reported findings.

As delineated in Table 2, the CNN-XGBoost hybrid model demonstrated superior performance across multiple evaluation metrics. Specifically, the hybrid model achieved an average accuracy of 99.95%, an average sensitivity of 99.96%, and an F1-score of 99.94%. Conversely, when utilizing the CNN as an independent classifier, the average accuracy, average sensitivity, and F1-score were notably lower, standing at 97.43%, 97.12%, and 92.22%, respectively.

Table 2: Ten-fold performance metrics (average \pm standard deviation) of the CNN model.

Classifier	Accuracy (%)	Sensitivity (%)	F1-score (%)
Direct CNN classifier	97.43 \pm 1.53	97.12 \pm 1.65	92.22 \pm 1.61
CNN-XGBoost (proposed method)	99.95 \pm 0.32	99.96 \pm 0.33	99.94 \pm 0.34

The reduced standard deviation observed in the CNN-XGBoost model compared to the direct CNN model across all assessment metrics, as depicted in Table 2, is indicative of greater consistency in performance. Specifically, the lower standard deviations of 1.53 for accuracy and 1.65 for sensitivity in the direct CNN models contrast with the notably diminished standard deviations of 0.32 and 0.33, respectively, in the CNN-XGBoost model. This disparity in standard deviations underscores the CNN-XGBoost model's heightened stability and robustness in classification tasks. The diminished variability suggests that the performance metrics of the CNN-XGBoost model exhibit closer proximity to the average performance across multiple evaluations, thereby implying a more reliable and consistent classification outcome. In comparing the performance of the proposed CNN-based classification techniques against existing methods, a comprehensive analysis reveals their efficacy in medical diagnostics in Table 3. Zhang et al. [22] utilized a DenseNet model trained on a combination of BIDMC, MIT-BIH, and PTB datasets, achieving an accuracy of 94.97% and a sensitivity of 89.38%. Despite using a deep network architecture, their model's performance is limited, likely due to insufficient feature extraction capabilities or imbalanced training data. Wang et al. [26] incorporated CWT with CNN for feature extraction and achieved an accuracy of 98.74%, though sensitivity remained significantly low at 67.47%. The proposed approach overcomes these limitations by combining raw ECG signals and their transformed CWT profiles, ensuring comprehensive feature extraction and improved model generalization. Botros et al. [24] proposed an SVM layer integrated with a CNN model, achieving over 99% accuracy and sensitivity on the MIT-BIH and BIDMC datasets. While their results are competitive, the lack of reported F1-scores limits a full evaluation of the model's balance between precision and recall. Khan et al. [29] applied a 1-D ResNet model on the MIT-BIH dataset, achieving 98.63% accuracy and 92.41% sensitivity. However, the performance plateaued without additional enhancements like ensemble strategies or advanced feature extraction techniques. The work of Rawi et al. [25] is particularly noteworthy, as it combines CNN and XGBoost for classification using the MIT-BIH and PTB datasets. Their model achieved an accuracy of 99.38%, a sensitivity of 98.37%, and

an F1 score of 99.11%, demonstrating the effectiveness of combining CNN-based feature extraction with XGBoost for robust classification. However, the novelty of the proposed method lies in its dual CNN architecture, where features are extracted not only from raw ECG signals but also from their corresponding CWT profiles. This dual representation enhances the richness of the extracted features, enabling the XGBoost classifier to achieve superior discriminative performance. By leveraging this enhanced feature set, the proposed approach achieves a remarkable accuracy of 99.95%, a sensitivity of 99.96%, and an F1 score of 99.96%, outperforming Rawi et al.'s results across all evaluation metrics. In comparison to Mogili and Narsimha [27], who also employed a CNN-XGBoost hybrid model on the MIT-BIH dataset with an accuracy of 99.84% and sensitivity of 92.61%, the proposed method demonstrates clear improvements. The significantly higher sensitivity and F1-score of the proposed approach are attributed to the multi-representation strategy and careful preprocessing, which unify datasets from BIDMC, MIT-BIH, and PTB. This integration creates a more diverse and balanced training set, further enhancing model generalization. Premalatha and Bai [28] proposed a CNN-XGBoost model with oversampling techniques to address class imbalance issues in a real-time IoT elderly patient dataset. Their model achieved 98% accuracy and a recall (sensitivity) of 100%. However, oversampling can introduce biases and overfitting risks, as indicated by their relatively lower F1-score of 94.8%. In contrast, the proposed method maintains a balanced performance without relying on oversampling techniques, achieving higher precision, recall, and F1-score simultaneously. Al-Jibreen et al. [30] presented a lightweight CNN model with separable convolution on the MIT-BIH Arrhythmia dataset, achieving modest results with an accuracy of 93.64% and a notably low F1-score of 53%, highlighting its limitations in handling class imbalances and complex features.

Table 3: Comparison of related work with the proposed approach.

Ref.	Method	Dataset	Accuracy	Sensitivity	F1-score
[22]	DenseNet model	BIDMC+ MIT-BIH+ PTB	94.97%	89.38%	-
[26]	CWT and CNN model	MIT-BIH	98.74%	67.47%	68.76%
[24]	SVM layer with CNN model	MIT-BIH+ BIDMC	> 99%	> 99%	-
[25]	CNN with XGBoost	MIT-BIH+ PTB	99.38%	98.37%	99.11%
[27]	CNN with XGBoost	MIT-BIH	99.84%	92.61%	95.99%
[28]	CNN-XGBoost model with oversampling	IoT Elderly Dataset	98%	100%	94.8%
[29]	1-D ResNet model	MIT-BIH	98.63%	92.41%	92.63%
[30]	Lightweight CNN with separable convolution	MIT-BIH Arrhythmia	93.64%	93.8%	53%
[31]	XGB Explainer with EWT features	MIT-BIH	98.14%	98.14%	98.10%
Proposed method	CNN-XGBoost model	BIDMC+ MIT-BIH+ PTB	99.95%	99.96%	99.96%

However, this study is limited in certain respects and it is important to acknowledge them. To begin with, our investigation scope has been confined by the lack of datasets in literature which limits the size and heterogeneity of the dataset that was employed for classification purposes. Secondly, we have used only two categories of ECG signals: normal and HF (abnormal) samples when classifying them. This dichotomous categorization framework may not be able to capture the subtleties involved in finer classifications of ECG diagnoses as a result undermining the generalizability of our proposed approach.

In future, further research efforts need to broaden these limitations through examining data consisting more diverse kinds regarding ECG abnormalities and subclasses. Moreover, such inclusion of different datasets from different sources will enable us to better model and thus understand what really happens in the ECG signals on a patient or population level. Also, broadening this classification system so as to accommodate fine specifications within various classes among other ECG subcategories would bring about an improved insight towards heart health and disease process.

4 Conclusion

The paper introduces a novel deep learning model that combines the efficacy of CNNs for feature extraction with XGBoost for classification, aiming to enhance automatic detection of HF using 2-second ECG fragments. The model consists of two CNNs: one processing ECG segments in the time domain and the other processing the CWT of the same ECG segment. By leveraging CNNs to extract deep features from both time and frequency domains, the proposed model achieves more accurate HF detection. To evaluate the model's performance, datasets from the MIT-BIH, BIDMC, and PTB Diagnostic ECG databases are utilized for training and testing. Results demonstrate that the proposed CNN-XGBoost model significantly outperforms using CNN alone as an independent classifier. Specifically, the CNN-XGBoost model achieves an impressive average accuracy of 99.95%, average sensitivity of 99.96%, and F1-score of 99.94%. In contrast, the direct utilization of CNN yields lower performance metrics, with an average accuracy of 97.43%, average sensitivity of 97.12%, and F1-score of 92.22%. Overall, the proposed model represents a promising advancement in the field of deep learning for ECG diagnosis. By combining CNNs with XGBoost, it offers a robust and accurate approach to HF detection, demonstrating its potential to enhance clinical decision-making and patient care in cardiac health.

Authors' Contributions

The paper is entirely authored by Ahmad Ahmad.

Competing Interests

The author declare that he has no conflict of interest.

References

- [1] A. A. Inamdar and A. C. Inamdar, "Heart failure: diagnosis, management and utilization," *Journal of Clinical Medicine*, vol. 5, no. 7, p. 62, Jun 2016.
- [2] P. A. H. et al., "2022 american college of cardiology/american heart association/heart failure society of america guideline for the management of heart failure: executive summary," *Journal of Cardiac Failure*, vol. 28, no. 5, pp. 810–830, May 2022.
- [3] N. R. A. H. Kashou and P. A. Noseworthy, "Ecg interpretation: clinical relevance challenges and advances," *Hearts*, vol. 2, no. 4, pp. 505–513, Nov 2021.
- [4] J. Schläpfer and H. J. Wellens, "Computer-interpreted electrocardiograms: benefits and limitations," *Journal of the American College of Cardiology*, vol. 70, no. 9, pp. 1183–1192, Aug 2017.
- [5] W. B. A. et al., "Implementing machine learning in interventional cardiology: the benefits are worth the trouble," *Frontiers in Cardiovascular Medicine*, vol. 8, p. 711401, Dec 2021.
- [6] S. M. et al., "Artificial intelligence for clinical decision support for monitoring patients in cardiovascular icus: A systematic review," *Frontiers in Medicine*, vol. 10, p. 1109411, Mar 2023.
- [7] M. A. Rahman and A. Tumian, "Variables influencing machine learning-based cardiac decision support system: A systematic literature review," *Applied Mechanics and Materials*, vol. 892, pp. 274–283, Jul 2019.
- [8] B. Mahesh, "Machine learning algorithms-a review," *International Journal of Science and Research (IJSR)*, vol. 9, no. 1, pp. 381–386, Jan 2020.
- [9] S. S. et al., "Convolutional neural networks for radiologic images: a radiologist's guide," *Radiology*, vol. 290, no. 3, pp. 590–606, Mar 2019.
- [10] J. Xue and L. Yu, "Applications of machine learning in ambulatory ecg," *Hearts*, vol. 2, no. 4, pp. 472–494, Oct 2021.
- [11] I. U. H. I. Haq and B. Xu, "Artificial intelligence in personalized cardiovascular medicine and cardiovascular imaging," *Cardiovascular Diagnosis and Therapy*, vol. 11, no. 3, p. 911, Jun 2021.
- [12] L. C. Y. Q. B. J. Schmidt and G. W. Wei, "Review of applications and challenges of quantitative systems pharmacology modeling and machine learning for heart failure," *Journal of Pharmacokinetics and Pharmacodynamics*, pp. 1–2, Feb 2022.
- [13] M. H. Asyali, "Discrimination power of long-term heart rate variability measures," in *Proceedings of the 25th Annual International Conference of the IEEE Engineering in Medicine and Biology Society (IEEE Cat. No. 03CH37439)*, vol. 1, Sep 2003, pp. 200–203.
- [14] Z. J. Y. Sun and A. C. Cheng, "Predicting cardiovascular disease from real-time electrocardiographic monitoring: An adaptive machine learning approach on a cell phone," in *2009 Annual International Conference of the IEEE Engineering in Medicine and Biology Society*, Sep 2009, pp. 6889–6892.
- [15] W. C. G. L. S. S. Q. Jiang and H. Nguyen, "A chf detection method based on deep learning with rr intervals," in *2017 39th Annual International Conference of the IEEE Engineering in Medicine and Biology Society (EMBC)*, Jul 2017, pp. 3369–3372.
- [16] Z. Masetic and A. Subasi, "Congestive heart failure detection using random forest classifier," *Computer Methods and Programs in Biomedicine*, vol. 130, pp. 54–64, Jul 2016.
- [17] M. Liu and Y. Kim, "Classification of heart diseases based on ecg signals using long short-term memory," in *2018 40th Annual International Conference of the IEEE Engineering in Medicine and Biology Society (EMBC)*, Jul 2018, pp. 2707–2710.
- [18] U. R. A. et al., "Deep convolutional neural network for the automated diagnosis of congestive heart failure using ecg signals," *Applied Intelligence*, vol. 49, pp. 16–27, Jan 2019.
- [19] J. C. Q. Zou and Y. Zhao, "Ecg signal classification based on deep cnn and blstm," *BMC Medical Informatics and Decision Making*, vol. 21, pp. 1–2, Dec 2021.
- [20] C. Padmavathi and S. V. Veenadevi, "Heart disease recognition from ecg signal using deep learning," *International Journal of Advanced Science and Technology*, vol. 29, no. 5, pp. 2303–2316, 2020, online.
- [21] O. S. L. et al., "Comprehensive electrocardiographic diagnosis based on deep learning," *Artificial Intelligence in Medicine*, vol. 103, p. 101789, Mar 2020.
- [22] Y. Zhang and M. Xia, "Application of deep neural network for congestive heart failure detection using ecg signals," in *Journal of Physics: Conference Series*, vol. 1642, no. 1, Sep 2020, p. 012021.
- [23] S. Kusuma and K. R. Jothi, "Ecg signals-based automated diagnosis of congestive heart failure using deep cnn and lstm architecture," *Biocybernetics and Biomedical Engineering*, vol. 42, no. 1, pp. 247–257, Jan 2022.
- [24] J. B. F. Mourad-Chehade and D. Laplanche, "Cnn and svm-based models for the detection of heart failure using electrocardiogram signals," *Sensors*, vol. 22, no. 23, p. 9190, Nov 2022.
- [25] A. A. R. M. K. Elbashir and A. M. Ahmed, "Ecg heartbeat classification using convxgb model," *Electronics*, vol. 11, no. 15, p. 2280, Jul 2022.
- [26] T. W. et al., "Automatic ecg classification using continuous wavelet transform and convolutional neural network," *Entropy*, vol. 23, no. 1, p. 119, Jan 2021.
- [27] R. Mogili and G. Narsimha, "Detection of cardiac arrhythmia from ecg using cnn and xgboost," *International Journal of Intelligent Engineering & Systems*, vol. 15, no. 2, 2022.
- [28] G. Premalatha and V. T. Bai, "Design and implementation of intelligent patient in-house monitoring system based on efficient xgboost-cnn approach," *Cognitive Neurodynamics*, vol. 16, no. 5, pp. 1135–1149, 2022.
- [29] F. K. X. Y. Z. Yuan and A. U. Rehman, "Ecg classification using 1-d convolutional deep residual neural network," *Plos One*, vol. 18, no. 4, p. e0284791, 2023.
- [30] A. A.-J. S. A.-A. S. Islam and A. M. Artoli, "Person identification with arrhythmic ecg signals using deep convolution neural network," *Scientific Reports*, vol. 14, no. 1, p. 4431, 2024.
- [31] B. Majhi and A. Kashyap, "Explainable ai-driven machine learning for heart disease detection using ecg signal," *Applied Soft Computing*, vol. 167, p. 112225, 2024.
- [32] D. S. B. et al., "Survival of patients with severe congestive heart failure treated with oral milrinone," *Journal of the American College of Cardiology*, vol. 7, no. 3, pp. 661–670, Mar 1986.
- [33] A. L. G. et al., "Physiobank, physiotookit, and physionet: components of a new research resource for complex physiologic signals," *Circulation*, vol. 101, no. 23, pp. e215–e220, Jun 2000.
- [34] R. B. D. Kreiseler and A. Schnabel, "Nutzung der ekg-signalbank cardiodat der ptb über das internet," *Biomed. Tech.*, vol. 40, pp. 317–318, 1995.
- [35] Y. C. C. K. H. Chang and G. J. Wu, "Application of extreme gradient boosting trees in the construction of credit risk assessment models for financial institutions," *Applied Soft Computing*, vol. 73, pp. 914–920, Dec 2018.
- [36] J. H. Friedman, "Greedy function approximation: a gradient boosting machine," *Annals of Statistics*, vol. 29, no. 5, pp. 1189–1232, Oct 2001.
- [37] W. T. et al., "Xgboost prediction model based on 3.0 t diffusion kurtosis imaging improves the diagnostic accuracy of mri birads 4 masses," *Frontiers in Oncology*, vol. 12, p. 833680, Mar 2022.

Research Article

Statistical Analysis of Wind Characteristics and Wind Energy Potential Based on Weibull Distribution in Bingol Province, Turkey

Bilal Balun^{1a}, Ömer Faruk Nemutlu^{2b}, Ali Sari^{3c}, Ahmet Benli^{2d}

¹ Department of Architecture, Bingöl University, Bingöl, Türkiye

² Department of Civil Engineering, Bingöl University, Bingöl, Türkiye

³ Department of Civil Engineering, Istanbul Technical University, Istanbul, Türkiye

ofnemutlu@bingol.edu.tr

DOI : 10.31202/ecjse.1473486

Received: 25.04.2024 Accepted: 31.05.2024

How to cite this article:

Bilal Balun, Omer Faruk Nemutlu, Ali Sari, Ahmet Benli, " Statistical Analysis of Wind Characteristic and Wind Energy Potential Based on Weibull Distribution in Bingol Province, Turkey ", El-Cezeri Journal of Science and Engineering, Vol: 12, Iss: 1, (2025), pp.(9-18).

ORCID: "0000-0003-0906-4484; ^b 0000-0001-7841-3911;; ^c 0000-0002-6888-1276; ^d 0000-0002-3557-4704.

Abstract : In this study, the statistical analysis of wind energy density and wind speed distribution parameters in Bingol province was examined using hourly wind speed data measured by the General Directorate of Meteorology between 2014 and 2017. Weibull distribution was used for statistical modeling and k and c parameters were calculated for 10 m and 30 m height. According to statistical criteria, in the wind data analysis of Bingol province, it was determined that the months with the highest potential in terms of mean wind speed and wind power densities are March, April and May. In the months when mean wind speeds are the highest, the dominant wind direction is south. As a result, it is concluded that the average monthly and annual power densities in Bingol province are about $100 W/m^2$. It is determined that the wind potential of the region can be used for small scale off-grid wind applications. The fact that the average speed is mostly higher than 4 m/s for a 30 m hub height has shown that electrical energy generation from wind energy is promising.

Keywords : Renewable energy; Wind Characteristic; Wind Energy Potential; Weibull Distribution; Wind frequency distribution

1 Introduction

In general, winds that occur because of temperature changes in the atmosphere start with the density difference or pressure variations of the points of equal height [1]. The winds formed because of these effects can be used as an alternative energy source to fossil fuels. Generating electricity using wind energy which is undoubtedly the cleanest among energy resources, provides environmental, social, and economic advantages [2]. The need to research alternative energy sources has arisen with the population and energy consumption in the world. Therefore, many scientific studies have been conducted on wind energy and wind characteristics in recent years [3]–[7]. In addition, wind characteristics are needed to investigate the effects of winds on structures. As a result of the use of fossil fuels which are the most used energy source for increasing energy consumption in today's world, carbon dioxide and greenhouse gases are released, which causes global warming by trapping the heat in the atmosphere. Therefore, the utilization of renewable energy resources has come into prominence. The potential shortages in traditional resources can be compensated by using abundant renewable resources such as wind, solar and biomass energy. Wind energy is a clean energy source, it does not cause environmental pollution and CO₂ emission. Today, wind energy is used at increasing rates day by day, although it is not at a level to close the energy gap, which is still needed and becomes a bigger problem day by day. It has been observed in many studies that regional wind energy potentials have been tried to be determined [8]–[13]. First of all, the wind characteristics of the region were revealed to determine the compatibility of the study area regions with wind energy generation. In a site where a wind power plant is planned to be established, the wind characteristics of that region should be analyzed to benefit from the wind energy potential at the maximum level and in the most efficient way. The uncontrollable nature of the wind in unstable fluctuation can lead to various problems in terms of its use as an energy source. Before deciding the wind energy potential of a region, it is necessary to determine wind characteristics such as observed frequency distributions of wind speed, wind energy density, prevailing direction of wind speed, and seasonal changes of wind [14]. Besides, wind data should be analyzed since it is not available to generate energy from every wind speed. To analyze the wind energy potential of any region, hourly wind speed and direction information must be measured for at least one year in the region, and wind measurements are generally made in the range of 10-30 meters [15]. The change in wind

speed is characterized by a probability distribution function [4]. In the studies, the wind speed frequency distribution is shown using various probability density functions such as log-normal function, gamma function, beta function, Rayleigh and Weibull distributions [5], [16], [17]. On the other hand, the two-parameter Weibull distribution and one parameter Rayleigh distribution are methods used to represent the wind distribution of many regions of the world [11], [18]–[20]. Since Rayleigh distribution is single parameter, it is less flexible than two-parameter Weibull; however, its parameters are easier to calculate. The Weibull distribution is preferred as the Rayleigh distribution is a special case of the distribution [21]. It can be said that the most suitable probability distribution for wind speeds is the Weibull distribution [3], [4], [22]–[24]. The versatile two-parameter Weibull distribution is widely used to fit the measured wind speed probability distribution. When considering the annual average wind speeds on land and sea, Turkey has more wind power potential compared to many European countries [25]. By determining the average wind speeds and wind power densities in regions with high wind energy potential, companies that will invest in this sector will be encouraged. The purpose of this study is to reveal the wind resource potential of Bingol located in eastern Turkey and to make a preliminary study to determine whether wind energy can be obtained from the region and the areas where this energy can be used. By determining the parameters (k and c) of Weibull distribution, it was ensured that wind characteristics of Bingol were revealed. For this purpose, hourly measured 4-year (2014-2017) wind speeds obtained from a meteorological wind station in Bingol were evaluated within the scope of the study.

2 Data and Methods

2.1 Data

Time series of hourly wind speed data measured from Bingol Airport station for the period between 2014 and 2017 were provided by Turkish State Meteorological Service. All wind measurements were obtained at an anemometer height of 10 m above ground level. The altitude of the airport in Bingol province located in eastern Turkey is 1063 meters. In addition to analyzing the 4-year wind speed data with the distribution form stated below, the dominant wind directions have been determined using wind roses.

2.2 Probability Distribution Model

Correct determination of the probability distribution of wind speed is a prominent factor in evaluating the wind energy potential in a region. If wind is measured over a year, it is generally seen that very strong winds are seldom, moderate, and strong winds are more likely to occur. In order to determine the wind energy potential, it is necessary to know the distribution of wind speeds at a given site. There are many methods to determine wind speed distributions. In the literature, the Weibull distribution is generally used in the statistical analysis of wind data. Wind distribution for a site is determined either by measuring or by Weibull distribution at different points and heights based on measurements. Many methods such as the method of moments, maximum likelihood estimation (MLE) and least squares are used to determine the Weibull distribution. However, it was stated that the MLE is the most effective method in determining the parameters of the Weibull distribution function [13], [26]–[28]. The probability density function expression of the Weibull distribution is as in Equation (1) and has two parameters. Where k represents the shape parameter and c represents the scale parameter. To determine these parameters, wind speed measurements made at short intervals are required be spread over a long time.

$$f(v) = \frac{k}{c} \left(\frac{v}{c}\right)^{k-1} \exp\left(-\left(\frac{v}{c}\right)^k\right) \tag{1}$$

Actually, the scale parameter c indicates how windy a considered wind position is, while the shape parameter k indicates how much the wind distribution peaks [18]. The Weibull distribution can be characterized by the cumulative distribution function $F(v)$ given in Equation (2). As well v represents the wind speed; the parameters k and c in this equation are the same as those in the probability density function. The Weibull cumulative distribution function gives the probability that the wind speed will occur less than or equal to a certain value of v .

$$F(v) = \int_0^v f(v)dv = 1 - \exp\left[-\left(\frac{v}{c}\right)^k\right] \tag{2}$$

In this study, MLE method was used to determine the k and c parameters. The k parameter of the Weibull distribution is determined iteratively as in the following equation.

$$k = \left[\frac{\sum_{i=1}^N v_i^k \ln(v_i)}{\sum_{i=1}^N v_i^k} - \frac{\sum_{i=1}^N \ln(v_i)}{N} \right]^{-1} \tag{3}$$

Once k parameter is calculated, c parameter is decided with the following equation.

$$c = \left(\frac{\sum_{i=1}^N v_i^k}{N} \right)^{\frac{1}{k}} \tag{4}$$

Table 1: Land-cover classes, Hellman coefficient (μ) values [29]

Terrain	Hellmann coefficient (α)
Lake, ocean and smooth hard ground	0.10
Foot high grass on level ground	0.15
Tall crops, hedges, and shrubs	0.20
Wooded country with many trees	0.25
Small town with some trees and shrubs	0.30
City area with tall buildings	0.40

The mean wind power density is used to determine the wind energy potential of a particular site. The mean power density per unit area for the Weibull distribution is expressed in Equation (5). Here ρ is the density of the air ($1.05\text{kg}/\text{m}^3$ for the given site), Γ is the gamma function.

$$PD_w = \frac{1}{2}\rho c^3 \Gamma\left(1 + \frac{3}{k}\right) \quad (5)$$

Following the Weibull distribution, Equations 6 and 7 are used in calculating the average wind speed and standard deviation of the wind speed, respectively. Standard deviation is a statistical measure that shows the spread of the most used data for quantitative scaled numbers relative to the mean. The low values of the standard deviation indicate that the data tends to be very close to the mean, thus it reveals the distribution of wind speed values.

$$v_m = c\Gamma\left(1 + \frac{1}{k}\right) \quad (6)$$

$$\sigma = \sqrt{c^2 \left[\Gamma\left(1 + \frac{2}{k}\right) - \Gamma^2\left(1 + \frac{1}{k}\right) \right]} \quad (7)$$

Generally, the wind speed measurements are carried out at a height of 10 m from the earth's surface. The hub's height must be at least 30 m above the ground to obtain the energy from the wind turbines. Thus, it is necessary to estimate wind speeds at higher elevations using wind speed data from lower elevations. Wind speed data measured at a certain height can be transferred to various heights using Equation (8).

$$V = V_{ref} \left(\frac{H}{H_{ref}}\right)^\mu \quad (8)$$

The symbols used in this Equation are defined as follows:

- V : Wind speed at the desired height (m/s),
- V_{ref} : Wind speed at reference altitude (m/s),
- H : Desired height (m),
- H_{ref} : Reference height (m),
- μ : Hellmann coefficient.

Hellmann coefficient (μ) values are given in Table 1 for different terrains.

3 Analysis Results and Discussion

In this study, 2014–2017 wind speed data for Bingol, Turkey were analyzed using the Weibull distribution. After deciding on Weibull parameters, mean wind speed, standard deviation and mean power density values were calculated. The wind characteristics of Bingol province were tried to be revealed by evaluating the prevailing wind directions and wind speed data according to months and years and the results obtained were examined under the headings below.

3.1 Statistical Distributions

Using the Weibull distribution, k and c parameters were determined, and mean wind speed and standard deviation values were calculated according to the relevant equations (Table 2). In Table 2; SD defines Standard Deviation, W defines Weibull Distribution. It is seen in Table 2 that Weibull k parameter varies between 1.40 and 2.59, while c parameter varies between 2.25 and 5.34 at 10 m height. At 30 m, the k parameter does not change, but the c parameter varies between 2.74 m/s and 6.51 m/s. As a result of the examination of monthly wind speeds, it was determined that the highest mean wind speeds occurred in March, April and May at 10 m height. Based on 4-year wind speeds, the months with the highest k parameter are July and August at 10 m height. In addition, the c parameter reached its highest value in March, April, May, June, July, and August. When wind speeds for 30 m height are evaluated, the highest mean wind speed, standard deviation, and the k and c parameters were realized in similar months at 10 m height. It has been observed that wind speeds, standard deviation and c parameter increase with increasing height. The lowest mean wind speeds were obtained in the winter months (November, December, January and

Table 2: Monthly mean wind speeds, standard deviations, and Weibull parameters for 10 m and 30 m

Year	Month	Mean WS (m/s) (10m)	SD (m/s) (10m)	W k (10m)	W c (10m)	Mean WS (m/s) (30m)	SD (m/s) (30m)	W k (30m)	W c (30m)
2014	Jan	1.99	1.06	2.01	2.25	2.43	1.29	2.01	2.74
2014	Feb	3.85	3.00	1.40	4.22	4.68	3.65	1.40	5.14
2014	Mar	4.56	2.18	2.14	5.15	5.55	2.66	2.14	6.27
2014	Apr	3.59	2.20	1.73	4.02	4.37	2.68	1.73	4.90
2014	May	3.04	2.06	1.66	3.40	3.71	2.51	1.66	4.15
2014	Jun	3.34	1.82	2.03	3.77	4.07	2.22	2.03	4.59
2014	July	3.47	1.90	2.07	3.92	4.23	2.31	2.07	4.78
2014	Aug	3.26	2.20	1.80	3.67	3.98	2.68	1.80	4.47
2014	Sept	3.39	1.97	1.92	3.82	4.13	2.40	1.92	4.65
2014	Oct	2.78	2.01	1.66	3.11	3.38	2.45	1.66	3.79
2014	Nov	2.25	1.38	1.77	2.53	2.74	1.69	1.77	3.08
2014	Dec	2.41	1.23	2.09	2.72	2.94	1.50	2.09	3.31
2015	Jan	2.75	2.14	1.47	3.04	3.35	2.61	1.47	3.70
2015	Feb	2.94	1.70	1.70	3.29	3.58	2.07	1.70	4.01
2015	Mar	3.78	2.24	1.87	4.26	4.60	2.73	1.87	5.19
2015	April	4.17	2.02	2.12	4.71	5.09	2.46	2.12	5.74
2015	May	3.95	1.98	2.01	4.45	4.81	2.42	2.01	5.43
2015	Jun	4.41	2.03	2.33	4.98	5.38	2.47	2.33	6.07
2015	July	4.14	2.04	2.08	4.67	5.04	2.48	2.08	5.69
2015	Aug	4.00	1.87	2.28	4.52	4.88	2.28	2.28	5.51
2015	Sep	3.78	1.99	2.02	4.27	4.61	2.43	2.02	5.20
2015	Oct	2.97	1.36	2.35	3.36	3.62	1.66	2.35	4.09
2015	Nov	2.98	1.56	2.04	3.37	3.63	1.90	2.04	4.10
2015	Dec	2.81	1.81	1.69	3.15	3.43	2.21	1.69	3.84
2016	Jan	2.29	1.06	1.87	2.58	2.79	1.29	1.87	3.14
2016	Feb	2.32	1.23	1.96	2.61	2.82	1.50	1.96	3.19
2016	Mar	4.07	2.55	1.77	4.58	4.97	3.10	1.77	5.58
2016	Apr	4.20	2.01	2.14	4.74	5.12	2.45	2.14	5.78
2016	May	4.62	2.50	1.97	5.21	5.63	3.05	1.97	6.35
2016	June	4.62	1.81	2.43	5.21	5.63	2.21	2.43	6.35
2016	July	4.21	1.58	2.51	4.75	5.13	1.93	2.51	5.78
2016	Aug	3.53	1.32	2.17	3.98	4.30	1.61	2.17	4.85
2016	Sep	4.08	1.94	2.14	4.60	4.97	2.36	2.14	5.61
2016	Oct	3.18	1.87	1.93	3.59	3.88	2.28	1.93	4.37
2016	Nov	3.59	2.80	1.45	3.96	4.38	3.41	1.45	4.82
2016	Dec	2.55	1.74	1.66	2.85	3.11	2.12	1.66	3.48
2017	Jan	2.81	2.05	1.51	3.11	3.42	2.50	1.51	3.80
2017	Feb	3.19	2.25	1.56	3.55	3.89	2.74	1.56	4.33
2017	Mar	3.92	2.23	1.69	4.39	4.77	2.72	1.69	5.35
2017	Apr	4.70	2.47	2.01	5.31	5.73	3.01	2.01	6.47
2017	May	4.73	2.24	2.29	5.34	5.76	2.73	2.29	6.51
2017	Jun	4.13	1.90	2.34	4.67	5.04	2.31	2.34	5.69
2017	July	4.07	1.96	2.20	4.60	4.96	2.39	2.20	5.60
2017	Aug	4.39	1.84	2.59	4.95	5.35	2.25	2.59	6.03
2017	Sep	3.46	1.84	2.02	3.91	4.22	2.24	2.02	4.76
2017	Oct	3.99	2.09	2.01	4.50	4.86	2.55	2.01	5.48
2017	Nov	2.25	1.34	1.85	2.54	2.74	1.63	1.85	3.09
2017	Dec	2.23	1.30	1.83	2.51	2.71	1.59	1.83	3.06

Table 3: Annual mean wind speeds, standard deviations and Weibull parameters for 10 m and 30 m

Year	Mean WS (m/s) (10 m)	SD (10 m)	W k (10 m)	W c (10 m)	Mean WS (m/s) (30 m)	SD (30 m)	W k (30 m)	W c (30 m)
2014	3.13	1.92	1.68	3.51	3.82	2.34	1.68	4.27
2015	3.61	1.99	1.88	4.07	4.40	2.43	1.88	4.96
2016	3.77	2.05	1.91	4.25	4.59	2.50	1.91	5.18
2017	3.72	2.14	1.80	4.19	4.54	2.61	1.80	5.10
All data	3.59	2.05	1.81	4.03	4.37	2.50	1.81	4.91

February). Considering the 4-year wind data, the highest mean wind speed was realized in May 2017 with 5.76 m/s at 30 m height. However, the lowest mean wind speed was recorded in January 2014 with 2.43 m/s at 30 m height.

It is seen from Table 3 the yearly mean wind speeds range from 3.13 m/s to 3.77 m/s at 10 m height. (In Table 2; SD defines Standart Deviation, W defines Weibull Distribution.) In addition to this, the average of the standard deviation from 2014 to 2017 is 2.05. At 30 m height, the mean wind speed reaches 4.37 m/s over a period of 4 years. These results show that at higher hub height, the higher the wind speed, standard deviation and scale parameters are obtained. It was also determined that the shape parameter has lower values than the scale parameter at different hub heights. The averages of the k and c parameters required to calculate the energy generated from the wind over a 4-year period are respectively 1.81 and 4.03 for 10 m height, 1.81 and 4.91 for 30 m height, respectively.

The wind speed probability density function obtained by the Weibull distribution of wind speeds on an annual basis using the MLE method is given in Figures 3-7. As the hub heights increase, the peaks of the Weibull distribution decrease in all years

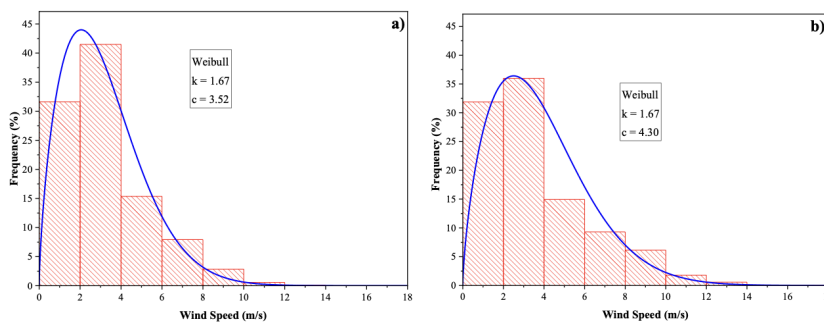


Figure 1: 2014 wind speed profile; a) 10m, b) 30m

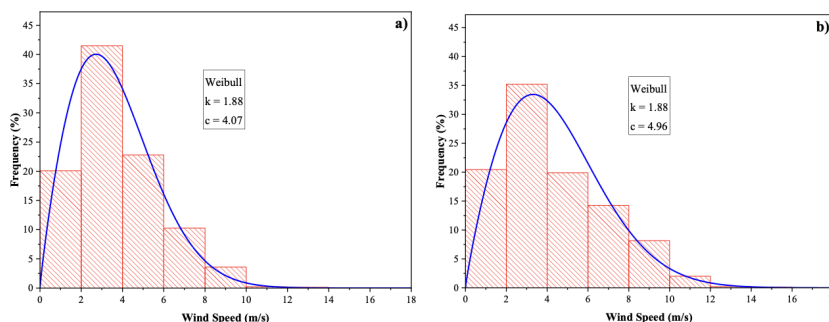


Figure 2: 2015 wind speed profile; a) 10m, b) 30m

and spread towards increasing speed. It can also be said for the determined wind speed ranges, the distributions of wind speeds and Weibull distribution coincide. From the figures, wind speeds are generally between 0 and 4 m/s for 10 m hub height. When the height of 30 m is reached, it has been determined that the frequency of wind dispersion is maintained up to 6 m/s. When all wind speed data are considered at 10 m hub height, it has been determined that the most wind data is around 2 m/s and corresponds to approximately 40% of the data. For a height of 30 m, it was found that this value was around 3 m/s and showed a distribution of approximately 35%.

3.2 Wind Roses

Monthly and annual wind rose charts help explain the variation in wind direction each month and year as shown in the figures below. The monthly wind rose charts obtained from 10 m height in Figure 6 demonstrate that most wind flows from the South during the spring months when average wind speeds are the highest. When all wind data from 2014 to 2017 are examined-again, most of the winds flow from the South (about %14) (Figure 7). Simply, it can be concluded that the prevailing wind direction in the study area is south. It is observed that the winds are generally flowing from the south in the spring, which is the windy season, and that there is no uniform distribution in the other months. Wind roses were generated with WRPlot Software. WRPlot software provides a visual representation of how the wind direction changes in certain periods.

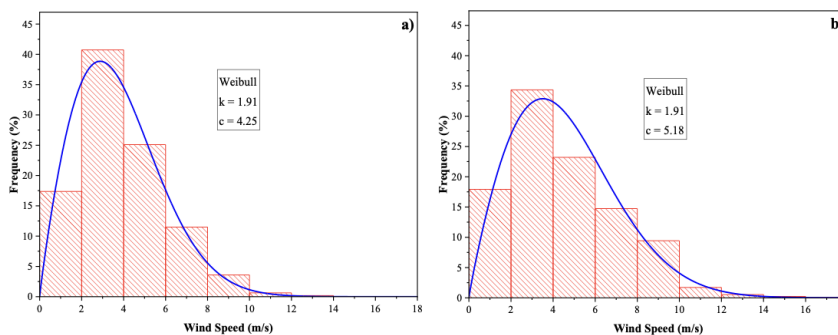


Figure 3: 2016 wind speed profile; a) 10m, b) 30m

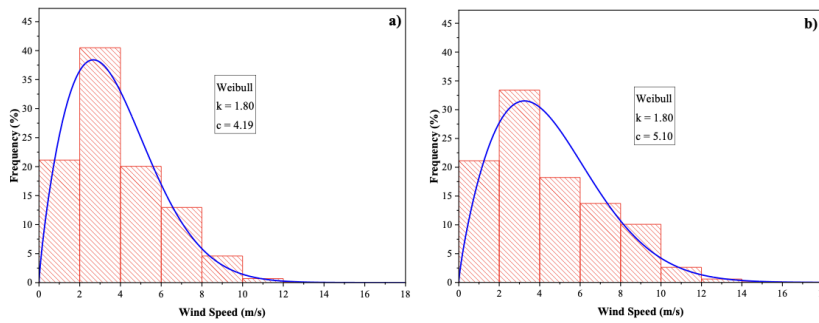


Figure 4: 2017 wind speed profile; a) 10m, b) 30m

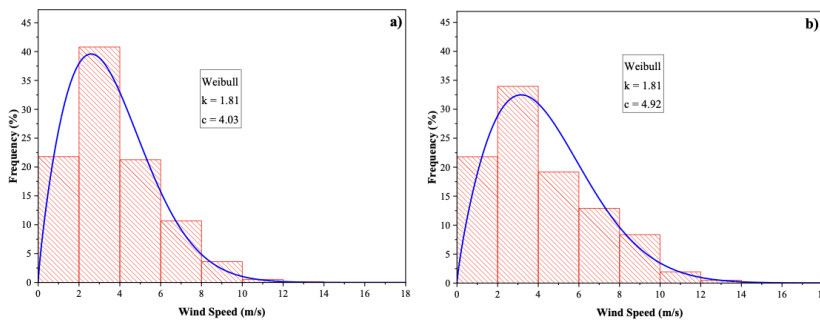


Figure 5: 2014 to 2017 wind speed profile; a) 10m, b) 30m

3.3 Wind Power Density

Calculating wind power density (PD) is an important step in evaluating wind energy potential. The annual values of the Weibull power density (PD) are given in Table 4. In this study, wind power density values are evaluated for 30 m. According to the Weibull distribution, the highest wind power density was achieved as 105.04 W/m^2 in 2017 and the lowest power density as 68.22 W/m^2 in 2014. In Bingol province, the average wind power density was approximately 90 W/m^2 in a period of 4 years.

3.4 Evaluation of Wind Data

In Figure 8, the mean wind speeds and wind power densities of Bingol province by months are shown. In the Bingol region, the highest wind power density and mean power speeds is observed in the spring months, while the lowest is observed in the winter months. Generally, both mean wind speeds and wind power densities are high in the spring months. Mean wind speeds in March, April, May, and June are about 5 m/s at 30 m height. The lowest monthly mean wind speeds were obtained in January and February for 10 m and 30 m altitude, respectively, 2.5 m/s and 3.0 m/s. The average wind power density is around 135 W/m^2 in March and April. Accordingly, it can be said that spring months have higher energy potential than other months in terms of average wind speed and wind power density. However, in addition to the mean wind speeds and wind power densities, the data distribution is also important in wind energy. International standards have classified the energy that wind turbines can generate over wind speed (m/s) and power density (W/m^2) [30]. Considering the monthly and annual wind power densities and mean wind speeds the energy potential of region is in Class 1 (Tables 4 and 5) (Fig 8). As a result of these data it was found that wind potential of the region can be used for low-capacity wind turbines in rural and small communities.

The cumulative distribution function shows the ratio of the wind speed when it is below a certain wind speed. The cumulative distribution function can also be used to predict the wind is within a certain speed range [31]. Figure 9 shows the cumulative percentages of monthly wind speeds. The cumulative distribution function in Figure 9 shows that approximately 90% of the wind speed recorded in March, April, May and June is below 8.5 m/s in December and January, and below 4.5 m/s.

In order to determine the wind energy potential of a region, it is necessary to determine the wind speed distribution [32], [33]. Figure 10 shows wind speed Weibull distributions and cumulative probability distributions derived from the measured hourly time-series data of Bingol (2014 to 2017). The cumulative distribution shows that approximately 90% of the wind speed recorded

Table 4: Annual PDw based on Weibull distribution at 30 m height

Years	2014	2015	2016	2017
PDw (W/m^2)	68.22	91.02	101.87	105.04

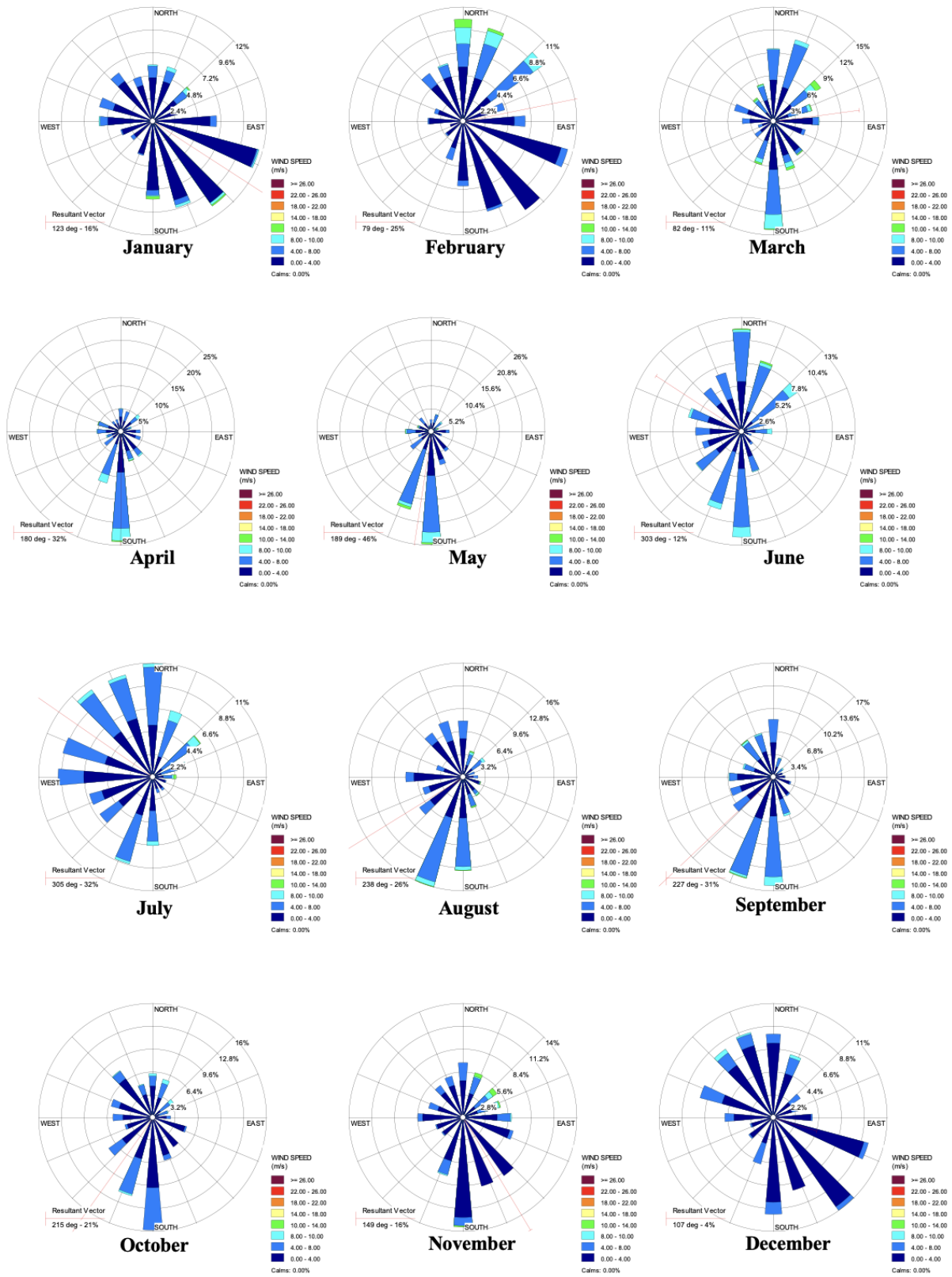


Figure 6: Monthly wind roses 2014 to 2017

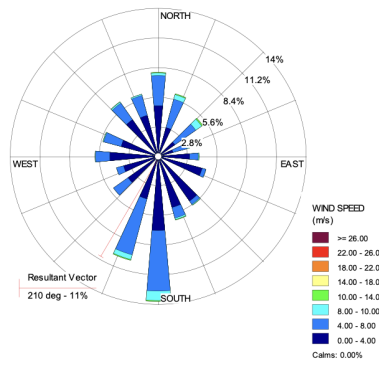


Figure 7: Average Wind rose 2014 to 2017

Table 5: Annual PDw based on Weibull distribution at 30 m height

Wind Power Class	m/s(10m)	W/m ² (10m)	m/s(30m)	W/m ² (30m)
1	0-4.4	0-100	0-5.1	0-160
2	4.4-5.1	100-150	5.1-5.9	160-240
3	5.1-5.6	150-200	5.9-6.5	240-320
4	5.6-6.0	200-250	6.5-7.0	320-400
5	6.0-6.4	250-300	7.0-7.4	400-480
6	6.4-7.0	300-400	7.4-8.2	480-640
7	> 7.0	>400	8.2-11	640-1600

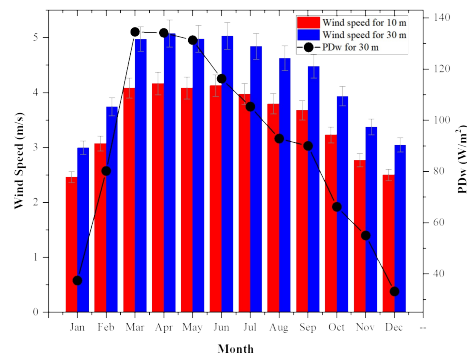


Figure 8: Monthly average wind speeds and PDw

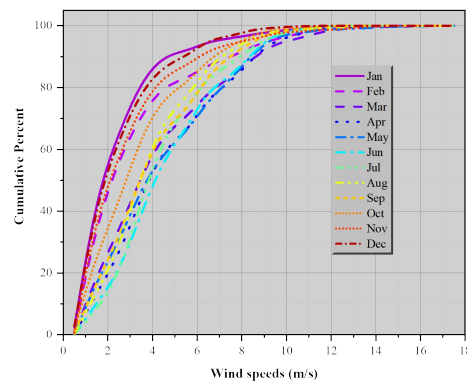


Figure 9: 2014 to 2017 cumulative distribution at 30 m height (hourly average)

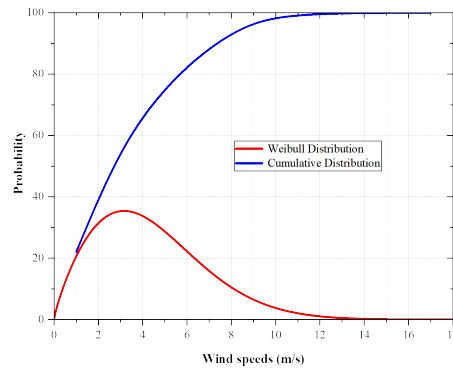


Figure 10: Wind speed Weibull distributions and cumulative probability distributions, derived from the measured hourly time-series data of Bingöl (2014 to 2017)

in 2014 to 2017 is below 6.5 m/s. When 4-year wind data were examined, it was determined that approximately 35% of the Weibull distribution was composed of 2.5 m/s wind speed.

To promote renewable energy, examining only the wind energy potential of a region may be insufficient. For this reason, renewable energy studies carried out in a region should be evaluated together in a comprehensive manner [34], [35]. It may be useful to make a solar energy potential assessment for Bingöl province in the future.

4 Conclusion

In this paper, hourly long-term wind speed data of Bingöl province between 2014 and 2017 were analyzed statistically. Probability density distributions are derived from long-term wind speed data and distribution parameters are defined. The dominant wind directions and energy potential of the region were determined, and the data obtained are given below.

- In this study, where the wind characteristics of Bingöl province were examined with the Weibull distribution, when all wind data were taken into consideration, it was determined that the shape parameter (k) and scale parameter (c) were 1.81 and 4.03 for 10 m height, 1.81 and 4.91 for 30 m respectively.
- Mean wind speeds from 2014 to 2017 were 3.59 m/s and 4.37 m/s for 10 m and 30 m height, respectively.
- Mean wind speeds reached their highest value with about 5.0 m/s in March, April, May and June. The lowest wind speeds were in the winter months.
- In the spring months when average wind speeds are the highest, the prevailing wind direction is south
- These results show that the potential of generating electricity from wind in general is low in Bingöl. As a result, it has been concluded that since the average monthly and annual power densities in Bingöl province are 100 W/m^2 , it is not possible to directly support the electrical grid by wind energy systems, and it can be used particularly for electrical applications that do not require low power density in rural areas. The fact that the average speed is mostly higher than 4 m/s for 30 m hub height has shown that electrical energy generation from wind energy is promising. However, this study can help to encourage the use of small-scale wind energy projects in Bingöl, especially in applications that require electricity, such as the use of internet infrastructure, traffic signs, street lighting, charging stations and irrigation in the rural areas.
- It also shows that the hub heights of the wind turbines to be installed should be as high as possible.
- It is recommended to take long-term measurements at different heights in different regions to make a better decision about the wind characteristics and wind energy potential of the province.
- In this way, the average wind speeds and wind power densities in regions with high wind energy potential will be determined and companies that will invest in this sector will be encouraged.

Acknowledgments

The authors greatly thank Directorate General for State Hydraulic Works for their support in conducting the characterization.

Authors' Contributions

In this study, Authors contributed equally to the study.

Competing Interests

The authors declare that they have no conflict of interest.

References

- [1] A. Kareem and Y. Tamura, *Advanced structural wind engineering*. Springer, 2013.
- [2] M. Monfared, H. Rastegar, and H. Kojabadi, "A new strategy for wind speed forecasting using artificial intelligent methods," *Renewable Energy*, vol. 34, no. 3, pp. 845–848, 2009.
- [3] J. Chadee and C. Sharma, "Wind speed distributions: a new catalogue of defined models," *Wind Engineering*, vol. 25, no. 6, pp. 319–337, 2001.
- [4] P. Wais, "A review of weibull functions in wind sector," *Renewable and Sustainable Energy Reviews*, vol. 70, pp. 1099–1107, 2017.
- [5] H. Li and F. Zhang, "Summary on wind speed distribution and its parameter estimation," *Proceedings Advanced Materials Research*, pp. 689–693.
- [6] M. Sedghi, S. Hannani, and M. Boroushaki, "Estimation of weibull parameters for wind energy application in iran's cities," *Wind Structures*, vol. 21, no. 2, pp. 203–221, 2015.
- [7] C. Seshaiyah and K. Sukkiramathi, "A mathematical model to estimate the wind power using three parameter weibull distribution," *Wind Structures*, vol. 22, no. 4, pp. 393–408, 2016.
- [8] K. Ulgen and A. Hepbasli, "Determination of weibull parameters for wind energy analysis of izmir, turkey," *International Journal of Energy Research*, vol. 26, no. 6, pp. 495–506, 2002.
- [9] A. Celik, "A statistical analysis of wind power density based on the weibull and rayleigh models at the southern region of turkey," *Renewable Energy*, vol. 29, no. 4, pp. 593–604, 2004.
- [10] E. K. Akpınar and S. Akpınar, "Determination of the wind energy potential for maden-elazig, turkey," *Energy Conversion Management*, vol. 45, no. 18–19, pp. 2901–2914, 2004.
- [11] E. Akpınar and N. Balpetek, "Statistical analysis of wind energy potential of elazig province according to weibull and rayleigh distributions," *Journal of the Faculty of Engineering Architecture of Gazi University*, vol. 34, no. 1, pp. 569–580, 2019.
- [12] F. Mahmood, A. Resen, and A. Khamees, "Wind characteristic analysis based on weibull distribution of al-salman site, iraq," *Energy Reports*, vol. 6, pp. 79–87, 2020.
- [13] B. Safari and J. Gasore, "A statistical investigation of wind characteristics and wind energy potential based on the weibull and rayleigh models in rwanda," *Renewable Energy*, vol. 35, no. 12, pp. 2874–2880, 2010.
- [14] R. Mouangue, M. Kazet, A. Kuitche, and J.-M. Ndjaka, "Influence of the determination methods of k and c parameters on the ability of weibull distribution to suitably estimate wind potential and electric energy," *International Journal of Renewable Energy*, vol. 3, no. 2, 2014.
- [15] Y. Kaplan, "The evaluating of wind energy potential of osmaniye region with using weibull and rayleigh distributions," *Süleyman Demirel University Journal of Natural Applied Sciences*, vol. 20, no. 1, pp. 62–71, 2016.
- [16] O. Alavi, A. Sedaghat, and A. Mostafaeipour, "Sensitivity analysis of different wind speed distribution models with actual and truncated wind data: A case study for kerman, iran," *Energy Conversion and Management*, vol. 120, pp. 51–61, 2016.
- [17] J. Wang, X. Huang, Q. Li, and X. Ma, "Comparison of seven methods for determining the optimal statistical distribution parameters: A case study of wind energy assessment in the large-scale wind farms of china," *Energy*, vol. 164, pp. 432–448, 2018.
- [18] S. Ali, S. Lee, and C. Jang, "Statistical analysis of wind characteristics using weibull and rayleigh distributions in deokjeok-do island - incheon, south korea," *Renewable Energy*, vol. 123, pp. 652–663, 2018.
- [19] T. Burton, D. Sharpe, N. Jenkins, and E. Bossanyi, *Wind energy handbook*. Wiley Online Library, 2001.
- [20] J. Seguro and T. Lambert, "Modern estimation of the parameters of the weibull wind speed distribution for wind energy analysis," *Journal of Wind Engineering and Industrial Aerodynamics*, vol. 85, no. 1, pp. 75–84, 2000.
- [21] S. Kwon, "Uncertainty analysis of wind energy potential assessment," *Applied Energy*, vol. 87, no. 3, pp. 856–865, 2010.
- [22] S. Mathew and K. Pandey, "Analysis of wind regimes for energy estimation," *Renewable Energy*, vol. 25, no. 3, pp. 381–399, 2002.
- [23] K. Doğanşahin, A. Uslu, and B. Kekezoğlu, "İki bileşenli weibull dağılımı ile rüzgâr hızı olasılık dağılımlarının modellenmesi," *Avrupa Bilim ve Teknoloji Dergisi*, vol. 15, pp. 315–326, 2019.
- [24] A. Gungor, M. Gokcek, H. Ucar, E. Arabaci, and A. Akyuz, "Analysis of wind energy potential and weibull parameter estimation methods: a case study from turkey," *International Journal of Environmental Science and Technology*, vol. 17, no. 2, pp. 1011–1020, 2020.
- [25] Y. Kaplan, "Overview of wind energy in the world and assessment of current wind energy policies in turkey," *Renewable Sustainable Energy Reviews*, vol. 43, pp. 562–568, 2015.
- [26] P. Ramirez and J. Carta, "Influence of the data sampling interval in the estimation of the parameters of the weibull wind speed probability density distribution: a case study," *Energy Conversion and Management*, vol. 46, no. 15–16, pp. 2419–2438, 2005.
- [27] D. Weisser, "A wind energy analysis of grenada: an estimation using the 'weibull' density function," *Renewable Energy*, vol. 28, no. 11, pp. 1803–1812, 2003.
- [28] T. Chang, "Performance comparison of six numerical methods in estimating weibull parameters for wind energy application," *Applied Energy*, vol. 88, no. 1, pp. 272–282, 2011.
- [29] M. Patel, *Wind and solar power systems: design, analysis, and operation*. CRC Press, Taylor and Francis Group, FL, USA, 2005.
- [30] M. Baloch, S. Abro, G. Kaloi, N. Mirjat, S. Tahir, M. Nadeem, M. Gul, Z. Memon, and M. Kumar, "A research on electricity generation from wind corridors of pakistan (two provinces): A technical proposal for remote zones," *Sustainability-Basel*, vol. 9, no. 9, 2017.
- [31] G. Nage, "Analysis of wind speed distribution: Comparative study of weibull to rayleigh probability density function; a case of two sites in ethiopia," *American Journal of Modern Energy*, vol. 2, no. 3, pp. 10–16, 2016.
- [32] E. Dokur and M. Kurban, "Wind speed potential analysis based on weibull distribution," *Balkan Journal of Electrical Computer Engineering*, vol. 3, pp. 231–235, 2015.
- [33] O. Oral, M. İnce, B. Aylak, and M. Özdemir, "Estimation of wind speed probability distribution parameters by using four different metaheuristic algorithms," *ECJSE*, vol. 9, no. 4, pp. 1342–1362, 2022.
- [34] Y. Alcan, M. Demir, and S. Duman, "Sinop İlinin güneş enerjisinden elektrik Üretim potansiyelinin Ülkemiz ve almanya İle karşılaştırarak İncelenmesi," *ECJSE*, vol. 5, no. 1, pp. 35–44, 2018.
- [35] F. Tan and S. Shojaei, "Past to present: Solar chimney power technologies," *ECJSE*, vol. 6, no. 1, pp. 220–235, 2019.

Research Article

Review of Blast Injury and Developing Threshold Values for Human Injury

Ömer Faruk Zırh^{1a}, Ali Sari^{1b}

¹ Department of Civil Engineering, Istanbul Technical University, Istanbul, Türkiye

zirh19@itu.edu.tr

DOI : 10.31202/ecjse.1514208

Received: 10.07.2024 Accepted: 27.08.2024

How to cite this article:

Zırh OF, Sari A, "Review of Blast Injury and Developing Threshold Values for Human Injury ", El-Cezeri Journal of Science and Engineering, Vol: 12, Iss: 1, (2025), pp.(19-35).

ORCID: ^a00009-0006-0194-1031; ^b 00000-0002-6888-1276.

Abstract : In today's world, explosions frequently occur in terrorist bombings, industrial and manufacturing sectors, and daily life. The blast waves generated by explosions subject structures and the human body to significant blast loads. These blast loads can cause deadly structural collapses, and serious injuries or fatal outcomes can occur in various parts of the human body, such as the brain, lungs, heart, auditory system, eyes, abdominal region and musculoskeletal system due to the impact of the blast load. This article initially discusses the blast wave and its characteristics (peak pressure and duration) as well as the parameters of the blast wave, which have been related to injuries occurring in the major organs of the human body. Subsequently, the effects of blast loading have been quantitatively documented under the headings of blast injuries, types and mechanisms of blast injuries, and the effects of explosions on the human body, correlating the severity of injuries with nearly all major systems of the human body. As a result, various injury scaling criteria have been carefully compiled to determine thresholds for major organ injuries, and ultimately, limit blast pressure values for different parts of the human body (lung, ear and head) have been proposed.

Keywords : Blast Injury, Blast Wave, Explosion, Injury Criteria, Injury Scaling

1 Introduction

Explosions occur when a liquid or solid substance instantaneously transitions to the gas phase, generating energy in the form of sound, heat, light, and pressure. These explosions can result in blast injuries or fatalities. Such injuries are generally caused by the detonation of high-order or low-order explosives. Examples of high-order explosives include C-4, Semtex, dynamite, ammonium nitrate, and trinitrotoluene, whereas low-order explosives include Molotov cocktails, pipe bombs and gunpowder. High-order explosives generate supersonic explosions that can move at speeds of up to 8000 meters per second and bringing about pressures up to 30000 times the atmospheric pressure [1]. As the name suggests, low-order explosives have less destructive power compared to high-order explosives but can cause severe explosions when combined with secondary agents (such as metal fragments, nails etc.).

The explosion effects data presented in the UFC 3-340-02 [2] guide largely pertain to the blast pressures of open spherical TNT explosives. Those data can be potentially extended to contain other explosive materials by associating the 'effective explosive weight' of these materials to the explosive energy of an equivalent weight of TNT. In addition to energy output, other factors can influence the equivalence of the material compared to TNT. These factors contain the shape of the material (round, flat, square etc.), the quantity of explosive substance, whether the explosion occurs in an open or enclosed space, and the pressure range considered (close, medium, or long distances). For blast-resistant design, the effects of the energy output of an explosive material of a particular shape compared to that of similarly shaped TNT can be indicated as a function of the blast heat of various materials as follows [2]:

$$W_E = \frac{H_{EXP}^d}{H_{TNT}^d} W_{EXP} \quad (1)$$

where H_{EXP}^d : heat of detonation of explosive in question , H_{TNT}^d : heat of detonation of TNT, W_{EXP} : weight of the explosive in question , W_E : effective charge weight . In conclusion, the characteristics of blast waves resulting from condensed high-energy explosives are apparently similar to those produced by TNT, and the blast parameters of other explosives can be determined

using explosives that have blast effects similar to those of spherical TNT. This is referred to as the TNT equivalent of explosives. Generally, the equivalent factor is utilized in relative comparisons, and the data is obtained by comparing the air blast data of different high-energy explosives. Table 6 in explosion physics part of the Wang and Jiang’s book provides a list of TNT equivalent factors for computing impulse and overpressure for the explosion of various explosives in an infinite air environment [3]:

1.1 Blast Wave

The pressure or blast wave generated by the sudden release of energy into the atmosphere is one of the most crucial aspects in blast-resistant design. The shape and magnitude of the blast wave, propagating outward in all directions from the explosion source at sonic or supersonic speeds, depend on the nature of the energy release and the distance from the epicenter of the explosion (standoff distance). The blast wave has two distinct characteristic types, namely shock waves and pressure waves, and their typical pressure-time curves are shown in Figure 1 below [4]:

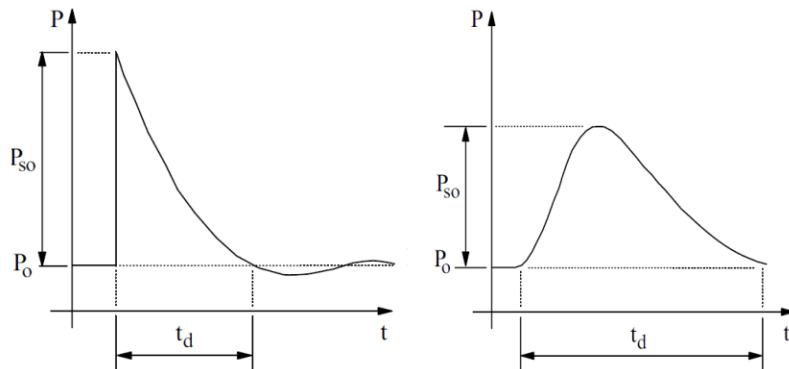


Figure 1: Characteristic types of blast wave: shock wave (left) and pressure wave (right) [4]

Examining the blast pressure-time curve of the shock wave reveals that this wave initially peaks instantaneously at a value above the ambient atmospheric conditions, and then gradually falls to the ambient pressure level with highly damped oscillations. Consequently, it can be stated that the positive phase of the blast wave is followed by a negative phase pressure wave. Looking at the blast pressure-time curve of the pressure wave, it can be observed that the pressure increases over time to reach a peak value, followed by a decrease in pressure over time. It is necessary to define the fundamental parameters of the blast wave as components of the blast load on building elements. These are defined as the maximum pressure for the positive phase, P_{so} , the duration of the positive phase, t_d , and the associated positive impulse, I_o^+ ; and for the negative phase; the maximum pressure, P_{so}^- , the duration of the negative phase, t_d^- , and the associated negative impulse, I_o^- [4]. The areas under the pressure-time curves represent the impulse value of the explosion.

$$I_o = \int P(t)dt \tag{2}$$

For a triangular wave : $I_o = 0.50P_{so}t_d$, For a half-sine wave : $I_o = 0.64P_{so}t_d$. For an exponentially decaying shock wave : $I_o = cP_{so}t_d$, Here, $P(t)$ represents the function of the variation of overpressure with time, P_{so} : the maximum lateral overpressure value, t_d : the duration of the positive phase, c : value ranging between 0.2 and 0.5 depending on P_{so} . In addition, the blast waves resulting from explosions exhibit very high strain rates in the range of 10^2 to 10^5 s^{-1} . The high and sudden loading rate is critical as it changes the expected damage mechanisms for various structural elements and the dynamic mechanical properties of the target structures, as well as being of paramount importance for human injuries. Figure 2 illustrates the ranges within which strain rates vary for different types of loading conditions [5].

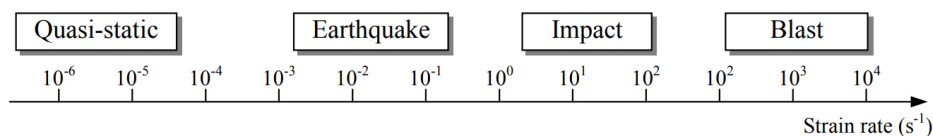


Figure 2: Variation of strain rate for different types of loading [5]

Also, the impulse and peak pressure values on the structure change with the standoff distance, R (distance from the explosive). For a spherical TNT explosions, the positive phase pressures, durations, impulses and other parameters of this shock environment vary with the scaled distance (Figure 3) [2].

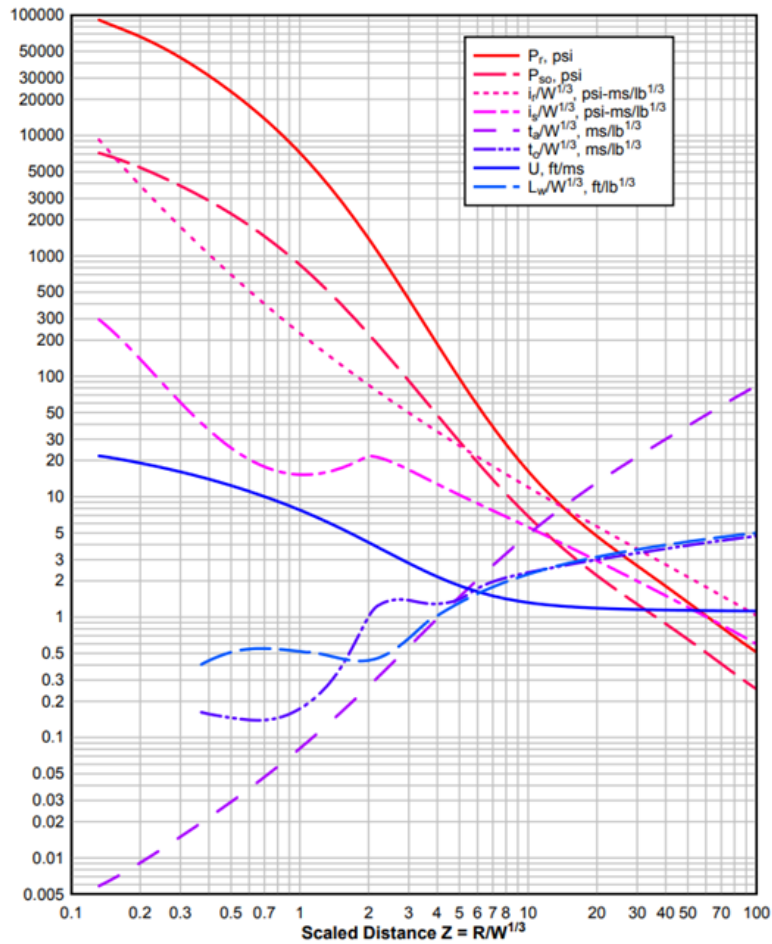


Figure 3: Positive phase shock wave parameters for a spherical TNT explosion in free-air at sea level [2]

1.1.1 Blast Wave Parameters

In addition to the maximum overpressure, impulse and duration, other blast wave parameters that may be involved in determining the blast loads for a structure include [6]:

- Peak reflected pressure, P_r
- Peak dynamic (blast wind) pressure, q_o
- Shock front velocity, U
- Blast wave length, L_w

Typically, these secondary parameters can be computed using the primary blast wave parameters as explained below.

Peak Reflected Pressure, P_r

When a blast wave from an open-air explosion strikes a surface, it reflects. As a result of this reflection, the surface is subjected to a pressure much higher than the incident lateral pressure. The magnitude of the reflected pressure is determined as an amplification of the incident pressure:

$$P_r = C_r P_{so} \tag{3}$$

where C_r : coefficient of reflection. The coefficient of reflection bases on the incidence angle of the wave relative to the reflecting surface, the type of the blast wave and the peak overpressure. The curves in Figure 4 and Figure 5 present the coefficient of reflection (C_r) for peak overpressures up to approximately five times the atmospheric pressure and for shock and pressure waves at incidence angles ranging from 0° to 90° [6].

For maximum overpressure values up to 138 kPa (20 psi), which is the range expected in most air explosions, Newmark indicates a simple formulation for the reflection coefficient of a blast wave at normal 0° incidence :

$$C_r = P_r/P_{so} \approx 2 + 0.05P_{so}(P_{so} : [psi]) \tag{4}$$

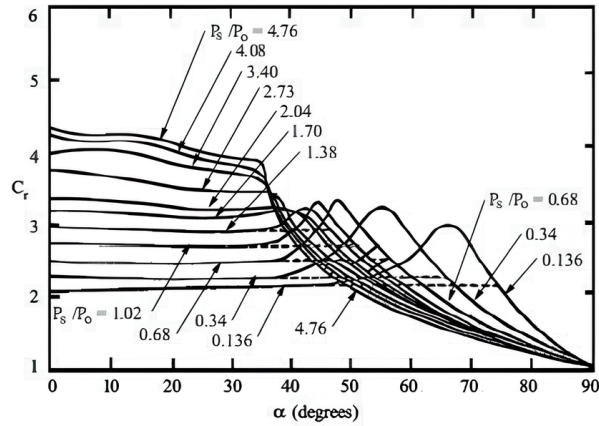


Figure 4: Determination of the reflection coefficient for shock wave [6]

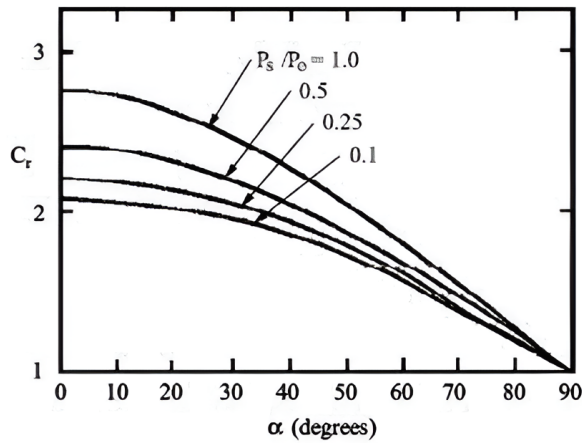


Figure 5: Determination of the reflection coefficient for pressure wave [6]

$$C_r = P_r/P_{so} \approx 2 + 0.0073P_{so}(P_{so} : [kPa]) \tag{5}$$

The dimensions of the reflecting surface can change the duration of the reflected pressure.

Peak Dynamic (Blast Wind) Pressure, q_o .

As the blast wave propagates through the atmosphere, the blast wind pressure, caused by the movement of air due to the blast wave, depends on the velocity of air particles, i.e., the maximum overpressure of the blast wave. To calculate this blast effect, data have been provided by Baker and UFC 3-340-02. Under normal atmospheric conditions, the maximum dynamic pressure can be obtained using Newmark’s empirical formulation [6]:

$$q_o = 2.5P_{so}^2/(7P_o + P_{so}) \approx 0.022P_{so}^2 [psi] \tag{6}$$

$$q_o = 2.5P_{so}^2/(7P_o + P_{so}) \approx 0.0032P_{so}^2 [kPa] \tag{7}$$

where P_o denotes the atmospheric pressure of the environment. The net dynamic pressure on a structure is the product of the dynamic pressure and a drag coefficient, C_d . Depending on the orientation and shape of the obstructing surface, the drag coefficient alters. For a rectangular building, the coefficient of drag can be used as -0.4 for the side and rear walls, as well as roof and $+1.0$ for the front wall [6].

Shock Front Velocity, U

As the blast waves resulting from a free-field explosion propagate through the medium, they travel at or above the speed of sound. For TNT explosives that release high energy, graphs of scaled distance against shock front velocity are provided in UFC 3-340-02 guide. However, similar graphs are not available for the propagation of pressure waves. For design intentions, it may be accepted that a pressure wave moves at the same speed as a shock wave. For standard atmospheric conditions and low-pressure ranges, the pressure / shock front velocities in air can be obtained utilizing the following equations provided by Newmark [6].

$$U \approx 1130(1 + 0.058P_{so})^{0.5} (ft/s) \tag{8}$$

$$U \approx 345(1 + 0.0083P_{so})^{0.5} (m/s) \tag{9}$$

Blast Wavelength, L_w

At any given time, the propagating blast wave extends over a restricted radial distance as the pressure / shock front moves outward. The pressure is greatest at the front and decreases towards the ambient pressure along the length of the blast wave, denoted as L_w . The length of the blast wave in the low-pressure range, can be approximately calculated as follows [6]:

$$L_w \approx Ut_d(m) \tag{10}$$

2 Blast Injury

After discussing the explosion, blast wave, and its characteristics and parameters, this section examines blast injury types and mechanisms, the effects of the blast wave on structures and various parts of the human body, such as the brain, lungs, heart, auditory system, eyes, abdominal region, and musculoskeletal system. Section will end with the injury scaling part.

Typical pressure wave forms for a simple open (free) field explosion and a confined explosion are given in Figure 6. When examining the pressure-time histories, it can be observed that a blast wave in a closed area creates an environment with high pressures for extended periods, allowing more energy transfer to the victim. This increased energy transfer can enhance the lethality of the explosion [7].

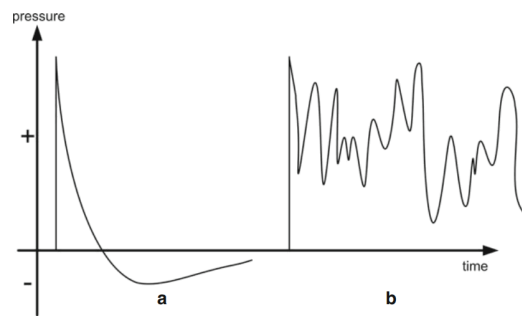


Figure 6: Pressure waveform of a simple open / free field explosion (a) and a closed field explosion (b) [7]

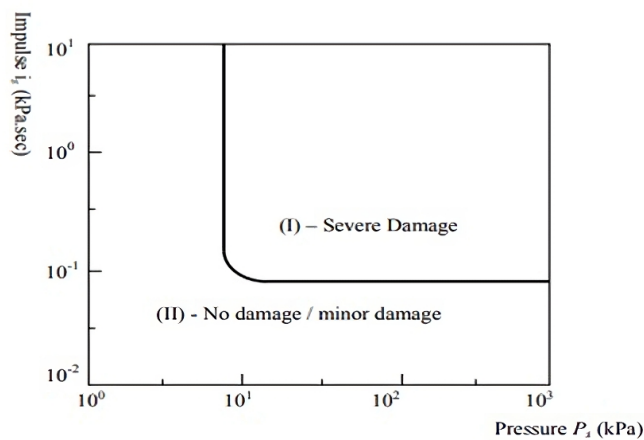


Figure 7: Typical pressure – impulse curve [8]

Also, Figure 7 presents a typical pressure-impulse (P-I) diagram. The pressure-impulse diagram is used to determine specific damage levels by combining the explosion pressures and impulses applied to a specific structural element. As seen in the diagram (Figure 7), Region I indicates severe structural damage, while Region II shows no damage or minor damage [8]. In this context, in recent years, significant efforts have been made to develop blast-resistant reinforced concrete structures for military buildings in regions frequently affected by terrorist attacks and wars [9].

2.1 Blast Injury Types and Mechanisms

Blast injuries alter significantly from other types of injuries in aspects such as injury mechanisms, conditions causing the injury, treatment, and on-site conditions. Therefore, epidemiological features and the injury characteristics of blast injuries are also distinct from those of other injury types.

During a blast injury, both the indirect and direct effects of the blast wave impact the body, making the injured tissues and organs, injury processes and mechanisms quite complex. This complexity is further exacerbated by the varying environment and conditions where the injury occurs. Thus, blast injuries are characterized by features not seen in other types of injuries. Generally, the characteristics of blast injuries can be listed as [3]:

- The dynamic pressure, overpressure and negative pressure of a blast wave can lead to injury either individually or in combination, acting both indirectly and directly. Therefore, complicated injuries are seen in explosions and blast injuries.
- While blast injuries can harm any tissue or part of the body, most blast injuries influence target, specific organs due to the characteristics of the shock wave and the medium of propagation.
- Although minor external injuries may be visible on the human body, serious internal injuries may also occur simultaneously.
- Finally, the rapid worsening of the injury is another characteristic of blast injuries.

Table 1 summarizes common types of blast injuries for different parts of the human body, such as the head, neck-spine, thorax, abdomen, upper extremity, and lower extremity [7].

Table 1: Common types of blast injuries [6]

Parts of the Human body					
Head	Neck - Spine	Thorax	Abdomen	Upper Extremities	Lower Extremities
Fractured skull (brain exposed)	Excessive mobility / fractured spine	Excessive bruising	Penetrating foreign body	Fractured upper / forearm	Fractured Tibia / Fibular / Femur
Fractured maxilla / mandible	Paravertebral haematoma	Penetrating foreign body	Laceration	Disruption at shoulder / elbow / wrist	Foot injury
Disrupted brain tissue	Deep thermal burns	Lacerations	Thermal burns	Hand injury	Disrupted / Fractured Pelvis
Intracranial bleeds	Foreign body-neck	Haemothorax / pneumothorax	Splenic rupture	Penetrating metallic / glass foreign body	Penetrating metallic foreign body
Descalping / Laceration	Laceration	Lung contusions	Renal injury	Traumatic amputation	Traumatic amputation
Tympanic membrane rupture		Fractured / Disrupted ribs		Laceration	Laceration
Deep thermal burns		Deep thermal burns		Degloving	Degloving
Eviscerated eye		Inhalation injury		Deep thermal burns	Deep thermal burns
Orbital injury					
Bruising					

Table 2 shows that blast injuries are classified as primary, secondary, tertiary, quaternary, and quinary, and the types of injuries with high occurrences for these injury mechanisms can be observed [1].

2.2 Review for the Effects of Explosion on the Human Body

Explosions cause damage to numerous components by their nature. Considering the impact load generated during an explosion, the effects of this impulse on structures and the human body are currently being investigated. Different outcomes can occur depending on the explosive types, the presence of shrapnel, the direction of the blast wave, and the effects of quaternary injuries.

Table 3 summarizes the injury criteria recommended by the NATO HFM-148 task group for different body regions, the injury threshold values according to these criteria, and the corresponding anthropomorphic test devices (crash test dummies) [10]. The anthropomorphic test device (ATD), commonly known as a crash test dummy, is a highly precise testing tool utilized to measure human injury potential in vehicle collisions. Crash test dummies simulate human responses to deflections, impacts, forces, accelerations and moments of inertia during a collision. Here, the relevant crash test dummy types are the Hybrid III 50th Male, the ES-2re and MIL-Lx. The Hybrid III male model is the most commonly utilized crash test dummy. The MIL-Lx, lower leg is attached to a standard Hybrid III ATD. Figure 8 shows the corresponding ATDs with example figures [11]. In addition, in spherical air blasts occurring at various distances, the blast wave parameters showing combinations of positive phase durations and peak overpressure are plotted as a series of curves collected according to the respective explosive masses, and are overlapped with estimated primary blast injury (PBI) criteria in Figure 9 [12]. For 100g and 10kg explosives, the curves are plotted with matching stand-off distances to the explosive at specific intervals. When examining the equivalent TNT explosive masses for the actual blast scenarios, the 10kg and 100g explosive masses approximately serve as explosions of improvised explosive devices

Table 2: Blast Injury Mechanisms [1]

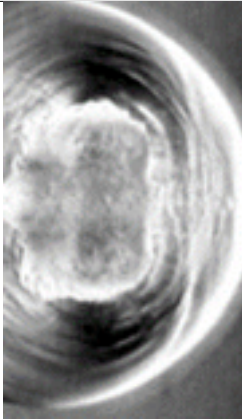



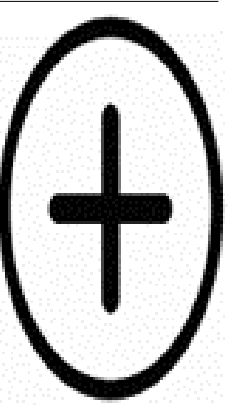
	Primary	Secondary	Tertiary	Quaternary	Quinary
Mechanism					
Definition	High-order explosives : -Impact of over pressurization wave on body surfaces.	High and low order explosives: - Due to flying debris, bomb fragments, other projectiles.	High-order explosions: - Due to individuals being thrown by blast winds or structural collapse	Any explosion-related injury, illness, or disease not due to primary, secondary, or tertiary mechanisms: - Includes exacerbations and complications of pre-existing illnesses.	Hyperinflammatory behavior, unrelated to their injury complex and severity of trauma
High Yield - Injuries	-Blast lung -TM rupture -Globe rupture -Abdominal hemorrhage	-Soft tissue injury -Globe penetration -Wound contamination	"Flying people injury" -Bony fracture -Traumatic amputation -Closed and open brain injuries	-Burns -Crush injury -Inhalation injury	-Prolonged shock and hypotension

Table 3: Injury assessment reference values and associated ATD for evaluating injury risk for different body regions according to NATO [9]

Body Region	Injury Criteria	Metric	Pass / Fail Level	ATD
Head	Head injury criterion	HIC15	250	H3 veya ES-2re + MIL-Lx
Neck	Axial compression force	Fz-	4.0 kN @0 ms / 1.1 kN > 30 ms	ES-2re + MIL-Lx
	Axial tension force	Fz+	3.3 kN @0 ms / 2.8 kN @35 ms / 1.1 kN > 60 ms	ES-2re + MIL-Lx
	Shear force	Fx / Fy	3.1 kN @0 ms / 1.5 kN @25-35 ms / 1.1 kN > 45 ms	ES-2re + MIL-Lx
	Bending moment (flexion)	Mocy+	190 Nm	ES-2re + MIL-Lx
	Bending moment (extension)	Mocy-	96 Nm	ES-2re + MIL-Lx
	Axial tension force	Fz+	1.8 kN	ES-2re + MIL-Lx
Shoulder	Compression force	Fy	1.4 kN	ES-2re + MIL-Lx
Thorax (ribs) (upper/middle/lower)	Rib deflection criterion	RDClateral	28 mm	ES-2re + MIL-Lx
Thorax	Thoracic compression criterion	TCCfrontal	30 mm	H3 + MIL-Lx
Thorax	Viscous criterion	VCfrontal	0.70 m/s	H3 + MIL-Lx
Thorax	Viscous criterion	VClateral	0.58 m/s	ES-2re + MIL-Lx
Abdomen (front/middle/rear)	Abdominal peak force	Ftotal	1.8 kN	ES-2re + MIL-Lx
Spine	Dynamic response index	DRIZ	17.7	H3 veya ES-2re + MIL-Lx
Pelvis	Maximum pubic force	Fy	2.6 kN	ES-2re + MIL-Lx
Upper legs	Axial compression force	Fz-	6.9 kN	H3 veya ES-2re + MIL-Lx
Lower legs	Axial compression force	Fz-	2.6 kN	H3 veya ES-2re + MIL-Lx
Internal organs Lungs	Chest wall velocity predictor	CWVP	3.6 m/s	H3 veya ES-2re + MIL-Lx

and anti-personnel landmines, respectively.

As a result, the following sections will provide information about the responses and injuries of different parts of the human body due to explosions.

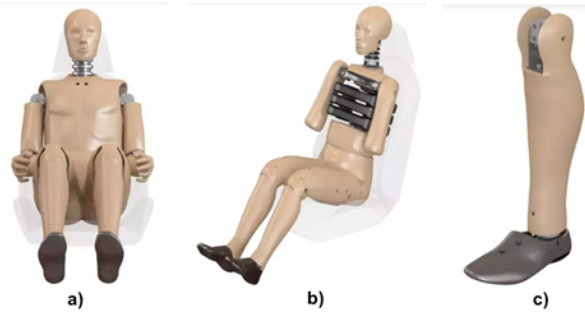


Figure 8: ATD types : a) H3 50th Male, b) ES-2re, c) MIL-Lx legform [11]

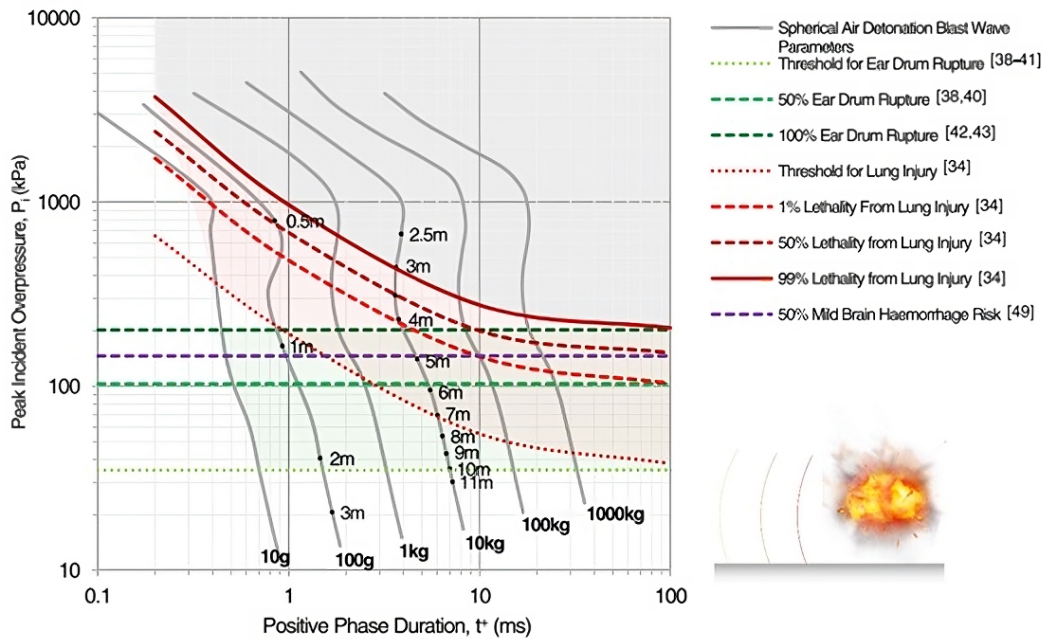


Figure 9: Analysis of PBI criteria based on blast wave parameters resulting from spherical air blasts at different stand-off distances [12]

2.2.1 Head

Traumatic brain injury (TBI) or head trauma is a type of injury resulting from the effect of kinetic energy from the primary blast wave on the brain. Typically, blunt force can complicate the injury in addition to the blast wave. The explosion can further affect the brain through the penetrating effects of secondary injuries or closed head injuries caused by tertiary injuries [13]. Common examples of secondary blast injuries include facial laceration and bodily injuries caused by glass shards. At this point, it is important to note that the properties of the interlayer material in glass significantly affect the structural performance of glass against impact. The full performance of glass is determined by parameters such as the type of glass, its thickness, the type and speed of impact, and boundary conditions [14].

TBIs are generally categorized as primary and secondary injury phases. The primary phase involves direct damage from the transmit of blast load to the intracranial contents while the secondary injury phase involves a series of molecular mechanisms that begin at the moment of impact and continue over hours or days [15]. This phase is multifactorial, involving delayed physiological events in response to the first injury.

The Glasgow Coma Scale (GCS) can be utilized to assess whether a brain injury resulting from a blast is mild, moderate, or severe. Table 4 provides information on the criteria and scoring system of the Glasgow Coma Scale [16]. A score of 13-15 indicates minor brain injury, a score of 9-12 indicates moderate brain injury, and a score of 3-8 indicates severe brain injury. Dizziness, headache, memory loss, seizures, numbness, weakness, and difficulty concentrating are the additional signs and symptoms of TBI [17].

2.2.2 Auditory System

The auditory system is typically influenced by the primary blast wave. The tympanic membrane (TM) can simply stretch due to the differential pressure and can rupture at pressures (<0.5 atm) much lower than those required to harm other organs [18].

Table 4: Glasgow Coma Scale (GCS) criteria and scoring system [14]

GLASGOW COMA SCALE (GCS)		
Response	Scale	Score
Eye Opening Response	Eyes open spontaneously	4 Points
	Eyes open to verbal command, speech, or shout	3 Points
	Eyes open to pain (not applied to face)	2 Points
	No eye opening	1 Point
Verbal Response	Oriented	5 Points
	Confused conversation, but able to answer questions	4 Points
	Inappropriate responses, words discernible	3 Points
	Incomprehensible sounds or speech	2 Points
	No verbal response	1 Point
Motor Response	Obeys commands for movement	6 Points
	Purposeful movement to painful stimulus	5 Points
	Withdraws from pain	4 Points
	Abnormal (spastic) flexion, decorticate posture	3 Points
	Extensor (rigid) response, decerebrate posture	2 Points
	No motor response	1 Point
Minor Brain Injury = 13 -15 points; Moderate Brain Injury = 9-12 points; Severe Brain Injury = 3-8 points		

All patients subjected to an explosion shall be investigated about tinnitus and hearing loss during the initial trauma assessment. To avoid further auditory damage, reducing noise exposure is crucial for long-term recovery.

Most individuals with eardrum injuries who are hemodynamically stable, have no signs on chest radiography, and are followed up by otolaryngology, and who show no findings of blast injury or additional symptoms after a 4-6 hours observation period, recover without intervention. However, about 30% of these individuals progress some degree of permanent loss of hearing [19], [20].

A diagram showing the threshold levels for eardrum rupture and hearing loss due to different blast pressure values is provided in Figure 10 as specified in UFC 3-340-02 (2008) [2]. The graph indicates that 50% of human eardrums exposed to blast pressure rupture at 15 psi, while the threshold pressure for eardrum rupture is 5 psi. It is also observed that temporary hearing loss occurs at lower pressure levels than those causing eardrum rupture [2].

2.2.3 Lung

The lungs can sustain severe damage and potentially fatal outcomes from the primary blast wave due to the significant differences in density throughout the organ. Primary blast lung injury (PBLI) is more likely to happen in closed environments where high-grade explosives are used, which prolongs the duration of the blast wave, or when the victim is close to the blast. The occurrence of PBLI in those who die directly at the blast site may be quite high, ranging from 13% to 47% [21].

Lung injury caused by the primary blast wave contains pulmonary contusions, intrapulmonary hemorrhage, and tearing of the alveolar capillaries. The immediate result of this energy distribution can manifest as respiratory distress, pneumothorax, hypoxia and hemothorax. In addition, there is potential for sudden air embolism from the tearing of alveolar capillaries, which can very quickly result in cardiac arrest or cardiogenic shock. The level of lung damage is related to the degree of absorbed energy from the primary blast wave. Patients can show inadequate oxygenation in the tissues (hypoxia), shortness of breath (dyspnea) and/or increasing cough. Tachycardia (a heart rate over 100 beats per minute), reduced breath sounds and rhonchi may also be present. Also, secondary blast lung damage from debris or flying shrapnel can be more evident during the examination, given the indications of blunt trauma to the thorax or the existence of a penetrating wound.

Depending on available data, survival threshold curves for lung injuries from the response to short-term (3–5 ms) rapidly rising pressures (shock wave) are provided in Figure 11 as specified in UFC 3-340-02 (2008). The graph uses W_h ($1lb = 0.454kg$) to denote human weight. According to the graph, the threshold pressure for lung hemorrhage is 30–40 psi, severe lung hemorrhage is 80 psi and above, and the fatality threshold for lung damage is approximately 100 to 120 psi [2]. The mentioned pressure values are maximum effective pressures, meaning the incident (incoming) pressure should be considered as the largest of the incoming pressure, incoming pressure plus dynamic pressure, or the reflected pressure. Table 5 summarizes the limit pressure values for different types of injuries. Additionally, since survival probability is mass-dependent, the survival probabilities for infants, children, and adults will differ. The recommended weights are 11 lb ($\approx 5kg$) for infants, 55 lb ($\approx 25kg$) for small children, 121 lb ($\approx 55kg$) for adult women, and 154 lb ($\approx 70kg$) for adult men [2].

2.2.4 Eye

The eye, with its heterogeneous density, is remarkably impressionable to trauma. Consequently, the organ is easily affected by damage from both the primary blast wave and secondary blast injury. These injuries are relatively typical in the patient

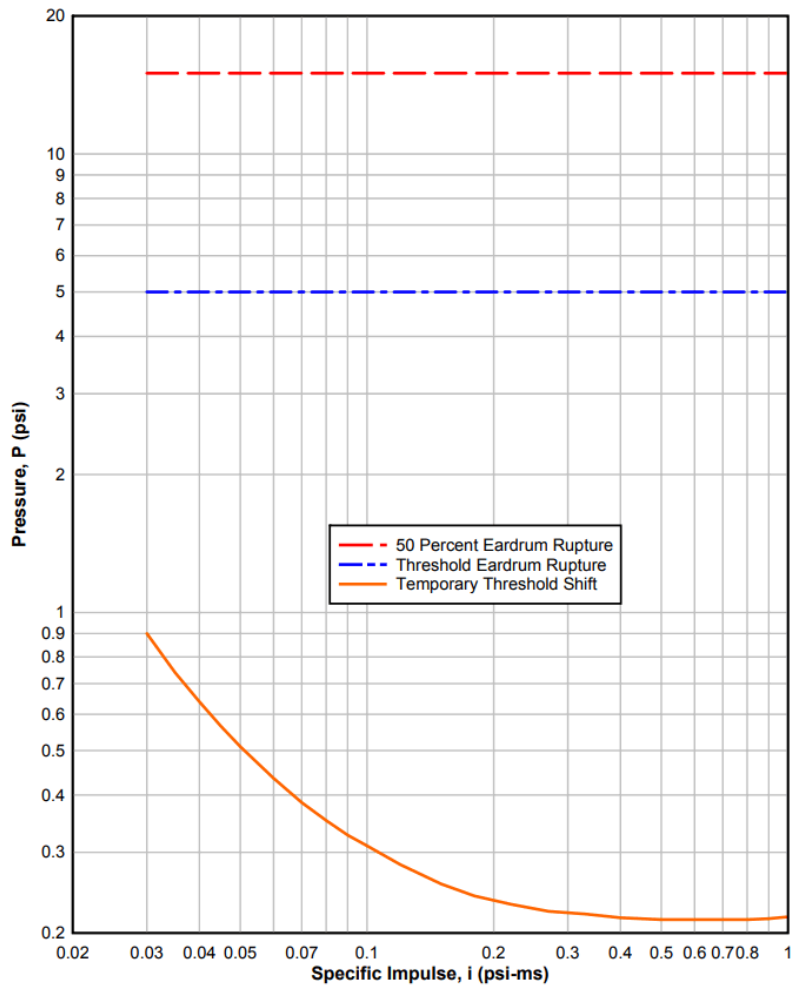


Figure 10: Human ear damage due to blast pressure [2]

Table 5: Effects of short-term (3-5 ms) rapidly rising air blasts on the human body [2]

Critical Organ or Event	Maximum Effective Pressure (psi)
Eardrum Rupture	
Threshold	5
50 percent	15
Lung Damage	
Threshold	30 - 40
50 percent	80 and above
Lethality	
Threshold	100 - 120
50 percent	130 - 180
Near 100 percent	200 - 250

population although they are exceptionally deadly,. The most common blast-related eye injuries contain injuries from both intraocular foreign bodies and superficial, corneal abrasions and eyelid injuries [22]. Secondary blast injuries from flying debris account for the majority of eye injuries in blast patients, including superficial foreign body injuries, conjunctivitis, corneal abrasions and eyelid lacerations. However, the primary blast wave can also cause iris tears, globe rupture, and inflammation-related optic nerve injuries (retrobulbar hematoma) [23].

2.2.5 Cardiac

Although the heart and major blood vessels do not include gas, they can be injured by the kinetic forces and pressure of explosions. Blast-related cardiac injuries present with pathology and content similar to blunt cardiac trauma, containing

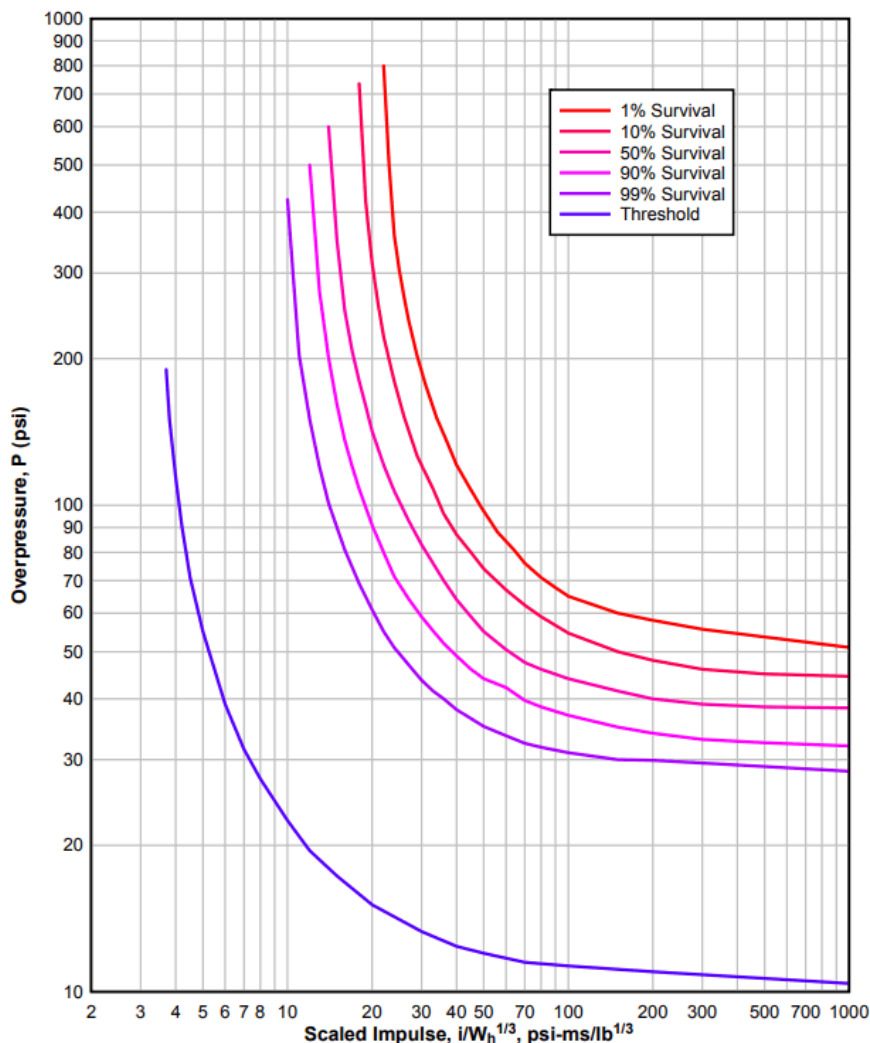


Figure 11: Threshold curves for survival in lung injury, $W_h =$ Weight of human being (lbs) [2]

myocardial contusion, tamponade (fluid accumulation in the pericardial sac), free/septal wall rupture, valve injury, papillary muscle rupture and aortic injuries. When blast-induced cardiac dysfunction is suspected, reducing positive pressure ventilation and providing inotropic support is advised instead of aggressive fluid administration due to the high probability of identical lung injury [24].

2.2.6 Abdomen

The gastrointestinal (GI) system is sensitive to injury from the primary blast wave due to its gas-containing components and heterogeneous density. Although rare among blast survivors, primary blast wave-induced injuries to the intestines can result in perforation, hemorrhage, ischemia and infarction. A huge level of energy transmission from the primary blast wave is needed for these injuries, and they are typically seen in those close to the explosion [24].

Literature indicates that injuries to the GI tract (large intestine, small intestine, stomach) account for 48% of abdominal injuries in blast victims [25]. The gas including sections of the GI tract are the most defenseless to the primary blast effect, but solid organs can also be damaged. GI injury is also more common in underwater explosions due to the medium's capability to transmit pressure and apply higher forces. Damages to solid organs such as the spleen, kidneys and liver are mainly linked with the patient's proximity to the source of the primary blast wave and high-grade primary blast waves [25].

Abdominal symptoms can be developed by patients up to 14 days after exposure to a blast [26]. Therefore, monitoring of symptoms and repeated evaluation are crucial for diagnosing gastrointestinal damage [13].

2.2.7 Musculoskeletal System

Blast injuries usually affect the musculoskeletal system. In a group of 101 blast victims, 57% had extremity injuries. Among these, 75.2% had at least one fracture, and over 90% had open fractures [27]. The closer the blast victim is to the epicenter of the explosion, the more likely they are to have multiple fractures, and more serious open fractures are affiliated with higher mortality [27]. For patients with serious extremity hemorrhage, tourniquet application is essential. For individuals with indication of traumatic injury, plain radiographs of the effected region shall be acquired after initial stabilization. Other injuries of extremity can be splinted after initial stabilization.

2.3 Injury Scaling

An injury scale is a method used to assign severity score or a numerical assessment to traumatic injuries. The most commonly utilized injury scale is the Abbreviated Injury Scale (AIS), developed by the American Association for Automotive Medicine (AAAM) and it first published in 1971.

2.3.1 Abbreviated Injury Score (AIS)

The Abbreviated Injury Scale (AIS) is a method of injury scaling that assigns a severity rating from 1 to 6 to distinct anatomical injuries. Table 6 supplies the AIS definitions and examples for spine and head injuries. An essential restriction of the AIS is that it does not represent the potential outcome for the entire individual and examines each injury in isolation [28].

Table 6: Abbreviated Injury Scale (AIS) scores and example injury types for two body parts [10]

AIS	Severity	Head	Spine
0	None	—	—
1	Minor	Headache or dizziness	Acute strain (No fracture or dislocation)
2	Moderate	Unconsciousness less than 1 hour ; Linear fracture	Minor fracture without any cord involvement
3	Serious	Unconscious 1 to 6 hours ; Depressed fracture	Ruptured disc with nerve root damage
4	Severe	Unconscious 6 to 24 hours ; Open fracture	Incomplete cervical cord syndrome
5	Critical	Unconscious more than 24 hours ; Large hematoma	C4 or below cervical complete cord syndrome
6	Maximum Injury (virtually nonsurvivable)	Crush of skull	C3 or above cervical complete cord syndrome

2.3.2 Injury Severity Score (ISS)

The Injury Severity Score (ISS) that was developed in 1974 is a technique used to characterize trauma patients with multiple injuries and is commonly used in trauma literature due to its connection with the AIS. The ISS depend on the AIS, which explains the severity of injuries in distinct body parts [29].

$$ISS = (A)^2 + (B)^2 + (C)^2 \tag{11}$$

Values A, B, and C in Equation 11 represent the scores of the three most severely injured body parts according to the Abbreviated Injury Scale. A represents the face, neck and head; B represents abdomen and the thorax; and C represents the extremities. Considering that the maximum AIS score for each region is 5, the ISS ranges from 0 to 75. However, if any of the three values is 6, the ISS is automatically set to 75 because an AIS score of 6 represents an injury that is not survivable. Table 7 describes the injury severity levels, definitions, and examples of possible injuries for different value ranges of the Injury Severity Score [30].

2.3.3 Dynamic Response Index (DRI)

The Dynamic Response Index (DRI) indicates the peak dynamic pressure of the spinal column and is computed by modeling the human body as an analog, lumped mass-parametric mechanical system consisting of a mass, damper and spring. The DRI model evaluates the human body response to temporary acceleration-time profiles. Potential spinal injuries for positive z-acceleration environments in ejection seats could be predicted effectively by using the DRI. The threshold acceleration values for DRI are provided in Table 8 [28].

Table 7: Injury based damage level definitions (ISS) [12]

ISS Range	Proposed Hazard Level	Injury Description	Example of Injuries
$ISS \geq 25$	High Injury	Fatal / Severe Injury	Multiple very serious injuries Primarily fatalities
$10 < ISS < 25$	Medium Injury	Serious Life Threatening Injury	Very severe lacerations with significant blood loss Severe open bone fractures Crush injuries Skull fractures Bone fractures
$5 < ISS \leq 10$	Low Injury	Hospitalization Required, Not Immediately Life Threatening	Large numbers of lacerations Artery or tendon lacerations Concussions
$1 < ISS \leq 5$	Very Low Injury	Medical Aid Necessary, But No Hospitalization Required	Lacerations to face and body from glass fragments Cuts or abrasions to eye Contusions and abrasions
$0 \leq ISS \leq 1$	Minimal Injury	No Medical Aid Required	No injury Minor bruises and cuts Small foreign object in eyes Hearing loss

Table 8: Dynamic Response (DR) limits [10]

DR Level	Acceleration Direction (occupant's inertial response)					
	x		y		z	
	DRx < 0	DRx > 0	DRy < 0	DRy > 0	DRz < 0	DRz > 0
Low	-28	35	-14	14	-13.4	15.2
Moderate	-35	40	-17	17	-16.5	18
High risk	-46	46	-22	22	-20.4	22.4

2.3.4 Head Injury Criterion (HIC)

The Head Injury Criterion (HIC) is an evaluation of the possibility of head injury resulting from an impact. This variable is normally obtained from the acceleration-time history at the center of gravity of a dummy's head when exposed to impact forces.

$$HIC = \max \left[(t_2 - t_1) \left(\frac{1}{(t_2 - t_1)} \left[\int_{t_1}^{t_2} a(\tau) d\tau \right] \right)^{2.5} \right] \tag{12}$$

The acceleration-time history, $a(t)$, calculated at the center of mass of the dummy's head, is used analytically to compute the HIC as the square root of the sum of the squares of the acceleration-time histories in the x, y, and z directions over a 15 ms time interval, as given in Equation 13 [31]:

$$a(t) = \sqrt{(a_x^2(t)) + (a_y^2(t)) + (a_z^2(t))} \tag{13}$$

In the HIC formulation, t_1 represents the starting time, and $\Delta t = t_2 - t_1$ represents the maximum time interval over which the acceleration is calculated. With the condition $0 \leq t_1 \leq t_2 \leq T$, it is indicated that t_1 and the maximum time interval, Δt can initially be selected arbitrarily. Additionally, some simplified model assumptions are explained as follows [31]:

- The time interval $t_2 - t_1$ should be $\leq 36ms$. According to experience, larger deceleration times do not boost the risk of injury.
- The highest acceleration values should last 3 ms. This requirement arises from measurement method reasons and is sustained by the acceptance that shorter decelerations don't have any impact on the brain.

The head injury criterion consist of four distinct injury criteria [31]:

- Head Injury Criterion [HIC] : Skull fracture from blunt object impacts and brain injury.
- Blunt Object Skull Fracture Injury Criterion [kN] : Skull fracture resulting from blunt object impacts.
- Facial Injury Criterion [kN/mm] : Injury resulting from blunt object impacts and facial fracture.
- Facial Laceration Criterion : Facial laceration.

The levels related to the head injury criterion, the corresponding Abbreviated Injury Scale (AIS) values, and the associated descriptions of head injury or consciousness level are provided in Table 9 [31].

Table 9: Consciousness levels associated with Head Injury Criteria [31]

Head Injury Criteria	AIS Code	Level of Brain Concussion and Head Injury
135 - 519	1	Headache or dizziness
520 - 899	2	Unconscious less than 1 hour - Linear fracture
900 - 1254	3	Unconscious 1 - 6 hours - Depressed fracture
1255 - 1574	4	Unconscious 6 - 24 hours - Open fracture
1575 - 1859	5	Unconscious greater than 24 hours - Large hematoma
> 1860	6	Non-survivable

Table 10: Head Injury Criterion (HIC) tolerance levels [31]

Injury Criteria		Tolerance Levels				
Criterion	Units	Level 0 No Injury Egress	Level 1 Minor Injury Egress	Level 2 Major Injury Egress Assisted	Level 3 Severe Injury Medical Assistance	Level 4 Potentially Non-survivable
HIC - Brain injury (in all head impacts)	HIC (15 ms)	<150 (No concussion)	<150 (No concussion)	150 - 500 (Mild concussion)	500 - 1800 (Severe concussion)	>1800 (Life threatening coma)
HIC - Skull fracture (flat impacts)	HIC (15 ms)	<500 (No fracture)	<500 (No fracture)	500 - 900 (Minor fracture)	900 - 1800 (Major fracture)	>1800 (Life threatening coma)
Blunt object skull fracture	kN	<0.02 (No fracture)	<2.2 (No fracture)	2.2 - 5.5 (Minor depressed fracture)	>5.5 (Major depressed fracture)	>5.5 (Life threatening)
Facial injury	kN/mm	<0.02 (Very minor injury)	0.02 - 0.045 (Minor facial injury)	0.045 - 0.0825 (Major facial injury)	>0.0825 (Severe facial injury)	>0.0825 (Life threatening)
Facial laceration	Cuts to chamois leather thin layer	0	0	Moderate	Major	N/A

Also, Table 10 provides the tolerance levels and associated descriptions for different types of head injury criteria [31]. Tables 9 and 10 are used to evaluate the injuries sustained by the dummy in numerical analyses.

The probabilities of different severity levels of head injury for a given head injury criterion score are shown in Figure 12. The graph indicates that a HIC score of around 2500 corresponds to a 85% fatality rate and a 95% likelihood of critical head injury [31].

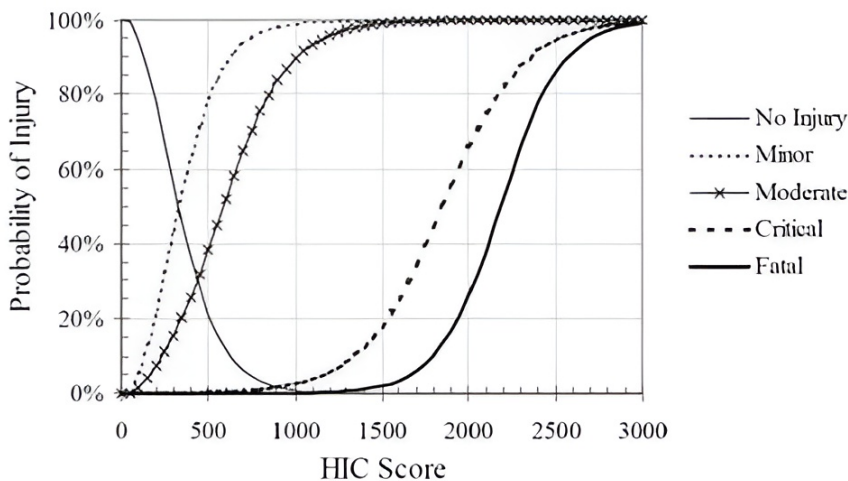


Figure 12: Probabilities of different severity levels of head injury for HIC scores [31]

2.3.5 Neck Injury Criterion

The Neck Injury Criterion (NIC), introduced by the National Highway Traffic Safety Administration (NHTSA), integrates the impacts of moments and forces calculated at the occipital condyle and is an excellent estimator of cranio-cervical injuries. The NIC considers N_{TF} (tension-flexion), N_{TE} (tension-extension), N_{CF} (compression-flexion) and N_{CE} (compression-extension). Federal Motor Vehicle Safety Standard (FMVSS) 208 needs that none of the four N_{ij} values surpass 1.4 at any point. The generalized N_{ij} is given by the following equation [28]:

$$N_{ij} = \frac{F_z}{F_{zc}} + \frac{M_y}{M_{yc}} \tag{14}$$

where F_z is the axial force for the upper neck (N), F_{zc} is the critical axial force (N), M_y is the moment around the occipital condyle (Nm), M_{yc} is the critical moment around the occipital condyle (Nm).

2.3.6 Lumbar Load Criterion

The lumbar load criterion specifies that the highest compressive force calculated between the lumbar spine and pelvis of a test dummy during a crash impact, where the vertical axis of the spine is parallel to the predominant impact vector, should not exceed 6672 N [28]. Additionally, the compressive force should not surpass 3800 N over a 30 ms time interval [28]. This is one of the most commonly utilized criteria in crash tests and vertical impact. Lastly, severe compression or severance of the spinal cord can result in death or paralysis.

2.3.7 Chest Criteria

The Chest Injury Criterion specifies that the maximum resultant acceleration measured by a triaxial accelerometer in the upper thorax should not exceed 60g for more than 3 ms [28]. In addition, chest deflection determined by a chest potentiometer behind the sternum should be less than 7.62 cm for the Hybrid III dummy [28].

2.3.8 Femur Force Criterion

The Femur Force Criterion indicates that the axial compressive force carried along each upper leg shall not be bigger than a certain value. Impulse loads that are larger than this limit may result in the total fracture of the femur bone and cause the severance of main arteries, leading to excessive bleeding. Different studies specify distinct values for the permissible highest axial compressive force. It is indicated by the Wayne State University that the permissible maximum value is 10,000 N [28]. The U.S. Department of the Army declares that the axial compressive force should not exceed 7562 N over a 10 ms time interval and should not exceed 9074 N at any moment [28].

In real dummies, load cells are put in the dummy's leg and are calibrated to measure the compressive force in the femur.

2.4 Proposed Injury Criteria

Based on numerous studies in the existing literature, when threshold values related to blast pressure for human injuries in spherical air blasts are reviewed and compiled [2], [3], [7], [12], [28], [31], the limit blast pressure values for different parts of the human body for various positive phase duration ranges are proposed as shown in Table 11.

Table 11: Limit blast pressure values for different parts of the human body and corresponding blast positive phase duration ranges

Positive Phase Duration td (ms)	Criteria	Lung	Ear	Head-Brain
$td \leq 10$	Peak Pressure (kPa)	55 : Threshold 150 : 1% Lethality 200 : 50% Lethality 300 : 99% Lethality	35 : Threshold 100 : 50% Ear Drum Rupture 200 : 100% Ear Drum Rupture	150 : 50% Mild Brain Hemorrhage Risk 270 : 50% Moderate Brain Hemorrhage Apnea Risk 400 : 50% Primary Blast Brain Fatality
$10 < td \leq 50$	Peak Pressure (kPa)	42 : Threshold 110 : 1% Lethality 160 : 50% Lethality 220 : 99% Lethality	35 : Threshold 100 : 50% Ear Drum Rupture 200 : 100% Ear Drum Rupture	150 : 50% Mild Brain Hemorrhage Risk
$50 < td < 200$	Peak Pressure (kPa)	28 : Threshold 90 : 1% Lethality 125 : 50% Lethality 185 : 99% Lethality	35 : Threshold 100 : 50% Ear Drum Rupture 200 : 100% Ear Drum Rupture	150 : 50% Mild Brain Hemorrhage Risk

3 Conclusion

In this paper, the focus is on the blast wave, blast wave parameters, blast injuries, types and mechanisms of blast injuries, the effects of explosions on the human body, and injury scaling and criteria. It is observed that for a blast with a positive phase duration up to 10 ms, the threshold blast pressure for lung injury is 55 kPa, whereas for the ear it is 35 kPa. At a blast pressure of 150 kPa, the probability of death due to lung injury is 1%, while there is a 50% risk of experiencing a mild brain hemorrhage. At 200 kPa, the probability of death due to lung injury is 50%, and there is a 100% likelihood of eardrum rupture. At a threshold of 300 kPa, there is a 99% likelihood of death due to lung injury. Additionally, the threshold for a 50% chance of moderate brain hemorrhage is 270 kPa, whereas at a threshold of 400 kPa, primary blast-induced brain fatalities are expected. Finally, a blast

pressure range of 690-825 kPa is considered the threshold range for blast-induced death, with values between 895-1240 kPa indicating a 50% chance of death, and values in the 1380-1725 kPa range indicating an almost 100% likelihood of blast-induced death [2].

Acknowledgments

The authors greatly thank Scientific and Technical Research Council of Turkey (TUBITAK) for scholarship.

Authors' Contributions

In this study, authors contributed equally to the study.

Competing Interests

The authors declare that they have no conflict of interest.

References

- [1] J. Bukowski, C. D. Nowadly, S. G. Schauer, A. Koyfman, and B. Long, "High risk and low prevalence diseases: Blast injuries," *The American Journal of Emergency Medicine*, vol. 70, pp. 46–56, 2023.
- [2] U. DoD, "Unified facilities criteria (ufc) structures to resist the effects of accidental," 2008.
- [3] Z. Wang and J. Jiang, *Explosive Blast Injuries: Principles and Practices*. Springer Nature, 2023.
- [4] S. Nadyrov, "Pencere camının ve çerçeve sistemlerinin patlamaya karşı davranışı," Master's thesis, Fen Bilimleri Enstitüsü.
- [5] M. Chiranjeevi and J. Simon, "Analysis of reinforced concrete 3d frame under blast loading and check for progressive collapse," *Indian Journal of Science and Technology*, vol. 9, no. 30, pp. 1–6, 2016.
- [6] T. C. on Blast-Resistant Design of the Petrochemical Committee of the Energy Division of ASCE, "Design of blast-resistant buildings in petrochemical facilities." American Society of Civil Engineers, 2010.
- [7] A. M. Bull, J. Clasper, and P. F. Mahoney, "Blast injury science and engineering," *Switzerland: Springer*, 2016.
- [8] T. Ngo, P. Mendis, A. Gupta, and J. Ramsay, "Blast loading and blast effects on structures—an overview," *Electronic journal of structural engineering*, no. 1, pp. 76–91, 2007.
- [9] M. Şahin, İ. Karagöz, M. Öksüz, and S. Yazıcıoğlu, "Properties of concrete reinforced with m12 monofilament type polypropylene fiber," *El-Cezeri*, vol. 8, no. 1, pp. 481–494, 2021.
- [10] F. J. Gallun, A. C. Diedesch, L. R. Kubli, T. C. Walden, R. L. Folmer, M. S. Lewis, D. J. McDermott, S. A. Fausti, and M. R. Leek, "Performance on tests of central auditory processing by individuals exposed to high-intensity blasts," *J Rehabil Res Dev*, vol. 49, no. 7, pp. 1005–25, 2012.
- [11] (Accessed 07.01.2024). [Online]. Available: <https://www.humaneticsgroup.com/>
- [12] J. Denny, A. Dickinson, and G. S. Langdon, "Defining blast loading 'zones of relevance' for primary blast injury research: A consensus of injury criteria for idealised explosive scenarios," *Medical Engineering & Physics*, vol. 93, pp. 83–92, 2021.
- [13] J. E. Smith and J. Garner, "Pathophysiology of primary blast injury," *BMJ Military Health*, vol. 165, no. 1, pp. 57–62, 2019.
- [14] M. Karadağ, U. C. Vural, and B. Karasu, "Otomotiv sektöründe cam," *El-Cezeri*, vol. 6, no. 2, pp. 299–322, 2019.
- [15] S. Yamamoto, D. S. DeWitt, and D. S. Prough, "Impact & blast traumatic brain injury: implications for therapy," *Molecules*, vol. 23, no. 2, p. 245, 2018.
- [16] B. Jennett, "Development of glasgow coma and outcome scales," *Nepal journal of neuroscience*, vol. 2, no. 1, pp. 24–28, 2005.
- [17] M. W. Greve and B. J. Zink, "Pathophysiology of traumatic brain injury," *Mount Sinai Journal of Medicine: A Journal of Translational and Personalized Medicine*, vol. 76, no. 2, pp. 97–104, 2009.
- [18] R. G. DePalma, D. G. Burris, H. R. Champion, and M. J. Hodgson, "Blast injuries," *New England Journal of Medicine*, vol. 352, no. 13, pp. 1335–1342, 2005.
- [19] S. Goh, "Bomb blast mass casualty incidents: initial triage and management of injuries," *Singapore Med J*, vol. 50, no. 1, pp. 101–106, 2009.
- [20] D. D. Yeh and W. P. Schecter, "Primary blast injuries—an updated concise review," *World journal of surgery*, vol. 36, pp. 966–972, 2012.
- [21] T. E. Scott, A. M. Johnston, D. D. Keene, M. Rana, and P. F. Mahoney, "Primary blast lung injury: the uk military experience," *Military medicine*, vol. 185, no. 5-6, pp. e568–e572, 2020.
- [22] M. G. Morley, J. K. Nguyen, J. S. Heier, B. J. Shingleton, J. F. Pasternak, and K. S. Bower, "Blast eye injuries: a review for first responders," *Disaster medicine and public health preparedness*, vol. 4, no. 2, pp. 154–160, 2010.
- [23] Y. Liu, K. Feng, H. Jiang, F. Hu, J. Gao, W. Zhang, W. Zhang, B. Huang, R. Brant, C. Zhang *et al.*, "Characteristics and treatments of ocular blast injury in tianjin explosion in china," *BMC ophthalmology*, vol. 20, pp. 1–8, 2020.
- [24] Z. R. Mathews and A. Koyfman, "Blast injuries," *The Journal of emergency medicine*, vol. 49, no. 4, pp. 573–587, 2015.
- [25] I. Wani, F. Q. Parray, T. Sheikh, R. A. Wani, A. Amin, I. Gul, and M. Nazir, "Spectrum of abdominal organ injury in a primary blast type," *World journal of emergency surgery*, vol. 4, pp. 1–5, 2009.
- [26] C. Owers, J. Morgan, and J. Garner, "Abdominal trauma in primary blast injury," *Journal of British Surgery*, vol. 98, no. 2, pp. 168–179, 2011.
- [27] M. Tahtabasi, S. Er, R. Karasu, and E. R. Ucaroglu, "Bomb blast: imaging findings, treatment and clinical course of extremity traumas," *BMC emergency medicine*, vol. 21, pp. 1–10, 2021.
- [28] A. Tabiei, C. Lawrence, and E. L. Fasanella, "Validation of finite element crash test dummy models for predicting orion crew member injuries during a simulated vehicle landing," in *10th International LS-DYNA Users Conference*, no. E-16677, 2009.
- [29] S. P. Baker, B. o'Neill, W. Haddon Jr, and W. B. Long, "The injury severity score: a method for describing patients with multiple injuries and evaluating emergency care," *Journal of Trauma and Acute Care Surgery*, vol. 14, no. 3, pp. 187–196, 1974.
- [30] S. Meyer, L. Little, and E. Conrath, "Injury based glass hazard assessment," *DTIC Document*, 2004.
- [31] R. Panowicz, K. Sybilski, and D. Kołodziejczyk, "Numerical analysis of effects of ied side explosion on crew of lightarmoured wheeled vehicle," *Journal of KONES*, vol. 18, pp. 331–339, 2011.



Research Article

Mango Leaf Disease Detection Using Deep Feature Extraction and Machine Learning Methods: A Comparative Survey

Yavuz Ünal^{1a}, Muammer Türkoğlu^{2b}

¹Computer Engineering Department, Amasya University, Amasya, Türkiye

²Software Engineering Department, Faculty of Engineering and Natural Science, Samsun University, Samsun, Türkiye

yavuz.unal@amasya.edu.tr

DOI : 10.31202/ecjse.1420624

Received: 16.01.2024 Accepted: 27.09.2024

How to cite this article:

Bilal Balun, Omer Faruk Nemetlu, Ali Sari, Ahmet Benli, " Statistical Analysis of Wind Characteristic and Wind Energy Potential Based on Weibull Distribution in Bingol Province, Turkey ", El-Cezeri Journal of Science and Engineering, Vol: 12, Iss: 1, (2025), pp.(35-43).

ORCID: ^a0000-0002-3007-679X; ^b 0000-0002-2377-4979.

Abstract : Plant diseases pose a significant threat to the quality and quantity of agricultural production, with leaf diseases being particularly detrimental to plant growth and yield. In the near future, ensuring access to affordable and safe food will become one of the most pressing global challenges. As a result, the early detection of plant diseases is crucial for both economic stability and food security. Detecting and monitoring diseases in mango leaves, however, is a complex task when relying solely on visual inspection. This study seeks to address this challenge by utilizing image processing and deep learning techniques to detect mango leaf diseases. We extracted deep features from mango leaf images using several prominent architectures, including Darknet19, Xception, SqueezeNet, MobileNetv2, DenseNet201, GoogLeNet, ResNet18, VGG16, and AlexNet. These features were then classified using machine learning algorithms such as decision tree, linear discriminant analysis, naive Bayes, support vector machine, k-nearest neighbors, and ensemble classifiers. Our findings demonstrate an improvement over existing results in the literature, with detailed experimental results presented within the article.

Keywords : Deep Feature Extraction, Mango Leaf Disease, Transfer Learning, Deep Learning.

1 Introduction

Agricultural products are one of the most effective ways of feeding the world's growing population. Protecting plants from disease and detecting disease at an early stage are key to producing high-quality agricultural food. Many factors, such as climate change, are increasing the incidence of plant diseases. Each year, around 40% of the world's food crops are destroyed by pests and diseases. Minimising plant diseases is also important to ensure global food security [1]. Plant diseases, weeds and pests are responsible for low crop yields. Known as the "king of fruits", the mango is one of the most important fruit crops grown in various countries around the world. The mango plant is one of the leading agricultural products and plays an important role in the economies of some Asian countries. Millions of people depend on mango cultivation for their livelihoods [2]. Plant diseases are one of the major constraints to the growth of mango plants. The major diseases are anthracnose, bacterial blossom blight, golmachi, moricha disease, shuttling, bacterial black spot, apical bud necrosis, red rust, lichen, powdery mildew, root rot, dumping off and ganoderma root rot. Powdery mildew and anthracnose are the two diseases that cause the most damage to mango trees [3].

In recent years, with the rapid development of deep learning technologies, people have begun to experiment with various artificial intelligence (AI) methods for plant disease detection. Traditional machine vision algorithms need to consider the task and prior knowledge when selecting the right features. These features often include the colour, shape and texture of the image. The manual design is the basis of the feature extractors. This process is tedious and challenging. In addition, the feature extractors are not able to generalise. On the other hand, deep learning techniques can modify the weight parameters and create a suitable feature extractor. The process is quite convenient and effective. In addition, feature extractors have greater generalisation capabilities and can successfully overcome the drawbacks of traditional image processing techniques [4]. As technological methods such as machine learning, deep learning, and image processing are applied in the field of agriculture, yield loss will decrease and production will increase [5]. In this study, features were extracted from mango leaves using deep feature extraction and disease classification was performed on mango leaves using different machine learning algorithms.

In this paper, deep feature extraction and various machine learning algorithms were used to detect mango leaf diseases. Previous studies have demonstrated the effectiveness of deep learning and image processing techniques in the field of disease

detection. Among these studies, Manoharan et al. [6] divided mango leaf images, consisting of a total of 440 images, into two classes, sick and healthy, and classified them with AlexNet, VGG16, and the method they suggested. They achieved a classification accuracy of 61% with AlexNet, 62% with VGG16, and 98% with the model they suggested. In their study, Mia et al. [3] classified the features extracted from mango leaf images using neural networks and support vector machines (SVMs). They classified 4 diseased mango leaf varieties and 1 healthy mango leaf variety with 80% accuracy. Saleem et al. [7] proposed a new segmentation approach to segment diseased parts by considering vein patterns in mango leaves. For this purpose, they performed canonical correlation analysis (CCA)-based feature extraction. These authors classified these features with cubic SVM and obtained a classification accuracy of 95.5%. Rao et al. [1] classified grape leaves and mango leaves in the PlantVillage dataset with AlexNet, the pre-trained CNN model. These models achieved classification accuracies of 99% and 89%, respectively. By using Faster R-CNN, Merchant et al. [8] detected the stems and leaves of mango plants with 74% accuracy. A mobile application has been developed for this purpose. Venkatesh et al. [9] developed a network named V2IncepNet based on the VGGNet model to detect anthracnose disease on mango leaf images, and they achieved 92% classification accuracy with this network. Kumar et al. [10] classified anthracnose disease in mango leaves by deep learning. They proposed a new CNN architecture and achieved 96.16% classification accuracy with this proposed network. Singh et al. [11] classified a dataset consisting of 1070 mango leaf images with a multilayer convolution neural network (MCNN) and compared them with PSO, SVM, and RBFNN, which they used as other classifiers. These authors achieved 97% accuracy with MCNN and obtained better results than the others. Arya et al. [12] applied CNN and AlexNet to mango and potato leaf images consisting of 4004 images. They obtained a classification accuracy of 90.85% with the CNN and 98.33% with the AlexNet. Pham et al. [13] studied a dataset consisting of 450 mango leaf images. This dataset included anthracnose, Gall Midge, powdery mildew, and healthy classes. They classified the leaf images by feature selection with AlexNet, VGG16 ResNet50, and ANN. The best result was obtained from the ANN (89.41%). Trang et al. [14] studied a dataset consisting of 394 mango leaf images and anthracnose, gall midge, powdery mildew, and healthy classes. They classified this dataset with InceptionV3, AlexNet, MobilnetV2, and their proposed residual network. They obtained the most successful classification with their own proposed residual network. With this model, they achieved 88.46% classification accuracy. Mohona et al. [15] analyzed a dataset consisting of corn, grape, mango, and pepper plant leaves with VGG16, VGG19, GoogLeNet, and the network model they proposed. They achieved the most successful results with their proposed network model. Tumang et al. [16] first performed contrast enhancement, to determine pests and diseases on mango leaves and subsequently performed image segmentation via K-means. The authors extracted gray level and GLCM features and classified them with Multi SVM. They achieved 85% classification accuracy. Rajbongshi et al. [17] used a dataset of 1500 mango leaf images in their study. This dataset included anthracnose, gall machi, healthy leaf, powdery mildew, and red rust classes. DenseNet201, InceptionResNetV2, InceptionV3, ResNet50, ResNet152V2, and Xception transfer learning techniques from pre-trained networks were applied to this dataset. They achieved 98% classification accuracy with DensNet201. Gulavnai and Patil (2019) applied the transfer learning models ResNet18, ResNet34, and ResNet50 to a dataset consisting of mango leaf images in their study. These leaf images contained the following diseases: powdery mildew, anthracnose, red rust, and Golich. With this dataset consisting of a total of 8853 images, the best classification accuracy was obtained with ResNet50 (91.50%). Ahmed et al. [18] created a dataset of 4000 mango leaf images. This dataset contains 1800 manually captured images and 2200 augmented images in the following classes: bacterial canker, cutting weevil, dieback, gall midge, powdery mildew, sooty mold, and healthy. The authors achieved 87% precision in their classification with CNN, 79% precision with ResNet50, and 91% precision with CNN-SVM.

In this study, deep learning and machine learning techniques were used for early detection of mango leaf diseases. Deep features were extracted from mango leaf images using various deep learning models (Darknet19, Xception, SqueezeNet, MobileNetv2, DenseNet201, GoogLeNet, ResNet18, VGG16 and AlexNet) and these features were classified using decision tree, linear discriminant analysis, naive bayes, support vector machines, k-nearest neighbour and ensemble classifiers. As a result of the experimental studies, the existing results in the literature have been improved and detailed results are presented in this paper.

2 Materials and Method

2.1 Dataset

The mangoleafbd dataset was used in this study [19]. There are 4000 images of mango leaves in this dataset. A total of 1800 plants were obtained by photographing different leaves. The remaining 2200 images were prepared by zooming and rotating where necessary. There are seven disease classes of mango leaves and one healthy leaf class in this dataset. These diseases include anthracnose, bacterial canker, cutting weevil, dieback, gall midge, powdery mildew and sooty mould. The images have a size of 240x320 pixels and are three-channel (RGB) coloured in JPG format. There are 500 images in each category. The photos were taken with a mobile phone camera. Details of the dataset are given in Table 1.

The dataset includes 500 images for each of the mango leaf disease classes, with conditions such as anthracnose, bacterial canker, cutting weevil damage, die-back, powdery mildew, and sooty mold. Anthracnose, caused by *Colletotrichum gloeosporioides*, manifests as black spots on leaves, affecting young branches and reducing fruit production. Bacterial canker,

Table 1: Classes in the mangoleafdb dataset.

Label	Class	Number of Images
1	Anthracnose	500
2	Bacterial Canker	500
3	Cutting Weevil	500
4	Die Back	500
5	Gall Midge	500
6	Powdery Mildew	500
7	Sooty Mould	500
8	Healty	500

from *Xanthomonas axonopodis*, appears as yellow to brown spots with a white halo. Cutting weevil damage is represented by insect-eaten leaves. Die-back, due to *Liaiodiplodia theobromae*, impacts leaves, flowers, and fruits. Powdery mildew, caused by *Oidium mangiferae*, produces a white fungus layer, leading to leaf yellowing and death in severe cases. Sooty mold, associated with insect feeding, blocks sunlight and hinders photosynthesis [18], [20]. Sample images in the data set used in the study are given in Figure 1.

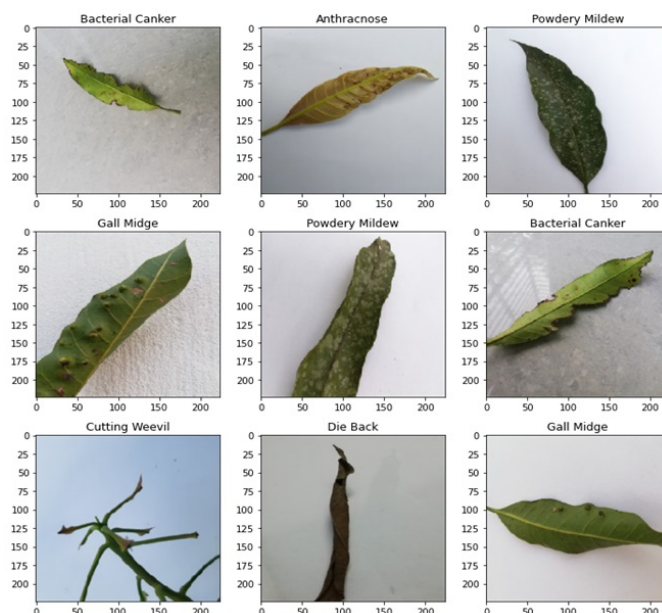


Figure 1: Data samples from the dataset used in this study

2.2 Proposed Method

In this paper, we present deep convolutional neural networks (CNNs) and machine learning classifiers for mango leaf disease detection. In this method, 9 powerful pre-trained deep architectures based on a transfer learning approach such as DenseNet201, AlexNet, VGG16 and ResNet18 are used. These architectures are used to extract deep features from mango leaf images. These deep features are then fed into six machine learning classifier methods, such as decision tree, SVM and KNN, and the training process is carried out. A general representation of the developed system is shown in Figure 2.

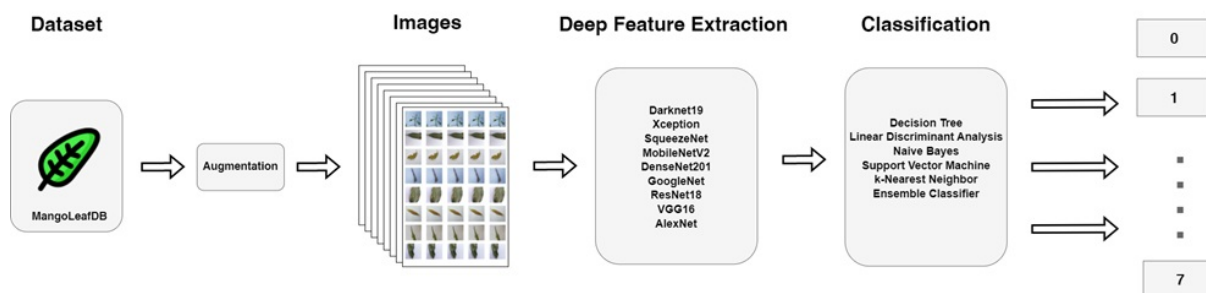


Figure 2: Summary of proposed methods in this study

As shown in Figure 2, extensive experimental studies based on pre-trained deep models and classifiers have been carried out for mango leaf disease detection. The theoretical background of these algorithms is given in the subheadings below.

2.3 Deep Learning and Pretrained CNN Models

Hinton proposed a new approach to artificial neural networks in the article he published with his studies. This approach is called the deep convolution neural network. Convolutional neural networks are known as multilayer neural networks. Important studies have been carried out with these neural network systems, and high-performance results have been obtained. Deep convolutional neural networks have achieved important success by increasing these achievements to higher levels [21]. With the training of deep learning models, especially convolutional networks, on large datasets such as ImageNet, very successful models have been developed. Training such models on relatively small datasets quickly causes the model to diverge or overfit. Therefore, the use of such models with pre-trained weight parameters on big data can produce successful test results on data of similar content and small size. Pretrained models with fine-tuning are frequently used for solving image processing problems [22], [23]. In this study, the pre-trained models Darknet19, Xception, SqueezeNet, MobileNetV2, DenseNet201, GoogLeNet, ResNet18, VGG16, and AlexNet were used. Features are extracted by using the weight parameters of these pre-trained models, and then classification is performed with various methods consisting of comprehensive classification methods. The feature extractor layers and feature sizes of the deep learning models used in the current study are given in Table 2.

Table 2: Feature extractor layers of the pre-trained CNN models used in this study

Pretrained Deep Models	Feature Extractor Layer	Feature Count	Image Size
DarkNet19	avg1	1000	256x256
AlexNet	fc6	4096	227x227
Xception	predictions	1000	299x299
SqueezeNet	pool10	1000	227x227
MobileNetv2	Logits	1000	224x224
DenseNet201	fc1000	1000	224x224
GoogLeNet	loss3-classifier	1000	224x224
ResNet18	fc1000	100	224x224
VGG16	fc6	4096	224x224

The deep learning architectures listed in Table 2 are known for their high performance in object classification. Among them, MobileNetV1 [24]. is a model developed by Google in 2017 for mobile devices with low computational power, which significantly reduces network complexity and model size by using deeply separable convolutions. MobileNetV2 improves on this structure and provides more efficient performance. Another model, the Xception network [25], is based on InceptionV3 and performs more efficient operations on multidimensional data by treating the convolutional layers as separate operations. ResNet [26] overcomes the 'vanishing gradient' problem by adding residual blocks and provides better learning by preventing information loss in the deeper layers of the network. DenseNet [27] is a model that facilitates network training by connecting each layer to all subsequent layers and optimises loss of function in multi-layer networks. VGG16 [28] is a model developed by Simonyan and Zisserman in 2014 that includes 5 block convolutional layers of 3x3 size and was successful in the ImageNet Visual Recognition Competition. SqueezeNet [29] is an architecture developed in 2016 with the aim of achieving AlexNet-level accuracy with fewer parameters, reducing the computational load of the network by using efficient layers and enabling it to work fast. Finally, AlexNet [21] is a model developed by Krizhevsky, Sutskever and Hinton in 2012, which won the ImageNet competition and gained worldwide recognition for deep learning. AlexNet is considered one of the models that started the deep learning revolution with its sequential convolution and fusion layers.

2.4 Classifiers

In this study, various machine learning classifiers, including decision trees, linear discriminant analysis (LDA), naive Bayes, support vector machines (SVM), k-nearest neighbors (KNN), and ensemble methods, are employed to classify the deep features extracted from specific layers of pre-trained deep learning models. These classification techniques can be summarized as follows:

- *Decision Tree*: Decision trees are structured similarly to real trees, consisting of roots, branches and leaves. The process begins at the root node, where the data set is progressively divided into smaller subsets based on specific feature values, creating branches. Each internal node represents a decision or condition, while the final nodes, known as leaves, represent the class labels or results. The classification process involves two main stages: the training (learning) phase and the testing phase. During the training phase, the model is built by examining the training data and generating classification rules based on patterns in the data. These rules are used to build the decision tree. In the classification phase, test data is applied to the model to verify its accuracy in predicting the correct classes by following the decision paths established in the learning phase [30].
- *Linear Discriminant Analysis (LDA)*: Dimensionality reduction is one of the most widely used techniques in machine learning applications and its main purpose is to reduce the dimensionality of the feature space by removing redundant features. LDA, one of the most commonly used methods in this process, optimises class separation by maximising the ratio of between-class variance to within-class variance. By transforming the data into a lower dimensional space, this technique performs the projection of features in a way that provides the highest separation between classes [31].

Table 3: Parameters of the classifiers used in this study

Decision Tree				
Preset	Max. number of splits	Split	Criterion	
Fine Tree	100		Gini's diversity index	
Medium Tree	20		Gini's diversity index	
Coarse Tree	4		Gini's diversity index	
SVM				
Kernel Function	Kernel Scale	Box constraint level	Multiclass method	
Linear	Automatic	1	One-vs-One	
Quadratic	Automatic	1	One-vs-One	
Cubic	Automatic	1	One-vs-One	
Gaussian	32	1	One-vs-One	
Gaussian	100	1	One-vs-One	
KNN				
Preset	Number of neighbors	Distance metric	Distance weight	
Fine	1	Euclidean	Equal	
Medium	10	Euclidean	Equal	
Coarse	10	Euclidean	Equal	
Cosine	10	Cosine	Equal	
Cubic	10	Minkowski	Equal	
Weighted	10	Euclidean	Squared Inverse	
Ensemble				
Preset	Ensemble method	Learner Type	Max. number of splits	Subspace dimensions
Boosted Trees	AdaBoost	Decision tree	20	-
Bagged Trees	Bag	Decision tree	3199	-
Subspace Disc.	Subspace	Discriminant	-	500
Subspace KNN	Subspace	Nearest neigh.	-	500

- *Naive Bayes*: The Naive Bayes classifier is an algorithm commonly used in supervised learning and is widely used in areas such as data mining, machine learning and sentiment analysis. It uses Bayes' theorem to estimate the probability that a feature belongs to a particular class. Naive Bayes assumes that the features in the classification are independent of each other and performs class prediction by calculating the probability of each feature independently of the others. Simple probability calculations are used to estimate the probability of events occurring [32].
- *Support Vector Machine (SVM)*: Support Vector Machines are a powerful classification method that works by creating an n-dimensional hyperplane that optimally separates the data into two classes. SVMs use a sigmoid kernel function and a two-layer feed-forward neural network, and are closely related to artificial neural networks. The interesting aspect of SVMs is that they use structural risk minimisation rather than the traditional empirical risk minimisation based on minimising the mean of the error squares. SVMs can be used in regression and classification tasks and have the ability to solve non-linear cases with kernel functions [33].
- *K-Nearest Neighbours (KNN)*: KNN is a simple and adaptive multi-class classifier based on neighbourhood. The parameter 'k' indicates how many nearest neighbours should be considered when determining the class of a new sample. Small values of k can make the classification more sensitive to noise, while large values of k become computationally expensive. When k=1, a new sample is classified by nearest neighbour. When k>1, the classification can be influenced by more than one neighbor [34].
- *Ensemble Classifier*: Ensemble learning techniques, which combine the results of several algorithms, outperform individual algorithms. By combining the votes of different classifiers, it makes more accurate predictions based on features derived from different data projections. The first examples of ensemble learning date back to the early part of the last century, and this method often produces stronger results by combining weak classifiers [35].
The hyperparameters for the classifier algorithms used in the present study are given in Table 3.

2.5 Performance Metrics

In this study, accuracy, derived from the confusion matrix, is used as the primary metric to evaluate performance. The confusion matrix is a widely used tool in classification tasks and consists of a table with rows and columns representing the predicted and actual classes. Each cell in the matrix contains values corresponding to the number of correctly or incorrectly classified instances. Additional performance metrics such as accuracy, precision, recall and F1 score can also be calculated from the confusion matrix.

The confusion matrix contains four essential parameters: true positives (TP), true negatives (TN), false positives (FP) and false negatives (FN). True positives (TP) are the number of correctly predicted positive cases, while true negatives (TN) are the number of correctly predicted negative cases. False positives (FP) are the number of negative cases incorrectly predicted as

positive, and false negatives (FN) are the number of positive cases incorrectly predicted as negative. The accuracy formula is given below.

$$\text{Accuracy} = \frac{TP + TN}{TP + TN + FN + FP} \tag{1}$$

3 Results and Discussion

The experiments were performed using a computer with an Intel Core i7-10875H-2.30 GHz CPU, 32 GB of RAM, and an NVIDIA GeForce RTX 2080 super. In addition, we used 10-fold cross-validation to calculate the performance of the proposed model in all the experimental studies.

In the experimental phase, the first step was to evaluate the performance of different pre-trained deep learning models using a transfer learning approach. The results of these evaluations are shown in Figure 4. The transfer learning method used in this study involved modifying the original deep learning architectures by replacing the last three layers with four newly designed layers: fully connected, softmax and classification layers. This adjustment allowed the models to better adapt to the specific dataset used for mango leaf disease detection. The experimental setup included key deep learning hyperparameters, with each model trained for 50 epochs, a batch size of 8, and using the Adam optimizer. The choice of Adam was driven by its ability to adjust learning rates for different parameters, ensuring faster convergence and improved performance. This configuration was designed to optimize the balance between computational efficiency and model accuracy, allowing effective fine-tuning of the pre-trained models on the new dataset.

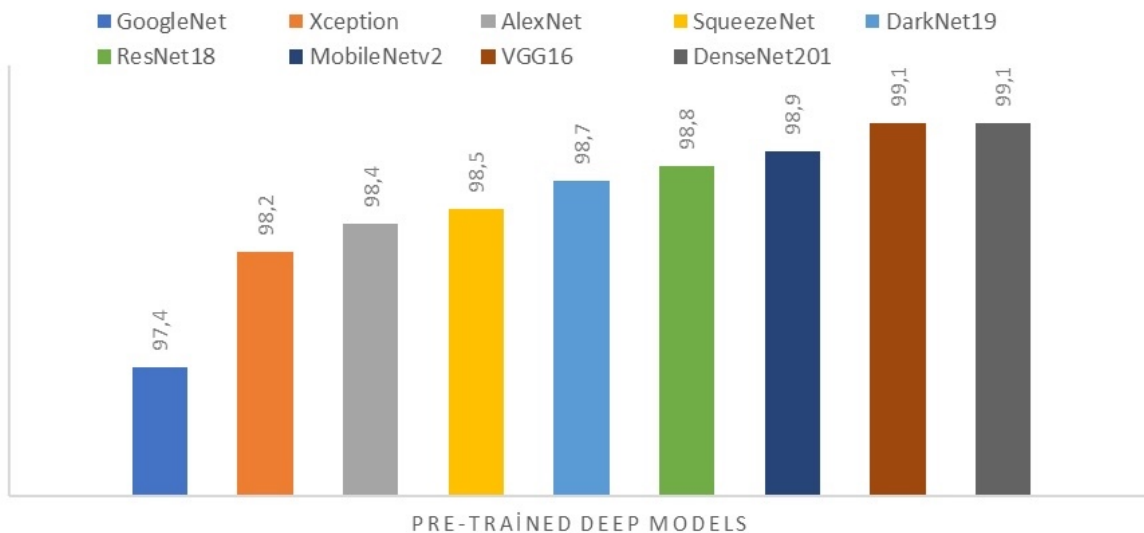


Figure 3: Accuracy scores of pre-trained deep models based on transfer learning approach

As shown in Figure 3, the highest accuracy was achieved with the DenseNet201 and VGG16 architectures, both reaching an impressive 99.1%. In contrast, the GoogLeNet architecture produced the lowest accuracy of the models evaluated. However, the remaining deep learning models showed strong performance, with accuracy scores ranging from around 98% to 99%, highlighting their overall effectiveness in the classification task.

In the second phase of the experimental study, pre-trained deep learning models were used as feature extractors. The deep features from the mango leaf images were extracted using each of the pre-trained architectures. These extracted features were then used to train different machine learning classifier algorithms. First, the performance of the decision tree classifier was evaluated using the parameters outlined in Table 3, and the corresponding results are presented in Table 4.

As shown in Table 4, the highest accuracy of 87.9% was achieved by combining the fine kernel-based decision tree with the Darknet19 model. In addition, the medium tree classifier gave the best performance when combined with the ResNet18 model. In contrast, the coarse tree classifier showed significantly lower accuracy compared to the other approaches, indicating relatively poor performance.

The performance results were then calculated using the parameters given in Table 3 based on the SVM classifier and are shown in Table 5.

As shown in Table 5, the highest accuracy achieved was 99.8%, resulting from several combinations of deep learning models, including Quadratic SVM-DenseNet201, Quadratic SVM-ResNet18, Quadratic SVM-VGG16, Cubic SVM-DenseNet201 and Cubic SVM-VGG16. In addition, five different kernel-based SVM classifiers consistently produced an average accuracy of 99% or higher.

Table 4: The accuracy scores % based on the combination of a deep feature extractor and a decision tree classifier

	Tree		
	Fine	Medium	Coarse
DarkNet19	87.9	81.5	48.4
Xception	86.5	72.4	45.2
Squeezenet	86.1	73.2	46.7
Mobilenetv2	76.9	73.2	42
Densenet201	87.8	79.9	47.9
GoogleNet	82.1	71.9	45.3
Resnet18	87.5	82.4	46.7
Vgg16	86	76.3	45.1
AlexNet	81.7	75.8	45.6

Table 5: The accuracy scores % based on the combination of the deep feature extractor and SVM classifier

	SVM					
	Linear	Quadratic	Cubic	Medium Gaussian	Coarse Gaussian	
DarkNet19	99.3	99.7	99.6	99.5		98.6
Xception	98.7	99.4	99.3	98.9		97.7
Squeezenet	99.2	99.4	99.5	98.8		98
Mobilenetv2	99.5	99.7	99.7	99.4		98.9
Densenet201	99.6	99.8	99.8	99.5		98.9
GoogleNet	98.2	98.7	98.9	98.2		96.7
Resnet18	99.6	99.8	99.7	99.4		98.9
Vgg16	99.7	99.8	99.8	99.5		98.9
AlexNet	99	99.4	99.4	99		97.7

The performance results using the k-nearest neighbours (KNN) classifier were then evaluated using the parameters given in Table 3, with the results summarised in Table 6.

As shown in Table 5, the highest accuracy achieved was 99.8%, resulting from several combinations of deep learning models, including Quadratic SVM-DenseNet201, Quadratic SVM-ResNet18, Quadratic SVM-VGG16, Cubic SVM-DenseNet201 and Cubic SVM-VGG16. In addition, five different kernel-based SVM classifiers consistently produced an average accuracy of 99% or higher.

The performance results using the k-nearest neighbours (KNN) classifier were then evaluated using the parameters given in Table 3, with the results summarised in Table 6.

As shown in Table 7, the highest accuracy, 100%, was achieved by combining the ensemble subspace discriminant classifier with the DenseNet201 model. In addition, all other pre-trained deep models also showed strong performance when using the ensemble subspace discriminant classifier, achieving accuracies of 99%. Furthermore, the ensemble subspace KNN classifier outperformed both the boosted trees and bagged trees methods.

Table 6: The accuracy scores % based on the combination of the deep feature extractor and KNN classifier

	KNN					
	Fine	Medium	Coarse	Cosine	Cubic	Weighted
DarkNet19	99	97.3	91.5	97.5	97.3	97.7
Xception	98.7	97.1	91.9	98	97.3	97.7
Squeezenet	98.2	97.1	90.3	95.9	97	97.4
Mobilenetv2	99.1	98.3	94.2	98.4	98.3	98.6
Densenet201	99.2	98.4	92.2	98.5	98.2	98.7
GoogleNet	96.9	95.3	89.5	95.5	95.4	96
Resnet18	99.1	98	94.8	98.3	98.1	98.3
Vgg16	98.9	96.6	88.1	97.7	96.5	97.2
AlexNet	96.9	93.8	84.8	94.9	93.8	95

Table 7: The accuracy scores % based on the combination of a deep feature extractor and an ensemble classifier

	Ensemble			
	Boosted Trees	Bagged Trees	Subspace Discriminant	Subspace KNN
DarkNet19	88.4	95.9	99.8	99
Xception	91.6	94.8	99.2	98.9
Squeezenet	89.7	94.9	99.6	98.2
Mobilenetv2	89.1	95	99.6	98.2
Densenet201	91.6	96.5	100	99.2
GoogleNet	83.9	93.7	99	96.7
Resnet18	92.1	95.9	99.9	99
Vgg16	92.8	96.2	99.7	99
AlexNet	90.4	93.2	99.2	96.8

Table 8: The accuracy scores % based on the combination of a deep feature extractor and machine learning classifiers

MODELS	Ensemble Classifier Models Accuracy Comparison					
	Transfer Learning Approach	Linear Discriminant	KNN (Fine)	Decision Tree (Fine)	SVM (Quadratic)	Ensemble Subspace Discriminant
DarkNet19	98.7	99.8	99	87.9	99.7	99.8
Xception	98.2	99.4	98.7	86.5	99.4	99.8
Squeezenet	98.5	99.7	98.2	86.1	99.4	99.6
Mobilenetv2	98.9	99.7	99.1	76.9	99.7	99.6
Densenet201	99.1	100	99.2	87.8	99.8	100
GoogLeNet	97.4	99.1	96.9	82.1	98.7	99
Resnet18	98.8	99.8	99.1	87.5	99.8	99.7
Vgg16	99.1	99.8	98.9	86	99.8	99.7
AlexNet	98.4	99.2	96.9	81.7	99.4	99.2

Finally, Table 8 provides a comprehensive comparison of the results of the deep learning models using the transfer learning approach and the deep feature extraction approach combined with different machine learning classifiers.

As shown in Table 8, the best performing classifiers on average were the Linear Discriminant Analysis (LDA) and the Ensemble Subspace Discriminant methods. When combined with the DenseNet201 model, these classifiers achieved perfect accuracy of 100%. In addition, DenseNet201 proved to be the best deep feature extractor overall. In comparison, the other deep learning models using the transfer learning approach delivered lower performance than the models where deep feature extraction was paired with machine learning classifiers.

4 Conclusion

In this paper, the features extracted by deep feature extraction from the data of seven diseased plants and one healthy class of mango plant leaves were classified by different machine learning algorithms and the results were compared. In this study, both features were extracted by deep learning and these extracted features were classified by seven different classifiers. We extracted deep features from the fully connected layers of these deep models (DarkNet19, Xception, SqueezeNet, MobenetV2, DenseNet201, GoogLeNet and ResNet18). The features obtained were classified by decision tree, linear discriminant, naive Bayes, support vector machine, k-nearest neighbour, ensemble and MLP methods. Several of the classifiers were tested with different kernels. Fine, medium and coarse kernels are used for the decision tree, and linear, quadratic, cubic, fine Gaussian, medium Gaussian and coarse Gaussian kernels are used for the SVMs. Fine, medium, coarse, cosine, cubic and weighted kernels were used for k-nearest neighbours. For ensembles, boosted trees, bagged trees, subspace discriminants, subspace KNNs and rusboosted tree kernels were used. In future studies, different approaches and analyses can be applied to this dataset. This study provides insight into the evaluation of architectures run on this particular dataset, the possibility of automatic diagnosis of mango leaf diseases, and performance parameters. This study has made a unique contribution to the literature by applying the proposed methodology to a mango leaf image dataset. The methodology fulfilled the task of automatically diagnosing mango leaf diseases with an accuracy rate of more than 99%.

Authors' Contributions

Methodology, Y.U.; software, M.T.; validation, M.T.; formal analysis, M.T.; investigation, Y.U.; resources, Y.U.; data curation, M.T.; writing-original draft preparation, Y.U.; writing-review and editing, M.T.

Competing Interests

The authors declare that they have no conflict of interest.

References

- [1] V. S. L. A. K. C. P. K. N. U Sanath Rao, R Swathi, "Deep learning precision farming: Grapes and mango leaf disease detection by transfer learning," *Global Transitions Proceedings*, vol. 2, no. 2, pp. 535–544, 2021, international Conference on Computing System and its Applications (ICCSA- 2021).
- [2] R. P. Sampada Gulavnai, "Deep learning for image based mango leaf disease detection," *International Journal of Recent Technology and Engineering (IJRTE)*, vol. 8, no. 3S3, pp. 54–56, 2019. [Online]. Available: <https://www.ijrte.org/wp-content/uploads/papers/v8i3s3/C10301183S319.pdf>
- [3] S. R. Md. Rassel Mia and M. A. Rahman, "Mango leaf disease recognition using neural network and support vector machine," *Iran Journal of Computer Science*, vol. 3, pp. 185–193, 2020.
- [4] L. Xu, B. Cao, F. Zhao, S. Ning, P. Xu, W. Zhang, and X. Hou, "Wheat leaf disease identification based on deep learning algorithms," *Physiological and Molecular Plant Pathology*, vol. 123, p. 101940, 2023. [Online]. Available: <https://www.sciencedirect.com/science/article/pii/S0885576522001552>
- [5] K. G. Liakos, P. Busato, D. Moshou, S. Pearson, and D. Bochtis, "Machine learning in agriculture: A review," *Sensors*, vol. 18, no. 8, 2018. [Online]. Available: <https://www.mdpi.com/1424-8220/18/8/2674>
- [6] N. Manoharan, V. J. Thomas, and D. Anto Sahaya Dhas, "Identification of mango leaf disease using deep learning," in *2021 Asian Conference on Innovation in Technology (ASIANTCON)*, 2021, pp. 1–8.
- [7] R. Saleem, J. H. Shah, M. Sharif, M. Yasmin, H.-S. Yong, and J. Cha, "Mango leaf disease recognition and classification using novel segmentation and vein pattern technique," *Applied Sciences*, vol. 11, no. 24, 2021. [Online]. Available: <https://www.mdpi.com/2076-3417/11/24/11901>
- [8] M. Merchant, V. Paradkar, M. Khanna, and S. Gokhale, "Mango leaf deficiency detection using digital image processing and machine learning," in *2018 3rd International Conference for Convergence in Technology (I2CT)*, 2018, pp. 1–3.

- [9] Venkatesh, N. Y. S. T. S., S. S., and S. U. Hegde, "Transfer learning based convolutional neural network model for classification of mango leaves infected by anthracnose," in *2020 IEEE International Conference for Innovation in Technology (INOCON)*, 2020, pp. 1–7.
- [10] P. Kumar, S. Ashtekar, S. S. Jayakrishna, K. P. Bharath, P. T. Vanathi, and M. Rajesh Kumar, "Classification of mango leaves infected by fungal disease anthracnose using deep learning," in *2021 5th International Conference on Computing Methodologies and Communication (ICCMC)*, 2021, pp. 1723–1729.
- [11] U. P. Singh, S. S. Chouhan, S. Jain, and S. Jain, "Multilayer convolution neural network for the classification of mango leaves infected by anthracnose disease," *IEEE Access*, vol. 7, pp. 43 721–43 729, 2019.
- [12] S. Arya and R. Singh, "A comparative study of cnn and alexnet for detection of disease in potato and mango leaf," in *2019 International Conference on Issues and Challenges in Intelligent Computing Techniques (ICICT)*, vol. 1, 2019, pp. 1–6.
- [13] T. N. Pham, L. V. Tran, and S. V. T. Dao, "Early disease classification of mango leaves using feed-forward neural network and hybrid metaheuristic feature selection," *IEEE Access*, vol. 8, pp. 189 960–189 973, 2020.
- [14] W. Tang, Q. Yang, K. Xiong, and W. Yan, "Deep learning based automatic defect identification of photovoltaic module using electroluminescence images," *Solar Energy*, vol. 201, pp. 453–460, 2020. [Online]. Available: <https://www.sciencedirect.com/science/article/pii/S0038092X20302875>
- [15] S. A. Mohona, S. Aktar, and M. M. Ahamad, "Efficient computation of leaf disease classification techniques using deep learning," in *2021 3rd International Conference on Electrical Electronic Engineering (ICEEE)*. IEEE, 2021, pp. 149–152.
- [16] G. S. Tumang, "Pests and diseases identification in mango using matlab," in *2019 5th International Conference on Engineering, Applied Sciences and Technology (ICEAST)*, 2019, pp. 1–4.
- [17] M. M. R. A. P. S. M. T. S. N. R. C. Aditya Rajbongshi, Thaharim Khan, "Recognition of mango leaf disease using convolutional neural network models: a transfer learning approach," *Indonesian Journal of Electrical Engineering and Computer Science*, vol. 23, no. 3, pp. 1681–1688, 2021.
- [18] S. I. Ahmed, M. Ibrahim, M. Nadim, M. M. Rahman, M. M. Shejunti, T. Jabid, and M. S. Ali, "Mangoleafbd: A comprehensive image dataset to classify diseased and healthy mango leaves," 2022. [Online]. Available: <https://arxiv.org/abs/2209.02377>
- [19] S. I. A. M. N. M. R. M. M. S. T. J. Sawkat Ali, Muhammad Ibrahim, "Mangoleafbd dataset," Online, 2022, 20.10.2024. [Online]. Available: <https://data.mendeley.com/datasets/hxsnvwt3r/1>
- [20] L. F. Arauz, "Mango anthracnose: economic impact and current options for integrated management," *Plant Disease*, vol. 84, pp. 600–611, 2007.
- [21] A. Krizhevsky, I. Sutskever, and G. E. Hinton, "Imagenet classification with deep convolutional neural networks," *Commun. ACM*, vol. 60, no. 6, p. 84–90, May 2017. [Online]. Available: <https://doi.org/10.1145/3065386>
- [22] U. R. Nadeem Akhtar, "Interpretation of intelligence in cnn-pooling processes: a methodological survey," *Neural Computing and Applications*, vol. 32, no. 3, pp. 879–898, 2020.
- [23] M. M.-S. J. M.-B. A. S. L. E. E. S. Olivias, J.D.M. Guerrero, "Transfer learning," in *Handbook of Research on Machine Learning Applications and Trends: Algorithms, Methods, and Techniques*, baskı sayısı (opsiyonel) ed., ser. Seri Adı (Opsiyonel), J. S. Lisa Torrey, Ed. Yayıncı Şehri: IGI Global, 2010, vol. Cilt Numarası (Opsiyonel), ch. Bölüm Numarası, pp. 242 – 264.
- [24] A. G. Howard, M. Zhu, B. Chen, D. Kalenichenko, W. Wang, T. Weyand, M. Andreetto, and H. Adam, "Mobilenets: Efficient convolutional neural networks for mobile vision applications," 2017. [Online]. Available: <https://arxiv.org/abs/1704.04861>
- [25] F. Chollet, "Xception: Deep learning with depthwise separable convolutions," 2017. [Online]. Available: <https://arxiv.org/abs/1610.02357>
- [26] Y. Tai, J. Yang, and X. Liu, "Image super-resolution via deep recursive residual network," in *2017 IEEE Conference on Computer Vision and Pattern Recognition (CVPR)*, 2017, pp. 2790–2798.
- [27] G. Huang, Z. Liu, and K. Q. Weinberger, "Densely connected convolutional networks," *CoRR*, vol. abs/1608.06993, 2016. [Online]. Available: <http://arxiv.org/abs/1608.06993>
- [28] A. Z. Karen Simonyan, "Very deep convolutional networks for large-scale image recognition," *Computer Vision and Pattern Recognition*, vol. abs/1608.06993, 2014. [Online]. Available: <https://arxiv.org/abs/1409.1556>
- [29] F. N. Iandola, M. W. Moskewicz, K. Ashraf, S. Han, W. J. Dally, and K. Keutzer, "Squeezenet: Alexnet-level accuracy with 50x fewer parameters and <1mb model size," *CoRR*, vol. abs/1602.07360, 2016. [Online]. Available: <http://arxiv.org/abs/1602.07360>
- [30] O. M. Lior Rokach, "Data mining with decision trees," in *Series in Machine Perception and Artificial Intelligence*, P. C.-L. Liu, Ed. World Scientific, 2007, pp. 71–86.
- [31] A. I.-A. E. H. Alaa Tharwat, Tarek Gaber, "Linear discriminant analysis: : A detailed tutorial," *AI Communications*, vol. 30, no. 2, pp. 169–190, 2017.
- [32] C. C. Aggarwal, *Data Classification*, 1st ed. Chapman and Hall/CRC, 2014.
- [33] V. V. Corinna Cortes, "Support-vector networks," *Machine Learning*, vol. 20, pp. 273–297, 1995.
- [34] M. N. A. H. Sha'abani, N. Fuad, N. Jamal, and M. F. Ismail.
- [35] W. C.-Y. S. Xibin Dong, Zhiwen Yu and Q. Ma, "A survey on ensemble learning," *Frontiers of Computer Science*, vol. 14, pp. 241–258, 2020.

Research Article

Classification of Cell Line Halm Machine Data in Solar Energy Panel Production Factories Using Artificial Intelligence Models

Murat Simsek^{1a}, Ozel Sebetci^{2b}, Irfan Yilmaz^{3c}

¹Artificial Intelligence Engineering Department, Ostim Technical University, Ankara, Türkiye

²Department of Computer Technologies, Aydın Adnan Menderes University, Aydın, Türkiye

³Software Engineering Department, Ostim Technical University, Ankara, Türkiye

osebetci@adu.edu.tr

DOI : 10.31202/ecjse.1580430

Received: 06.11.2024 Accepted: 09.01.2025

How to cite this article:

Murat Simsek, Ozel Sebetci, Irfan Yilmaz, "Classification of Cell Line Halm Machine Data in Solar Energy Panel Production Factories Using Artificial Intelligence Models", El-Cezeri Journal of Science and Engineering, Vol: 12, Iss: 1, (2025), pp.(44-53).

ORCID: "0000-0002-8648-3693; ^b0000-0002-2996-0270, ^c0009-0007-6168-4580.

Abstract : This study presents a quality estimation method for photovoltaic cells in solar panels using advanced machine learning techniques, including traditional methods and convolutional neural networks (CNNs). Photovoltaic cells, which are primarily composed of crystalline silicon, are of critical importance for the conversion of sunlight into electrical energy. The efficiency of these cells directly affects the performance and lifespan of solar panels. The study's objective is to assess the electroluminescence values of cells using the HALM device, which is capable of measuring the key parameters that determine cell quality. To enhance the performance of the CNN model, hyperparameter tuning and optimization techniques were employed to improve the accuracy of visual evaluation and classification. The proposed method offers significant advantages, including the optimization of the cell production process, a reduction in costs, and an improvement in operational efficiency through the minimization of discrepancies between human and machine decisions. Furthermore, this approach facilitates real-time monitoring and dynamic management of production processes by integrating machine learning models with production line databases. The findings indicate the potential of artificial intelligence to enhance the detection and classification of cell defects, thereby supporting more efficient and high-quality solar panel production. The study underscores the importance of AI-driven methods in advancing production technologies and improving the sustainability of solar energy systems.

Keywords : Artificial Intelligence, Machine Learning, Solar Energy, Pv-Photovoltaics, Energy Quality.

1 Introduction

The global and national focus on green energy has intensified significantly, with the goal of achieving sustainable energy solutions by 2050. In this context, various installations and production investments have been initiated, with solar energy emerging as a cornerstone of these efforts. As of the first quarter of 2024, solar energy capacity in Turkey reached an impressive 12,000MW, showcasing the rapid development and prioritization of this sector. Concurrently, industrial investments have also increased, with a particular focus on advancing cell and panel technologies, which play a critical role in enhancing energy efficiency in the sector.

With the growing population and advancing technological infrastructure, meeting the increasing energy demands of households has become essential for ensuring a comfortable lifestyle. Additionally, cumulative energy consumption rates have surged due to the parallel growth of production facility investments. The installation of photovoltaic (PV) electricity generation plants has become crucial in addressing these energy demands. Solar energy production involves a multi-stage process that ensures energy reaches end-users efficiently. This process includes the following four key stages: Silicon production: Silicon, the fundamental material for solar panels, is derived from sand or quartz through metallurgical and chemical purification methods. High-purity silicon is essential for the subsequent production stages. Ingot production: Using the Czochralski method, high-purity silicon is transformed into large cylindrical crystals with a head and tail. Alternatively, polycrystalline ingots are produced by cooling molten silicon in a crucible. Wafer production: The ingots are processed by cutting their head and tail sections using specialized machinery. The remaining cylinder is shaped into a rectangular prism. The edges are trimmed, and the surface is smoothed through chamfering to eliminate cutting marks. Thin slices, approximately as thick as a hair strand, are then cut using diamond wire. From a single ingot measuring 700~800mm in length, approximately 3,000 wafers can be produced. Cell

production: Wafers undergo doping with phosphorus or boron to create a p-n junction, enabling them to generate electricity when exposed to light. An anti-reflective coating is applied to minimize light reflection and maximize light absorption. Metal contacts are added to the front and back surfaces to collect electrical current. The cells are then soldered, coated with various chemicals, and baked to complete the manufacturing process. Following this, the cells are tested using the Halm machine to evaluate their efficiency and parameters. Based on these evaluations, the cells are categorized, labeled, and prepared for module production.

Module production: In this final stage, the cells are arranged in series and parallel configurations on glass substrates. Soldering connects the cells, and a holding material is applied to bind the cells and glass together. The module is laminated to enhance durability. After undergoing quality testing, the modules are labeled and equipped with a frame and j-box cabling, transforming them into ready-to-package solar panels. This study focuses on the application of machine learning in the Halm machine, a critical component in evaluating solar cells during production. By leveraging machine learning algorithms, the system can classify and predict outcomes without requiring explicit programming or manual operator intervention. This approach addresses the challenges of employee turnover, which often leads to disruptions in quality control processes. Machine learning ensures consistency and minimizes errors in interpreting machine data, enabling proactive evaluation and reducing reliance on human intervention. The study employed Decision Trees, Random Forests, K-Nearest Neighbors (KNN), and Linear Regression as primary methods. Balanced data was utilized to ensure reliable outcomes, as each solar cell has defined quality parameters. For instance, unread barcodes are reprocessed without compromising existing data integrity or stability.

The Halm machine is an IV measurement system designed to inspect and classify bifacial solar panel cells on production lines. It features three distinct flash boxes equipped with advanced lighting systems. Initially, the back of the cell is illuminated with $1,000W/m^2$ of irradiation. In the subsequent stage, the cell is adapted to outdoor lighting conditions by simultaneously flashing the front and back of the cell, with the front receiving $1,000W/m^2$ and the back $200W/m^2$. Integrating machine learning algorithms into solar energy production processes offers significant advantages, including improved accuracy, reduced dependency on human expertise, and enhanced efficiency in quality control. By implementing technologies such as the Halm machine, the solar energy sector can achieve greater productivity and contribute more effectively to sustainable energy goals. These advancements underscore the importance of combining technological innovation with renewable energy investments to meet the growing global energy demand.

Figure 1 illustrates the irradiance ranges and time intervals used in the Cell IV Measurement System for evaluating bifacial solar cells. The system employs three distinct measurement conditions: rear STC, outdoor illumination condition, and front STC. Initially, the rear of the cell is exposed to $200W/m^2$ to $1,000W/m^2$ of irradiance for 30 milliseconds, simulating standard rear-side test conditions. Following this, the bifacial condition is tested under outdoor illumination with simultaneous exposure of the front and rear sides for the next 30 milliseconds, where the rear side receives $200W/m^2$, and the front side is exposed to $1,000W/m^2$. Finally, the front STC is measured for the remaining 30 milliseconds, focusing solely on the front side with $1,000W/m^2$ of irradiance. This time-segmented approach ensures comprehensive evaluation of the cell's performance under varying irradiance and directional conditions, providing critical data for classification and efficiency analysis.

Measurement's work integrated with PV Control software and hardware in a control cabinet. The cell measurement system

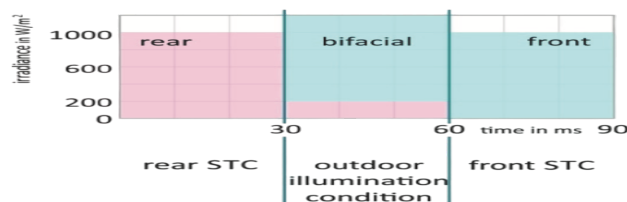


Figure 1: Cell IV Measurement System Ranges

was specially developed for industrial and light industrial use. Advanced hysteresis feature is used here. This is especially designed to be able to classify the next era of innovative cell technologies. Figure 2 depicts the HALM device, a state-of-the-art IV measurement system used for the evaluation and classification of bifacial solar cells in production lines. This device is equipped with advanced hardware and software components, including high-precision measurement units and integrated flash boxes, enabling detailed analysis of electrical parameters and efficiency. The HALM system features a user-friendly interface, as shown on the accompanying monitor, which facilitates real-time monitoring and data visualization. Its modular design ensures scalability and adaptability for various production environments, making it a critical tool in quality assurance and process optimization within the solar energy sector.

In Figure 3, measurements were made with two flash boxes, control units of two monitor cells and a HALM evaluation software PVC as an IV meter. Figure 3 shows a configuration of how test integration is done for a typical cell.



Figure 2: HALM device image

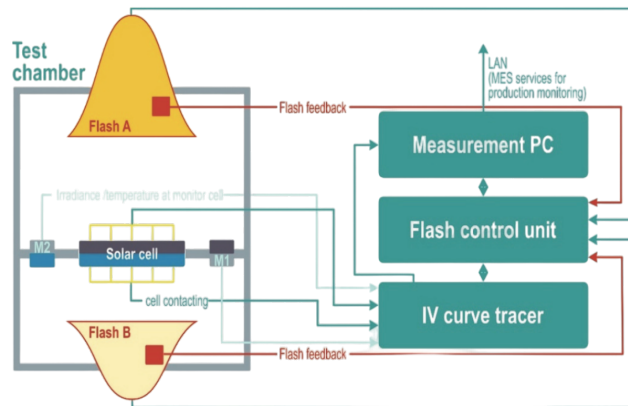


Figure 3: HALM Device Integration

2 Materials

Within the scope of this paper, minimizing operator errors in panel production lines and improving quality processes to increase production cycle efficiency are examined. The focus of the research is on understanding the challenges of faulty quality decisions and delays in production lines. Addressing these issues, the evaluation of machine parameters and quality class decisions presents an opportunity to optimize the workload of employees and improve organizational efficiency. These improvements have the potential to enhance production planning, reallocate human resources to other critical departments, and increase overall productivity. The research utilizes weekly production data from the Cell Production Department at the Kalyon PV factory, obtained using the HALM device. This dataset includes both visual evaluation criteria and efficiency-related parameters. The HALM device, equipped with an industrial automation camera, records images of the cells using a flash and conducts image analysis for visual evaluation. This automated process eliminates reliance on human error, ensuring consistent quality evaluation and accuracy, particularly in managing daily production volumes. By leveraging this technology, the study aims to streamline production processes and enhance overall operational efficiency.

Figure 4 above contains summary information of the processes and flows performed at all stages. The process, which starts with obtaining the data set, consists of pre-processing, analysis, model selection, training, model evaluation, training of the final model, monitoring the model and keeping it updated.

2.1 Provision and Promotion of the Data Set

In the study, the machine measurement parameters values in the data set of the Halm machine of the cell factory located in the Kalyon PV production facility were transferred to our table to be evaluated for inclusion in the production management system.

In the MES (Manufacturing Execution System), a data set comprising 1,288,007 cell parameters, representing one week's production data, was employed for evaluation purposes. This data set is used for cell quality classification and efficiency estimation based on the provided parameters.

The dataset consists of 30 variables identified for analysis, 20 of which are of type (int64) and 10 of type (varchar), all included

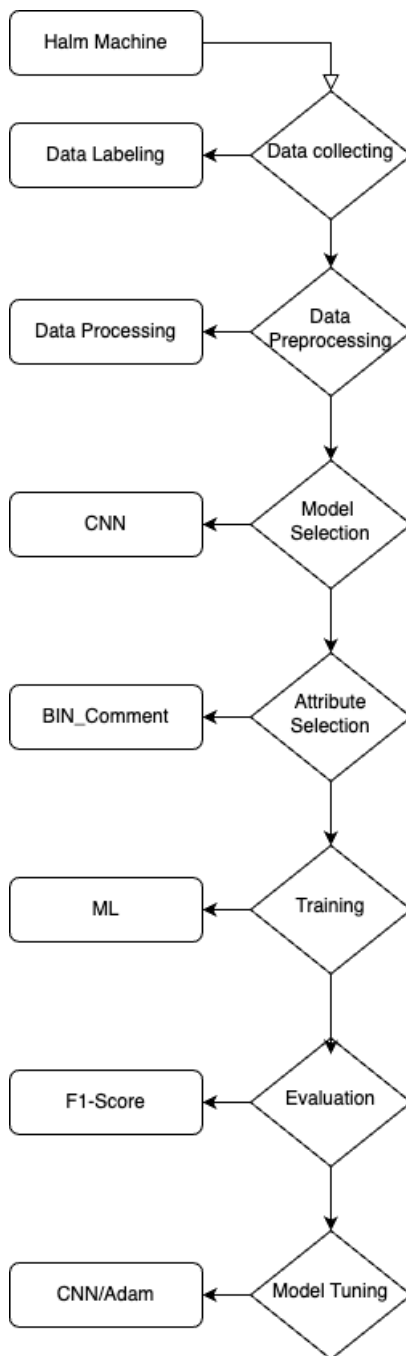


Figure 4: Process Flow Diagram

Table 1: Halm Machine Variables and Description

Variable Name (type)	Description
Measurement Time	Flash Burning Time
Multiple Flash Method	Multiple Flash Reflections
MPP Scanning Method	Full Directional IV Scan
Rheinland Dynamic Current Voltage Value	Cell Type and IV Chart Curve

as columns. Detailed descriptions and names of these columns are provided in the study. Additionally, images backed up within a shared folder structure are integrated into the system for visual evaluation. These images, coupled with the analysis of parameters, enable the identification of quality impacts on final panels and cells. Visual evaluations, performed through advanced image analysis, ensure reliable quality assessments free from human error, further enhancing production efficiency and product consistency.

Table 2: Halm Machine Variables and Description

Variable Name (type)	Description
UniqueID	Halm Makine ID
Title	Title
TestTimeDate	Test Time
BatchID	Batch ID
CellIDStr	Cell Soldering Machine ID
Operator	Operator
Comment	Line Information
BIN	Efficiency Value
Isc	Short Circuit Current
Jsc	Short Circuit Current Density
Uoc	Open Circuit Voltage
FF	Fill Factor
Eta	Efficiency
Impp	Current at Maximum Power Point
Umpp	Voltage at Maximum Power Point
Pmpp	Power at Maximum Power Point
Ivld1	Forward Light Curve
Jvld1	Measurement of Current Density
Ivld2	Measurement of Voltage Density
Jvld2	Measurement of Current Density 2
RshuntLf	Shunt/parallel resistor, forward light
RserLf	Series resistance forward light curve
<i>BINcomment</i>	Quality Class Value

2.2 Transferring Data to the System

After transferring the data set from the machine to the database, after determining the parameters affecting the quality criteria, the necessary database table for the parameters selected for machine learning was created, and with the help of a third-party application named FC, the data was transferred into the table named `h.a.l.m_machine_AI` on Microsoft SQL Server. PyCharm CE development environment was deemed appropriate, and developments were made on this IDE. Code management was carried out systematically via GitHub, as code versions needed to be considered and updated during the process. Additionally, in Microsoft SQL Server, `pandas` and `sqlalchemy` libraries were used to transfer data from the table, and `requests` libraries were used for the API. After these processes, it is brought to the appropriate `.csv` format ready for processing and made ready in the environment for processing. This process provides appropriate conditions for data processing and analysis.

2.3 Digitization of data

In this study, data is also divided into categorical and numerical data. For example, the quality value of a cell appears as categorical data such as (A, B, C). These values are evaluated numerically.

Table 3: Quality Data Set Digitization

Variable Name (type)	Value
A	1
B	2
C	3

2.4 Data visualizations

In order to transfer the log values of the detected errors in Figure 5 to the database and analyze the density of the data, error types can be grouped with the histograms in Figure 6 in order to understand the interpretations related to the numerical properties of the data set.

This section describes the algorithm to detect defects in the EL images of the cell and evaluate the image quality of the solar panels' cells. Quality standards are detailed in accordance with Kalyon PV production standards.

2.5 Pixel based Defects

As shown in Figure 7, pixel-based defects include cracks, finger cuts, and darkness errors. For each of these defects, the algorithm calculates a defect probability for each pixel of the cell. Different threshold evaluations are applied to distinguish various defect types. To evaluate the effect of the pixel being classified as a defect, defect areas are highlighted in white in the corresponding images.

2.6 Cell based defects

Figure 8 illustrates examples of cell-based defects, such as scratches on the cell, ghosting, and o-ring errors. These defects are identified and analyzed in the dataset using the hand image. The visualized examples demonstrate the specific characteristics

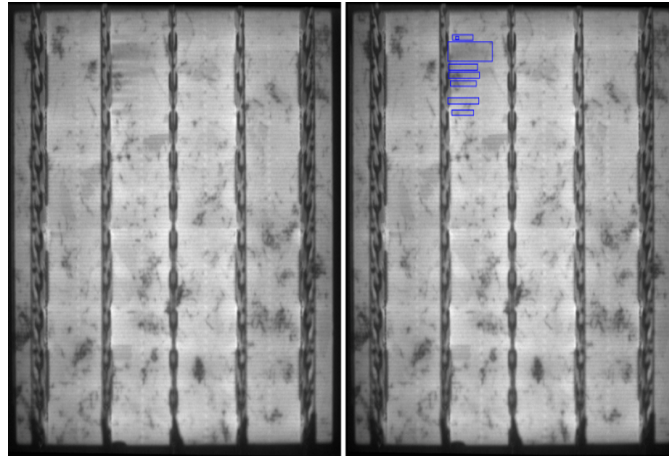


Figure 5: Cell Error Type Example

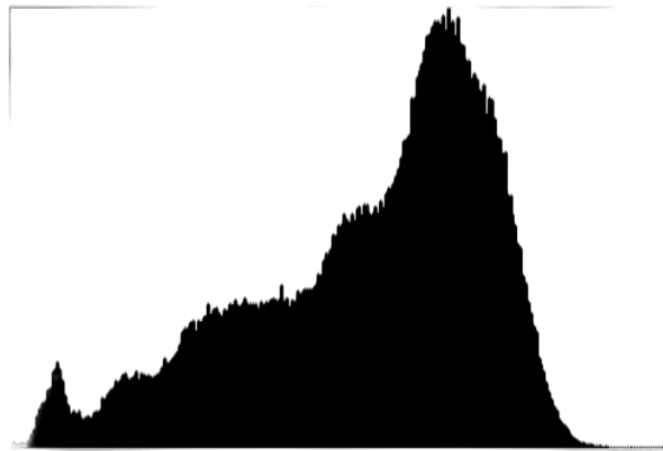


Figure 6: Distribution of Error Types

of each defect type, aiding in accurate defect categorization and evaluation.

3 Methods

3.1 Model Selection

The selection of models suitable for this study involves interpreting the data set and applying traditional machine learning classification and the CNN method to group the data and determine its quality. CNN is one of the most widely used deep learning models for processing visual data and is highly effective in detecting and classifying defects in microscopic images of solar panel cells. Transfer learning, which reuses a model previously trained on large data sets and adapts it to a new problem, is particularly useful for addressing challenges caused by data scarcity in specific areas of solar cell analysis. This approach reduces training time and generally achieves high accuracy rates.

3.2 Feature Extraction (Variable Selection)

In this study, the “BIN_Comment” variable was determined as the target variable, representing the output of the analysis from the evaluated data set. This involves identifying the factors affecting this variable and ensuring that the data set is appropriately formatted for modeling. Correlation is a statistical concept that measures the direction and strength of the relationship between two or more variables. It helps us understand whether a relationship exists between variables, and if so, its direction and strength. The correlation coefficient numerically represents this relationship [1]. **Positive Correlation:** A relationship between two variables where an increase in one variable corresponds to an increase in the other. The correlation coefficient takes a positive value (between 0 and +1).

Negative Correlation: A relationship between two variables where an increase in one variable corresponds to a decrease in the other. The correlation coefficient takes a negative value (between 0 and -1).

Zero Correlation: A lack of relationship between two variables, where the correlation coefficient is 0.

The red line correlation above helps us interpret its influence on the BIN_Comment variable in the evaluation of the cells. It can be used to make decisions regarding the factors affecting this parameter during the analysis stage. These values indicate

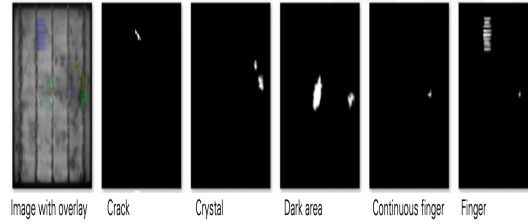


Figure 7: Pixel Based Error Examples

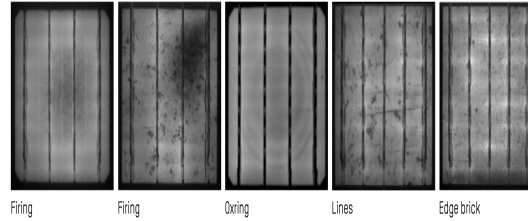


Figure 8: Cell-Based Error Examples

that they will play a significant role in providing insights into which factors have a greater impact on quality classification [2].

3.3 CNN Hyperparameter and Optimization Techniques

This method is a learning architecture that is extremely effective, especially in areas such as image processing and classification. Cell artificial intelligence evaluation can make predictions necessary for learning and identifying cell error types [3].

It consists of four main layers:

- **Convolution Layer:** This layer creates feature maps by applying various filters (kernels) on the input images. Filters detect edges and corners in the image.
- **Activation Function:** After each convolution layer, a non-linear activation function is applied, typically ReLU (Rectified Linear Unit). This helps the model learn complex features.
- **Pooling Layer:** This layer reduces the computational and work costs by decreasing the size of feature maps while preserving important features. The most common pooling operation is max pooling, which selects the maximum value in each subregion.
- **Fully Connected Layer:** This layer receives and evaluates the features obtained from the convolution and pooling layers, increasing the generalization and classification ability of the model.
- **Dropout Layer:** This layer disables random neurons during training to prevent overfitting.

The model visualized in this study was implemented with the help of the Python programming language and its powerful libraries `pandas`, `numpy`, and `sklearn`. These support libraries served as a cornerstone in the creation of the model, enabling the application of various statistical methods and traditional machine learning techniques. During the process, a laptop with a MacBook M2 Operating System and 16GB RAM was used as hardware, and the test environments were carried out on setups installed on this computer.

In this study, five different methods were tried. A total of 1,288,007 data parameters and EL images were evaluated. Following the pre-processing stages specified within the scope of the study, classification analysis was carried out using machine learning methods. In this context, two different analysis methods were chosen to evaluate the results obtained and analyze their accuracy. The compatibility ratio of cell machine values was also evaluated as a criterion. Accuracy, recall, F1-score, and error rate matrices were used in the evaluation process.

Accuracy: It is the ratio of the model's correct predictions to the total predictions. It is used to evaluate overall performance. Its expression is as follows [4]:

$$\text{Accuracy} = \frac{TP + TN}{TP + TN + FP + FN} \quad (1)$$

Recall: It shows how many of the positive examples in real data the model correctly identifies. This is an important criterion, especially in unbalanced data sets [5].

$$\text{Recall} = \frac{TP}{TP + FN} \quad (2)$$

F1-Score: It is the harmonic mean of precision and recall for a model. It is especially useful when working with unbalanced data sets where there are significant differences between classes, as it provides a balanced summary of both metrics [6].

$$\text{F1-Score} = 2 \cdot \frac{\text{Precision} \cdot \text{Recall}}{\text{Precision} + \text{Recall}} \quad (3)$$

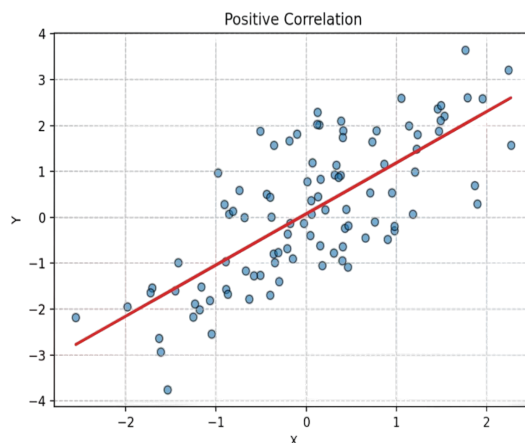


Figure 9: Correlation Heat Plot



Figure 10: Cell Analysis on Panel with CNN model

4 Results and Discussion

We conducted within the scope of the metrics and methods we evaluated, we first prepared the quality groups to evaluate them numerically in the normalization phase, then EL was evaluated for the visual evaluation method, and after a printout was made and made ready for machine learning, machine learning methods were applied [7]. Two different evaluation tables were created to evaluate the methods used. Relevant analysis results for performance evaluation are given in Table 3.

Table 4: Comparison of Machine Learning Methods.

Method	Validation	Precision	Recall	F1 Score
Logistic Regression	0.76	0.75	0.76	0.76
SVM	0.61	0.59	0.61	0.61
Decision Tree	0.59	0.60	0.60	0.60
Random Forest	0.77	0.78	0.77	0.77
CNN	0.82	0.78	0.82	0.82

Evaluation of quality classes taught with real data and comparison of methods are given in Table 5.

As a first step in this study, the relevant machinery, equipment, operating principles, and integration design were detailed. The data for this quality assessment was obtained from the database of the HALM machine, which provides measurement and value assignment in EL images.

In the second stage, a normalization method was applied. Quality values were used to prepare the data for the numerical evaluation of letter outputs. The BIN_Comment field was selected as the key data column, representing the major decision point of the dataset output. This field was considered as an attribute of the data. By evaluating the visual quality output value from the HALM device alongside 20 additional parameter fields, this selection revealed both the quality and efficiency values of the cell. Various machine learning models were employed to evaluate these results [8].

Logistic Regression, Support Vector Machine (SVM), Random Forest, Decision Tree, and CNN methods were applied as traditional and deep learning approaches. The results of these analyses, including the compatibility rates of the data with the actual analysis values, are shown in Table 5. Among these, the CNN method demonstrated the highest compatibility,

Table 5: Comparison of Machine Learning and Deep Learning Methods

BIN_Comment	Logistic Regression	SVM	Random Forest	Decision Tree	CNN
22 A	70.00	69	60	59	71
22.1 A	70.00	64	61	57	74
22.2 A	75.00	63	66	65	84
22.3 A	73.00	65	62	58	69
22.4 A	70.00	67	64	63	69
22.5 A	75.00	69	61	64	78
22.6 A	73.00	66	62	57	83
22.7 A	75.00	68	61	57	74
22.8 A	75.00	62	61	57	70
22.9 A	74.00	68	63	62	81
23 A	74.00	69	61	62	79
23.1 A	74.00	69	65	64	74
23.2 A	71.00	63	62	59	72
23.3 A	74.00	68	64	56	79
23.4 A	72.00	68	61	63	77
23.5 A	74.00	69	65	64	72
23.6 A	74.00	68	61	59	82
23.7 A	70.00	68	61	59	72
23.8 A	70.00	69	62	56	77
23.9 A	71.00	62	61	62	72
24 A	70.00	62	61	62	72

achieving a suitability rate of 78%. This method provided significant contributions to the study by enabling visual evaluation and interpretation of the estimated values [9].

Convolutional Neural Networks (CNNs) are particularly powerful for visual data analysis and classification. Performance is enhanced by selecting appropriate hyperparameters and applying suitable optimization techniques [10]. The CNN model used in this study has the following configuration:

- The first convolutional layer contains 32 filters of size 3×3 .
- The second convolutional layer contains 64 filters of size 3×3 .
- The third convolutional layer contains 128 filters of size 3×3 .
- A 2×2 MaxPooling layer was applied for downsampling.
- A dropout ratio of 0.5 was used to randomly disable 50% of neurons in the fully connected layer to reduce overfitting.
- The ReLU activation function was used in the convolution and flatten layers.
- A sigmoid activation function was used in the output layer for binary classification.
- The input size (`input_shape`) of the model is 64×64 pixels with 3-channel RGB images.
- The Adam optimizer was employed with a learning rate of 0.001 to provide stabilization and increase performance [11] [12].

To diversify the training data, the following data augmentation techniques were applied:

- **Rescaling:** Images were normalized to a range of 0 to 1 by multiplying pixel values by $1/255$.
- **Shear Range:** Images were distorted using shear transformations.
- **Zoom Range:** Images were randomly zoomed.
- **Horizontal Flip:** Images were randomly flipped horizontally.

The training of the model was carried out using the `model.fit` function. The training data was supplied via the `train_generator` object. The following parameters were used:

- `steps_per_epoch`: Calculated by dividing the total number of training data by the batch size.
- `epochs`: The number of times the model trains on the entire dataset, set to 25.
- `validation_steps`: The number of steps per validation step, calculated by dividing the number of validation data by the batch size [13], [14].

Table 4 presents the comparative analysis of various machine learning and deep learning methods for quality assessment in EL image evaluation. Among traditional machine learning methods, Random Forest and Logistic Regression performed well with validation scores of 0.77 and 0.76, respectively. However, CNN outperformed all other methods, achieving the highest validation score of 0.82.

Table 5 further illustrates a detailed comparison across different quality classes. CNN consistently yielded higher accuracy rates, surpassing 82% for several quality bins, while other methods generally achieved scores between 60% and 75%.

The study's methodology, incorporating normalization, hyperparameter optimization, and data augmentation techniques, significantly contributed to the robustness of the CNN model. The findings indicate that integrating advanced machine learning techniques into production processes can enhance quality control mechanisms, improve resource utilization, and increase production efficiency in the photovoltaic industry [15]–[18].

Authors' Contributions

Murat Simsek: Conceptualization, Methodology, Software. Ozel Sebetci: Data curation, Software, Writing - original draft. Irfan Yilmaz: Software, Writing - original draft.

Competing Interests

The authors declare that they have no conflict of interest.

References

- [1] W.-C. Hong, P.-F. Pai, Y.-Y. Huang, and S.-L. Yang, "Application of support vector machines in predicting employee turnover based on job performance," in *Advances in Natural Computation*, 2005, pp. 668–674.
- [2] B. L. Aylak, O. Oral, and K. Yazıcı, "Yapay zeka ve makine Öğrenmesi tekniklerinin lojistik sektöründe kullanımı," *El-Cezeri Journal of Science and Engineering*, vol. 8, no. 1, pp. 74–93, 2021.
- [3] M. A. Green, *Solar Cells: Operating Principles, Technology, and System Applications*. University of New South Wales Press, 2018.
- [4] E. E. Antunez, J. Gonzalez-Hernandez, and A. Dominguez, "Artificial neural network modeling of a photovoltaic panel considering temperature effects," *International Journal of Energy Research*, vol. 43, no. 12, pp. 5939–5950, 2019.
- [5] H. H. Al-Kayiem and Z. S. Al-Khafaji, "Modeling and optimization of photovoltaic cells using artificial neural networks: A review," *Renewable and Sustainable Energy Reviews*, vol. 82, pp. 1811–1820, 2018.
- [6] Y. Ma, Y. Yang, X. Yu, Y. Chen, and F. Blaabjerg, "Artificial intelligence for energy management in future smart grids: A review," *Renewable and Sustainable Energy Reviews*, vol. 104, pp. 62–72, 2019.
- [7] X. e. a. Liu, "Automated defect detection for photovoltaic modules using convolutional neural networks," *IEEE Transactions on Industrial Informatics*, 2020.
- [8] M. Garcia *et al.*, "Principal component analysis for solar cell defect detection," in *Procedia Manufacturing*, 2018, pp. 34–49.
- [9] A. Radford, K. Narasimhan, T. Salimans, and I. Sutskever, "Improving language understanding by generative pre-training," 2018.
- [10] S. Sharma *et al.*, "Random forest-based approach for solar cell quality prediction," *Renewable Energy*, pp. 3–7, 2017.
- [11] J. Zhang *et al.*, "Transfer learning for defect detection in solar cells using deep convolutional neural networks," *Solar Energy*, 2019.
- [12] D. P. Kingma, "Adam: A method for stochastic optimization," 2014, arXiv preprint.
- [13] F. Itano, M. A. de Abreu de Sousa, and E. Del-Moral-Hernandez, "Extending mlp ann hyperparameters optimization by using genetic algorithm," in *Proceedings of the 2018 International Joint Conference*, 2018, pp. 66–67.
- [14] K. Ramspeck, S. Schenk, L. Komp, A. Metz, and M. Meixner, "Accurate efficiency measurements on very high efficiency silicon solar cells using pulsed light sources," in *Proceedings of the 29th European Photovoltaic Solar Energy Conference and Exhibition*, 2014, pp. 1253–1256.
- [15] Z. Lu and J. Wu, "A review of artificial intelligence applications in marine renewable energy systems," *Renewable and Sustainable Energy Reviews*, vol. 117, p. 109469, 2020.
- [16] C. Monokroussos, R. Gottschalg, A. N. Tiwari, G. Friesen, D. Chianese, and S. Mau, "The effects of solar cell capacitance on calibration accuracy when using a flash simulator," in *Proceedings of the 4th WCPSEC*, vol. 2, 2006, pp. 2231–2234.
- [17] C. Y. J. Peng, K. L. Lee, and G. M. Ingersoll, "An introduction to logistic regression analysis and reporting," *The Journal of Educational Research*, vol. 96, no. 1, pp. 3–14, 2002.
- [18] G. Rong, G. Mendez, E. B. Assi, B. Bajic, and N. V. Chawla, "Understanding sbml's flat line: An analysis of loss functions for oversampling-based classifiers in imbalanced datasets," in *Proceedings of the AAAI Conference on Artificial Intelligence*, vol. 34, 2020, pp. 5372–5379.

Research Article

Investigation of Factors Affecting Motif-Based Short- and Long-Term Memory Behaviour in Brain Neuron Networks

Ahmet Turan^{1a}, Temel Kayıkçıoğlu^{2b}

¹ Biomedical Engineering Department, Samsun University, Samsun, Türkiye

² Electrical and Electronics Engineering Department, Karadeniz Technical University, Trabzon, Türkiye

ahmet.turan@samsun.edu.tr

DOI : 10.31202/ecjse.1523210

Received: 27.07.2024 Accepted: 19.10.2024

How to cite this article:

Ahmet Turan, Temel Kayıkçıoğlu, " Investigation of Factors Affecting Motif-Based Short- and Long-Term Memory Behaviour in Brain Neuron Networks", El-Cezeri Journal of Science and Engineering, Vol: 12, Iss:1, (2025), pp.(54-65).

ORCID: "0000-0001-5653-9656; ^b 0000-0002-6787-2415.

Abstract : Learning and memory formation in living things is a subject under investigation. It is thought that the memory formed in the brain's neural network structure is closely related to the connections between neurons. Connections called "motifs" have been identified, usually consisting of three or four neurons and repeating within the neural network. The basic structure of biological memory is thought to be related to such repetitive neural connections. In this study; the effect of the structures of motifs on short- and long-term memory was examined for all triple-neuronal network motifs. We used the Hodgkin-Huxley model of neurons. Using graph theory, we generated all triple-neuron motifs. In the created motifs; the effects of synaptic inputs between neurons, types of synaptic inputs of neurons, and chemical synapse duration on short- and long-term memory were examined. From the data obtained in all triple-neural network motif models; from the structure of the motif and the type of synaptic input, we determined the status of long- and short-term memory. We classified all triple-neural network motifs for situations in which they exhibit short- and long-term memory behaviour. We show that short-term memory varies with synaptic connection duration

Keywords : Brain neural network motifs, intercellular synaptic type, short-term memory, synaptic conductivity time, long-term memory

1 Introduction

How learning occurs in living things is investigated by biological experiments and computational methods. In order to elucidate this issue, studies on neuronal connections are being made [1] Intercellular synaptic inputs are being studied [2]. The connections formed between neurons are considered to be an important factor in memory formation. In order to support these studies, studies describing neural network structures have been carried out [3]. In fact, brain neuron network connection maps of some living things have been obtained [4]–[10]. These network maps, which are also the graphical representation of dynamic systems, are used to analyse the complex structures of biological systems [5]. The behaviour of neurons forming the networks in the learning process has been followed by biological studies and important data have been obtained [11]. It has been observed in biological experimental studies that while living things are learning, new connections are established between neurons, some of which are temporary and some are permanent [12]–[18]. Changes related to the learning process have been observed in the dendrites of neurons [19]. In these studies, it was also observed that some interneuron connections detected in neuronal networks were frequently repeated within the network. These special-function subnet links are named "Network motif". [4], [6]–[8], [13], [20]–[23]. Here the term "Network motif" refers to directed subgraphs. Motifs containing such triple-neurons are common in many biological environments [1]. These network motifs are modelled by computational neuroscience studies and their roles in their environments are investigated [24], [25]. Computational neuroscience uses computational techniques to model neural networks [26]–[28]. Thus, the functions of network motifs are investigated by means of computational models [7], [19]. It is thought that biological memory systems where learning takes place include such network motifs with memory capability [15]. Neurons in triple neural network motifs are usually; are named as input, output and driver neurons [7], [29]. It is thought that especially interneuron connections are effective in the formation of long and short-term memory [30]. Short-term memory, where thinking and information processing takes place, is considered to be the most functioning part of memory [26]. It is considered that the type of synaptic input between neuron groups is effective in the functioning of short-term memory, which is one of the important parts of memory. It is thought that storing information in long-term memory is possible with permanent, functional,

biochemical and structural changes that occur in neural connections in the brain [16], [31]–[33]. Experimental studies have shown that neurons are electrically active and usually communicate via chemical synapses. Chemical synaptic communication between neurons has also been modelled mathematically [34]. In some modelling studies, the responses of motifs to stimuli have been interpreted as short- and long-term memory behaviour. In these studies; some special network motif constructs and simpler neuron models (such as the Integrate and Fire Neuron Model) are used. For the synaptic input between neurons, a noise signal was applied to the postsynaptic cell, representing signals from other neurons. In some models, the synaptic weight parameter was used to express the total synaptic input to the dendrites [7]. All these studies have not yet fully revealed how learning takes place. How long- and short-term memory formation, learning, remembering, and forgetting occur in neurons is being investigated [35]. During learning, synaptic input changes were observed between neurons. Although this suggests that connectivity is effective in learning, the occurrence of this change has not been fully explained [36]. While Biological studies investigate the adaptive changes of the brain during learning, on the other hand, computational neuroscience studies try to model the learning process. The parameters that are effective in the retention of information during and after the learning process have not been fully explained. Understanding the learning functions of the brain will benefit the diagnosis and treatment of many diseases [37]. When the motif behaviours are learned, the properties of the network environments to be obtained by motif multiplexing can also be learned [38]. Although the behaviour of some neural network motifs has been investigated, especially in connectivity studies, there is no comprehensive motif model study. In addition, in learning research; no detailed studies on motif structure, intercellular synaptic entry type and synapse duration have been performed. The findings of our study will reveal the analysis of all triple neural network motifs on the effect of connectivity in learning. Our work; it is based on the thesis that learning is directly related to the type of synaptic input and motif structures between neurons. To this end, we examined some factors that affect the short- and long-term memory behaviour of all three-neuron motifs. Using graph theory, we systematically constructed all three-neuron motifs. First, we studied the basic motif connections, which are used in many studies in the literature. In these studies, the effect of synaptic input types of neurons was revealed. Considering the findings obtained here, the memory behaviour of triple neural network motifs was studied. Motifs were evaluated considering neuron roles. In the studied motifs, after the learning information was given to the input neuron in the form of electrical signals, the electrical effect on the output neuron was examined. The persistence of the output signal (action potentials) was interpreted as long-term memory behaviour, and its temporality (ending after a while) was interpreted as short-term memory behaviour. With this approach, we examined short- and long-term memory behaviour in motifs, across all possibilities of neurons' synaptic input types. We also studied the effect of time constant variation in the interneuron chemical synapse model on short-term memory duration. The prolongation of the synapse duration was made by increasing the time constant of the model. This means that one neuron continues to excite the other. In these studies, how learning happens is evaluated in terms of connectivity. Thus, it is aimed to contribute to the solution of neurological diseases such as learning problems, forgetting, memory loss, dementia, Alzheimer's, etc. From the findings of the study, it has been shown that memory formation is highly related to the following factors:

- With the interneuron connections that form the neural network motifs,
- With synaptic input types between neurons,
- With the duration of synapse between neurons.

2 Materials and Methods

The deterministic Hodgkin-Huxley neuron modelling method used in our study is one of the most basic and successful models. Modelling was performed in the MATLAB software environment.

2.1 Modelling of Neuron and Neural Network Motifs

In our study, we used Hodgkin-Huxley's neuron model, which is frequently used in many studies, to model the neurons forming the motifs. While the neuron was modelled as a single compartment of the soma and deterministic, signal transmission between neurons was modelled as a chemical synapse [39]–[43]. Synaptic inputs between neurons; were added to the electrical model with excitatory (E) or inhibitory (I) potential values [34], [40], [44]. In triple neural network motifs, in addition to external current input to neurons, synaptic input is made from one or two neurons depending on the motif structure. The electrical models of neurons according to the inputs they receive are shown in Figure 1 [40]. Ion channels in the cell membrane of the neuron are responsible for its electrical behaviour. These channels allow the neuron to generate an action potential. E_{Na} , E_K , E_L expressions are among the parameters in the electrical solution of the model, the equilibrium potentials of the ion channels. V_m is neuron membrane voltage, V_r is neuron membrane voltage at rest, C_m is neuron membrane capacitance. G_{Na} , G_K conductivity values of sodium Na^+ and potassium K^+ channels G_{Na} , G_K , maximum conductivity in the neuron membrane, G_L is leakage current conductivity equation (16-17). In the model, for the Na^+ ion channel, three identical activations m^3 and one inactivation gate (h) and the ion K^+ is defined with four identical activations n^4 gates equation (13-15). The voltage-dependent transition rate constants between the open-and-close states of an ion channel are defined as: α_{V_m} and β_{V_m} equation (2-9). Steady-state

activation of Na^+ current is defined as m_∞ , inactivation as h_∞ and steady-state activation of K^+ current is defined as n_∞ equation (10-12). The solution of the single-compartment neuron modelled with the electrical circuit shown in Fig.1-a is given in equation 1.

$$C_m(dV_m)/dt = -G_L(V_m - E_L) - G_{Na}(V_m - E_{Na}) - G_K(V_m - E_K) + Iinj(t) \quad (1)$$

$$\alpha_m = \left(\frac{-0.1(V_m - V_r - 25)}{\exp(-(V_m - V_r - 25)/10) - 1} \right) \text{ whereas } V_r - V_m > 24, 99 \quad (2)$$

$$\alpha_m = \left(\frac{-1}{\exp(-(V_m - V_r - 25)/10)} \right) \text{ whereas } V_r - V_m \leq 24.99 \quad (3)$$

$$\beta_m = 4(\exp(-(V_m - V_r)/18)) \quad (4)$$

$$\alpha_h = 0.07(\exp(-(V_m - V_r)/20)) \quad (5)$$

$$\beta_h = \left(\frac{1}{1 + \exp(-(V_m - V_r - 30)/10)} \right) \quad (6)$$

$$\alpha_n = \left(\frac{0.01(V_m - V_r - 10)}{1 + \exp(-(V_m - V_r - 10)/10)} \right) \text{ whereas } V_r - V_m > 9.99 \quad (7)$$

$$\alpha_n = \left(\frac{0.1}{\exp(-(V_m - V_r - 10)/10)} \right) \text{ whereas } V_r - V_m \leq 9.99 \quad (8)$$

$$\beta_n = 0.125(\exp(-(V_m - V_r)/80)) \quad (9)$$

$$m_\infty(V_m) = \alpha_m(V_m)/(\alpha_m(V_m) + \beta_m(V_m)) \quad (10)$$

$$h_\infty(V_m) = \alpha_h(V_m)/(\alpha_h(V_m) + \beta_h(V_m)) \quad (11)$$

$$n_\infty(V_m) = \alpha_n(V_m)/(\alpha_n(V_m) + \beta_n(V_m)) \quad (12)$$

$$\frac{dm}{dt} = \alpha_m(V_m)(1 - m) + \beta_m(V_m)m \quad (13)$$

$$\frac{dh}{dt} = \alpha_h(V_m)(1 - h) + \beta_h(V_m)h \quad (14)$$

$$\frac{dn}{dt} = \alpha_n(V_m)(1 - n) + \beta_n(V_m)n \quad (15)$$

$$G_{Na} = \bar{G}_{Na}m^3h \quad (16)$$

$$G_K = \bar{G}_Kn^4 \quad (17)$$

Neurotransmitter-activated ion channels, which are electrically excited when synaptic input arrives in the interneuron connection, are defined by time-dependent $gsyn(t)$ conductivity, as seen in equation (18) [45]. The synaptic communication current of the model we used is shown in equation (20), and the addition of the current to the electrical circuit is shown in Figure 1(d). Dynamics involving multiple synaptic inputs to a neuron, that is, multiple synapse inputs, are as shown in equation (20) [40]. Neural network motifs are created with neurons communicating with this method.

$$gsyn(t) = g_{max} \frac{t}{\tau} e^{(1 - \frac{t}{\tau})} \quad (18)$$

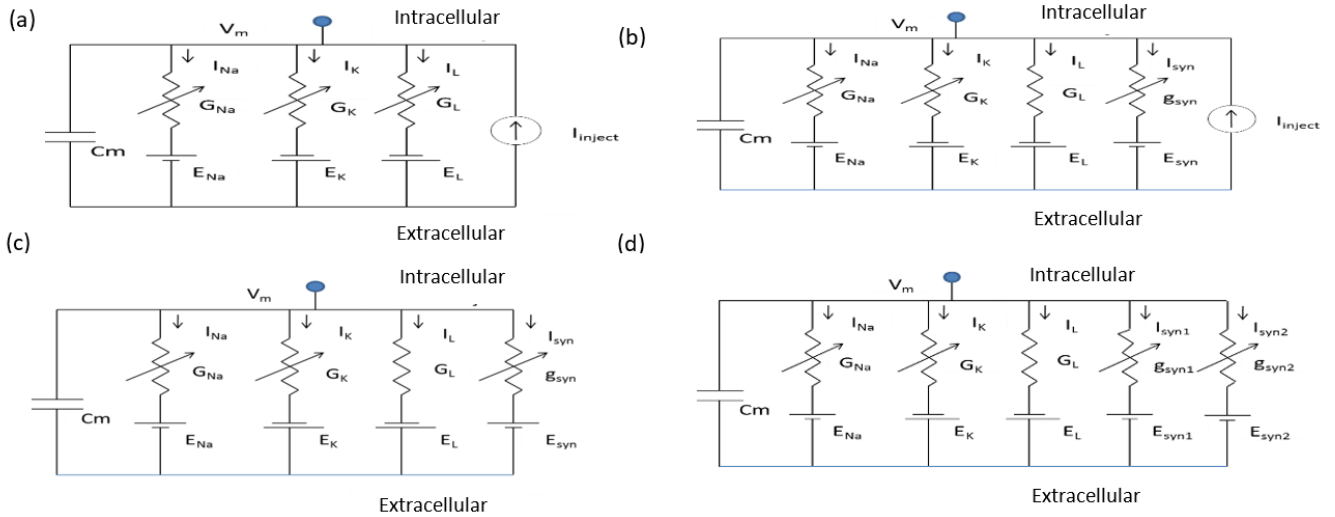


Figure 1: (a) Neuron model with only external current input. (b) Neuron model with external current input and single synaptic input. (c) Neuron model with only one synaptic input. (d) Neuron model with two synaptic inputs

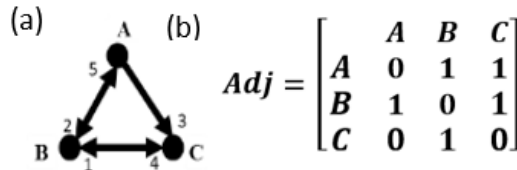


Figure 2: (a) Directed motif comprising 3-neuron and 5 links. (b) Adjacency matrix Adj.

$$I_{syn}(t) = g_{syn}(t)(V_m - E_{syn}) \tag{19}$$

$$C_m \frac{dV_m}{dt} + g_{rest} V_m + g_{syn}^{(1)}(t)(V_m - E_{syn}^{(1)}) + g_{syn}^{(2)}(t)(V_m - E_{syn}^{(2)}) + \dots = 0 \tag{20}$$

The parameters obtained from the biological experimental studies of Hodgkin-Huxley were used in the motif models. Commonly used model parameter values $G_{Na} = 120ms/cm^2$, $G_K = 36ms/cm^2$, $G_L = 0.3ms/cm^2$, $E_{Na} = 50mV$, $E_K = -77mV$, $E_L = -54.4mV$, $C_m = 1\mu F/cm^2$, $V_r = -65mV$. In synaptic input reversal potentials were used as: $E_{syn} = -70mV$ for inhibitor (I), $E_{syn} = -10mV$ for excitatory (E), maximum synaptic conductivity $g_{max} = 64nS$, synaptic conductivity time constant $\tau = 25ms$ [45]–[47]. For numerical solutions of Euler differential equations, the time step interval was chosen as $\Delta t = 10\mu s$. To model neuron and neural network motifs, we created simulation software using these parameters suitable for experimental studies. In our study, the Hodgkin-Huxley model, which contains more parameters and is closer to the behaviour of the neuron, was preferred for neuron modelling. In experimental studies on neurons communicating with chemical synapses; it has been observed that when the synaptic input type of the presynaptic neuron is Excitatory (E), action potentials are formed in the postsynaptic neuron. It has been observed that when the synaptic entry type is blocker (I), it prevents the formation of action potentials.

2.2 Generating All Triple-Neuron Brain Network Motifs Using Graph Theory

Graph theory is a mathematical method used to model complex biological systems. Graphs can be directed, undirected, and mixed. Directed graphs are often used to model biological neural networks. The interconnections of neurons can be described by the adjacency matrix (Adj). In this matrix, (1) shows a connection between neurons and (0) shows no connection [5], [29], [48]. The analysis of complex networks and the concept of network motifs is a subject studied in many fields of study [49], [50]. Figure 2 shows a directed graph motif and its adjacency matrix for its synaptic input directions (arrowheads). It has been found that the neuronal connectivity forming the motif is much stronger than the connections they make with other neurons. This brings to mind the idea that the motif structure is specialised for a purpose. The network motifs probably protect the behaviour they display alone when they are connected to other neurons. In all motifs, we consider (A) as the input neuron, (C) as the output neuron and (B) as the generally drive neuron (C) [7]. In our study; recognizing the input (A), output (C) and driver (B) roles of neurons, we systematically constructed all triple-neuron motifs using the adjacency matrix method of graph theory. In

MOTIF NAME AND CONNECTION TYPE							
MTF1 	MTF2 	MTF3 	MTF4 	MTF5 	MTF6 	MTF7 	MTF8
MTF9 	MTF10 	MTF11 	MTF12 	MTF13 	MTF14 	MTF15 	MTF16
MTF17 	MTF 18 	MTF19 	MTF20 	MTF21 	MTF22 	MTF23 	MTF24
MTF25 	MTF26 	MTF27 	MTF28 	MTF29 	MTF30 	MTF31 	MTF32
MTF33 	MTF34 	MTF35 	MTF36 	MTF37 	MTF38 	BMTF1 	BMTF2

Figure 5: All directed triple neuron brain network motifs were generated using graph topology.

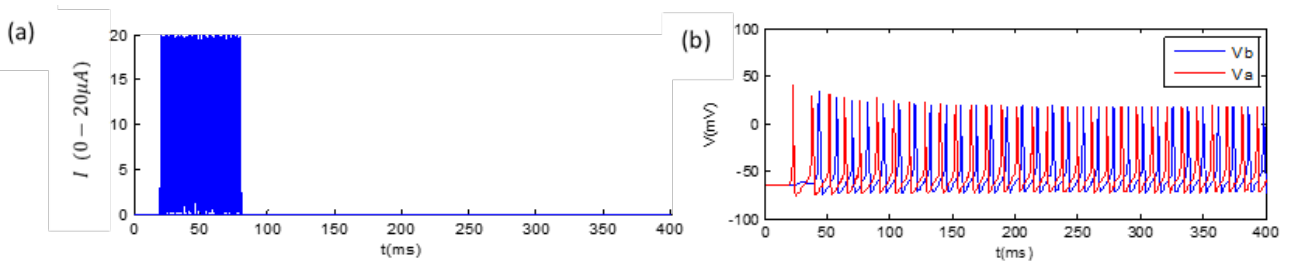


Figure 6: (a) Uniformly distributed random current applied externally to the A neuron. (b) Action potentials generated in A and B neurons when the neurons have synaptic input type (AB-EE).

and long-term memory behaviour of several triple- and quadruple-neuron network motifs has been investigated [52]. In studies conducted in this area, models with fewer parameters have been preferred in terms of ease of processing to model neuron [7], [53]. In previous studies, short- and long-term memory behaviour of some motifs comprising three neurons was investigated. In these studies, it has been shown that neurons form short- or long-term memory depending on the type of synaptic input. In the action potential graphs seen in the motif output cell, it is assumed that the motifs that continue to produce the output signal after the external current stimulus to the input neuron is interrupted show long-term memory behaviour. Graphic images that generate output signals for a while after the external current warning is interrupted are also considered as short-term memory [7]. By modelling this behaviour in our study, we examined memory behaviours in all possibilities of excitatory-inhibitory states of synaptic inputs of neurons, of all motifs obtained by graph theory. For this purpose, we examined the short- and long-term memory formation states of all motifs in Table 1 for these possibilities. To better evaluate the effect of motifs on the memory behaviour of the intercellular connection pattern and the type of synaptic input of the neurons (Excitatory-E, $E_{syn} = -10mV$ Inhibitor-I, $E_{syn} = -70mV$, we studied the basic motif (BMTF2) in Fig. 5. In BMTF2 basic connection; neuron A is modelled with the circuit in Figure 1(b) and neuron B is modelled with the circuit in Figure 1(c). Neuron A receives both external stimulation current and synaptic input from neuron B. B neuron only receives synaptic input from A neuron. In the experiments, the uniformly distributed random current form, which is shown in Fig.6.(a) and represents the total excitation from the dendrites to the soma, can be used as the external input current. When the synaptic input types of A and B neurons are selected as excitatory (AB - EE), action potentials continue to occur in both A and B neurons, although the external current input is cut off. A time shift (phase difference) occurs between the voltages V_a and V_b seen in Fig. 6.(b). This is because neurons A and B have reciprocal synaptic inputs and both types of synaptic input are excitatory. In the same structure; when the synaptic input type is (AB -EI), (AB-IE) and (AB-II), action potential generation ends when the external current input is cut off. When only one of

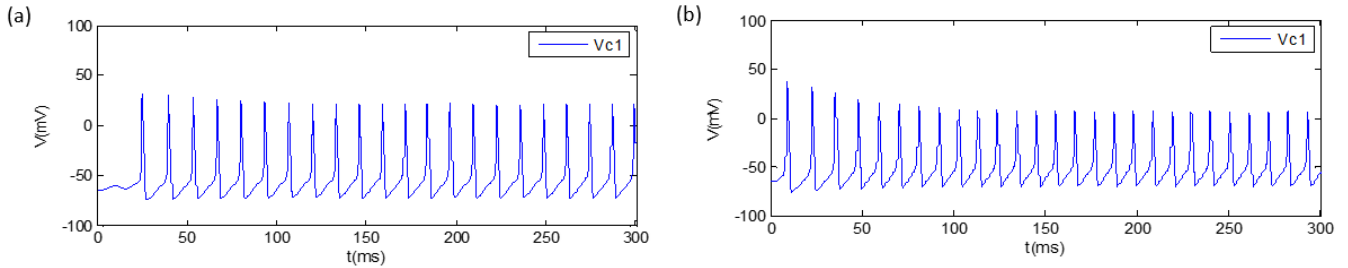


Figure 7: In MTF1 motif, external current input ($10\mu A$ - DC); (a) when applied to A neuron only, (A \rightarrow C, E) action potentials generated in C neuron (b) When applied to both A and B neurons, (AB, EE) action potentials generated in C neuron.

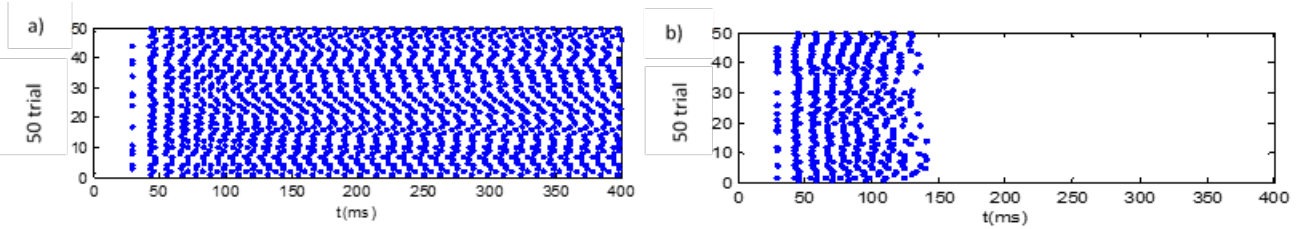


Figure 8: When the external current in Figure 3(a) is applied to the A neuron in the MTF8 motif; (a) raster plots of action potentials generated in C neuron in each of 50 trials when synaptic input types (ABC-EEE), (b) raster plots of action potentials generated in C neuron in each of 50 trials when synaptic input types (ABC-EEI) are present.

the A or B neurons is stimulated by an external direct current (DC) input ($10\mu A$ - DC), an action potential occurs in the neuron. These action potentials, which are formed in the A or B neuron under the influence of the external current, are transmitted to the C neuron as synaptic input (AB-EE). Thus, a sequence of action potentials is observed in the C neuron at a frequency of $f=68\text{Hz}$, shown in Figure 7(a). When both neurons A and B are stimulated by external direct current input, action potentials are generated in both neurons. Thus, the action potentials of the two neurons are transmitted simultaneously to the C neuron as synaptic input (AB-EE), and the action potential sequence is observed in the C neuron at a frequency of $f=72\text{Hz}$, shown in Figure 7(b). The reason for the increase in frequency is that the neuron receives more than one synaptic input. When A and B neurons have synaptic input type (AB-EI, etc.) to C neuron; as one of them is excitatory (E) and the other is inhibitor (I), the inputs cancel each other's effect. Thus, no action potential occurs in the C neuron. With these studies; we have examined the effect of intercellular connection type and synaptic input type. This study was carried out for all motifs in Fig. 5. As an example, we have shown the studies on the motif we named MTF8 in Fig. 5. First synaptic input type for all neurons in the motif were selected as excitatory (E) (ABC-EEE). The current shown in Figure 6(a) is applied to neuron A as an external current. The same application was repeated 50 times to show the difference in the action potential generation time in the C neuron. This difference is due to the randomness of the external current applied to the input neuron. Fig. 8. (a) shows a raster graph showing the action potential generation times in one line for each of the 50 trials. This graphical representation is the preferred method for describing short- and long-term memory behaviour. When the stimulus current is random and uniformly distributed, the time of the current magnitude that will generate the action potential is variable. Such a current application is for modelling that the neuron has been excited externally by an electrical signal of random time and magnitude. Although the external current application was cut off after 80ms, action potentials continued to occur in neuron C as seen in Fig. 8. (a). This is interpreted as the motif exhibiting long-term memory behaviour. In the same motif, action potentials continued to be produced in the C neuron for 60ms after the external current application, when the neurons stimulus types (ABC-EEI) were made. This, seen in Figure 8(b), is interpreted as the short-term memory behaviour of the motif. For other possibilities of warnings, these applications were repeated. In these excitation states (ABC-III, IIE, IEI, IEE, EII, EIE) the motif did not show both memory behaviours. We performed these applications for all motifs in Fig. 5. From the results obtained, the situations in which the motifs show memory behaviour were determined and shown in Fig. 9. in the conclusion part.

2.4 Investigation of the Effect of Change in Chemical Synapse Conductivity Function Time Constant Parameter on Short-term Memory Time

The time constant parameter of the synaptic conductivity function $g_{syn}(t)$ (equation 18) in intercellular synaptic input, the model is associated with the synaptic input duration. This function is defined with a time-dependent exponential function so that the sum of the impulses coming to the dendrites creates an action potential in the neuron. Synaptic input current $I_{syn}(t)$; is the product of the conductivity value $g_{syn}(t)$ and the difference $V_m - E_{syn}$ of the cell membrane voltage V_m and the synaptic excitation threshold voltage E_{syn} (equation 19). As can be seen here, as the time constant of the conductivity value increases,

Motif Name	Synaptic Input Type				F	Motif Name	Synaptic Input Type					F	Motif Name	Synaptic Input Type						F	Motif Name	Synaptic Input Type						F					
	1	2	3	4			1	2	3	4	5			1	2	3	4	5	1			2	3	4	5	6	1		2	3	4	5	6
MTF30	E	E	E	E	75	MTF20	E	E	E		69	MTF19	E	E	E		69	MTF13	E	E	E	E	E	E	75	MTF28	E	E	E	E	E	E	79
	E	I	E	E	75		MTF21	E	E	E			69	MTF22	E	E	E			78		E	E	E	E		I		77				
	I	E	E	E	69		MTF34	E	E	E	E		E	69	MTF4	E	E		E		74		E	E	E		E	I	E	69			
	I	I	E	E	69		MTF7	E	E	E			74		E	E	I			75		E	E	E	E		I	I	74				
MTF8	E	E	E	E	83		E	E	I		75	MTF24	E	E	E		74		E	E	E	I	E	E	66		I	I	E	E	E	74	
MTF11	E	E	E	E	80	MTF27	E	E	E	E	70		I	E	E		70		E	E	I	E	E	E	69		I	I	E	I	E	74	
MTF6	E	E	E	E	69		E	E	E	I	70	MTF36	E	E	E	E	74		E	E	I	E	E	I	75	MTF12	E	E	E	E	E	79	
	I	E	E	E	69	MTF29	E	E	E	E	E	81		E	E	E	I	74	MTF17	E	E	E	E	E		83		E	E	E	E	I	69
MTF26	E	E	E	E	79		E	E	E	E	I	75	MTF15	E	E	E	E	69											E	E	E	I	E
	E	E	I		69	MTF14	E	E	E		69		I	E	E	E	74		E	I	E	E	I		68		E	E	E	I	I	75	
MTF32	E	E	E	I	69		E	E	I		74		I	E	E	I	69		I	E	E	E	E		78		E	I	E	E	E	69	
	E	E	E	E	69		E	I	E		73	MTF35	E	E	E	E	69		I	E	E	E	I		78		E	I	E	E	I	69	
MTF10	E	E	E	E	80	MTF38	E	E	E	E	75		I	E	E	E	79		I	E	I	E	E		74		E	I	I	E	E	69	
	I	E	I	E	79			E	E	E	I	74		I	E	E	I	69		I	E	I	E	I		74		E	I	I	E	I	78
	I	E	E	E	74			E	I	E	E	79	MTF16	E	E	E	E	79	MTF31	E	E	E	E	E	69	MTF33	E	E	E	E	E	63	
MTF9	E	E	E	E	75		E	I	I	E	77		E	I	E	E	79			E	I	E	E	E	69		E	E	E	E	I	69	
	E	E	E	I	74								I	E	E	E	69		E	I	E	E	I		78		E	E	E	I	E	69	
	I	E	E	E	74								I	I	E	E	84		I	E	E	E	E	80		E	E	E	I	I	69		
	I	E	I	E	74														I	I	E	E	E	78		I	I	E	E	E	78		
TMTF_2	E	E			79													I	I	E	E	I	69		I	I	E	E	I	69			

Figure 9: Of the motifs in Fig.5., those showing long-term memory behaviour; (numbers above motifs indicate synaptic input, numbers in the figure indicate synaptic input type) representation of neurons with probabilities of synaptic input types and frequency of action potential produced in neuron C

the exponential decay time of the conductivity gets longer. The larger the time constant of the function, the longer a synaptic input state occurs between neurons. Time constant variation has been studied with simpler models in a few four-cell motifs in the literature [7]. In these modelling studies; the synaptic conductivity time constant has been shown to affect short-term memory duration in appropriate Motifs [53]. While chemical synapses are formed between neurons, physical changes occur in dendritic spines [54]. In our study; we examined the effect of synaptic conductivity time constant variation on short-term memory duration in triple-neuron motif models. For the appropriate motifs in Fig. 10., we show that the short-term memory duration changes with the change of the neurons communication function time constant. In the experiments in the first chapters, the time constant value of the interneuron synaptic conductivity function in the motifs was taken as $\tau = 25ms$. In this part of our study, we examined the short-term memory duration of the neuron at certain values by making the time constant (τ) variable. Studies in this section were carried out on the MTF8 motif.

3 Results

3.1 Identification of Triple Neuron Network Motifs, which are Long-Term Memory

We studied the effect of all probabilities of the intercellular synaptic input types (E or I) on memory behaviour in all motifs seen in Fig. 5. For all motifs, we repeated the work described in section 2.3. These motifs were simulated for all intercellular synaptic input type possibilities, and their long-term memory status was shown in Fig. 9. . Fig. 9. also shows the frequency (f) of the continuous action potential signal formed in the C output neuron. It is seen that the action potential frequency is close to each other in different motives and situations. If the output neuron receives more than one synaptic input, due to the motif structure, the output signal frequency is slightly increased. We have placed this in the table to express the continuity of the signal. With the synaptic flexibility in the learning process, when such synaptic input types occur between neurons, it is considered that the information is stored for the long-term. This study also revealed that intercellular connectivity and synaptic entry type play a very important role in motif analysis. Findings from this part of the study revealed a common feature of triple-neuronal network motifs displaying long-term memory behaviour. It has been determined that the intercellular connections of these motifs form a closed loop (in the form of A-C or A-B-C) reaching the output neuron. In the case of appropriate intercellular synaptic input type, such a loop-forming motif connection can retain information long-term even if the total synaptic input applied to the A neuron is interrupted. Among the motifs in Fig. 5., those with long-term memory are shown in Fig. 9. Examples of those listed in Fig. 9. are MTF30; 4 synaptic entries in the order in the figure (EEEE, EIEE, IEEI, IIEE) become long-term memory, MTF13; the 6 synaptic inputs, in the order in the figure (EEEEEE, EEEEEI, EEEEEIE, EEEEEII, EEEIEE, EEIEEE, EEIEEI), become long-term memory. There is no special order for motifs in the figure.

Motif Name	Synaptic Input Type				ap	Motif Name	Synaptic Input Type					ap	Motif Name	Synaptic Input Type						ap	Motif Name	Synaptic Input Type						ap							
	1	2	3	4			1	2	3	4	5			1	2	3	4	5	6			1	2	3	4	5	6								
MTF8	I	E	E	E	10	MTF19	E	E	I		9	MTF28	I	I	E	E	I	10	MTF29	I	E	E	E	E	13	MTF13	E	E	I	E	I	E	8		
	I	I	E	E	9		MTF20	E	E	I			9	I	I	E	I	I		8	I	E	E	E	I			10	E	E	I	E	I	I	8
	I	I	E	I	9		MTF22	I	E	E			8	E	I	E	I	I		8	E	I	E	I	I			8	E	E	I	I	I	E	9
MTF38	E	I	I	E	9	MTF36	I	E	I	E	8	MTF34	E	E	I	E		8		I	E	E	E	E		12	E	E	I	I	I	I	8		
MTF5	E	E	E		11	MTF25	E	I	I		8	MTF35	E	E	E	I		10		I	E	E	E	I		9	E	I	E	E	E	I	11		
MTF6	I	E	I		10	MTF15	E	E	E	I	9	MTF33	E	I	I	I	I	8		I	I	E	E	I		8	E	I	E	E	I	E	9		
MTF7	I	E	E		8		I	E	E	I	8	MTF17	I	E	E	E	E	8	MTF31	E	E	E	I	E	8	E	I	I	E	I	E	9			
	I	E	I		8	E	E	I	E	8	E		E	E	E	I	13	E		I	E	E	I		8	E	I	E	E	I	I	8			
MTF9	I	E	I	I	8	MTF11	E	E	E	I	12		E	E	E	I	E	12		E	I	E	I	I		9	E	I	I	I	I	E	8		
MTF30	E	I	E	I	9		I	E	E	E	8		E	E	E	I	I	11		I	E	E	E	I		8									
	I	E	E	I	9		I	E	I	E	8		I	E	E	I	E	9		I	E	E	I	E		8									
MTF4	E	E	E		9		I	E	I	I	9		I	E	E	I	I	8		I	I	E	I	E		8									
	E	E	I		8	MTF12	E	I	E	I	I	8		I	E	I	I	E	9		I	I	E	I	I		8								

Figure 10: Of the motifs in Fig. 5., those showing short-term memory behaviour; (numbers above motifs indicate synaptic input, numbers in the figure indicate synaptic input type) representation of neurons with probabilities of synaptic input types and the number of Action Potentials (AP) produced in neuron C.

Table 1: Chemical synaptic conductivity model, effect of time constant variation on short-term memory time.

Synaptic conductivity time constant $\tau(ms)$	Short-term memory duration (ms)	Number of action potentials
5	-	-
10	-	-
20	30	3
25	35	5
30	60	6
35	88	8
40	110	9
50	127	11

3.2 Identification of Triple Neuron Network Motifs, which are Short-Term Memory

All the motifs in Fig. 5. were analysed in terms of short-term memory behaviour by the methods described above. In some motifs; we observed that depending on the synaptic type, the action potentials formed in the output neuron C continued for a while, although the external current stimulus to the input neuron (A) was ended. This situation evaluates motifs as short-term memory behaviour. It refers to the retention of information for a while after the warning. Fig. 10. shows motifs that create short-term memory. Additionally, it shows the number of action potentials generated in neuron C to express the excitation situations of the neuron s and the retention time of the information. This study revealed the effect of connection and stimulus type on short-term memory formation in all three-neuron motifs.

3.3 The Effect of the Change in the Time Constant Parameter of the Conductivity Function of the Chemical Synaptic Communication Model between Neurons on Short-Term Memory Behaviour

The duration and number of action potentials formed in the C neuron were examined for different time constant values from the studies performed by changing the time constant of the chemical synaptic conductivity function. For this, the case study was carried out on the MTF8 motif model in Fig. 5. For the different values of the synaptic conductivity time constant (τ) seen in Table 1, the external current input in Fig. 6. (a) was applied to the neuron (A). The short-term memory time, as measured by the action potentials that continue to be produced in the C neuron after the external current input is interrupted, is shown in Table 1. From these data; it is seen that with increasing values of synaptic conductivity time constant, the duration and number of action potentials that occur at the output of the motif increase after external current input. This change prolongs the short-term memory time.

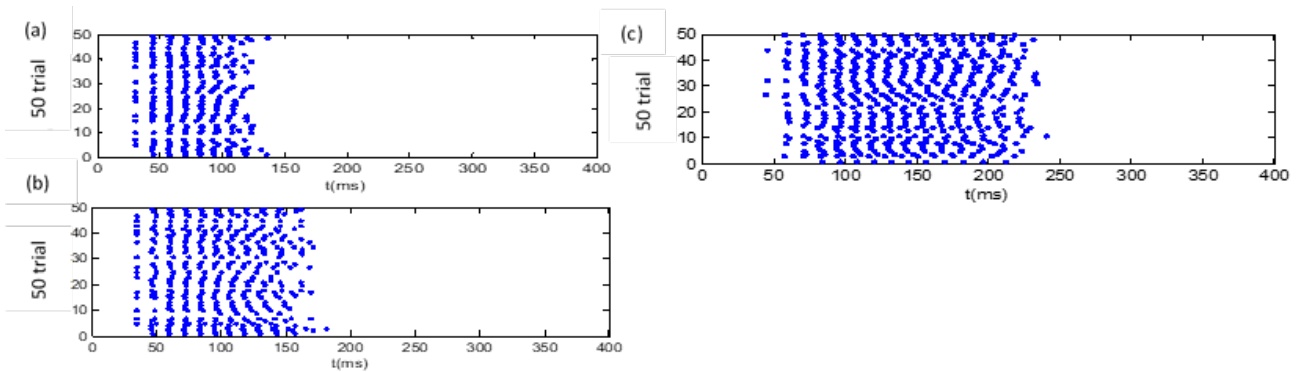


Figure 11: Raster plots of action potentials formed in the C neuron for (a) ($\tau = 25ms$) (b) ($\tau = 35ms$) (c) ($\tau = 50ms$) as a result of experiments repeated 50 times for each of the synaptic conductivity time constant (τ) values in the MTF8 motif.

In this section, the variation of short-term memory duration with time constant is graphically shown. From the studies done in MTF8; the short-term memory times of neurons at different values of the synaptic communication time constant (stimulus types IEEE) are shown in Fig. 11. This situation can also be evaluated as an increase in synapse strength during learning. It can be seen from the figures that as the time constant increases, the information retention time also increases.

4 Discussion

This study is about how learning occurs in brain neuronal networks, which are made up of complex connections. For this purpose, we generated all tri-neuronal network motifs using graph topology. All created motifs were eliminated considering their ability to form interneuron connections. In our study, we focused on the effect of the structure of motifs, the type of synaptic input of neurons, and the time constant of synaptic conductivity on short- and long-term memory behaviour. From the studies on motifs, all motifs showing long- and short-term memory behaviour were determined by considering the types of interneuron synaptic input. In addition, the effect of synaptic conductivity time constant in the chemical synapse model between neurons on short-term memory time was investigated. In the literature; there are studies on several motifs, of which the triple neuron connection is specific. In our study, we methodically obtained all of the three-neural interconnection possibilities in neural networks using graph topology. Some of the motifs obtained; it was removed from the work list because it did not contain three neurons and did not create an input and output neuron state due to the synaptic input direction. Thus, we constructed all the motif possibilities suitable for the neuronal network structure. In Fig. 5., 38 motif models suitable for these features are shown. Triple neural network motif structures were determined, suitable for the studies to be carried out in neural networks. We examined the short- and long-term memory status of the motifs obtained. In triple neural network motifs, one neuron input, one neuron output, and one neuron drive are considered. In the experiments, an external current is applied to the input neuron and the behaviour of the output neuron is examined. If the output neuron continues to generate signals even though the external current input is interrupted, the motif is considered to be long-term memory. If the output neuron generates a signal for some time after the external current input is interrupted, the motif is considered short-term memory. To conduct these experiments, we created separate models for each motif in Fig. 5. with Matlab software. The neurons that make up the motif, according to the interneuron connection structure; the software was modelled as a neuron with only external current input, only one synaptic input, both external current input and one synaptic input, two synaptic inputs, or no input applied. We used the Hodgkin-Huxley model for neurons. The synaptic input type probabilities (E,I) of the neurons were tested for each motif and the action potential generation status of the output neuron (C) was observed in each case. In the results obtained, the states of producing a continuous action potential were obtained and the states of being long-term memory were determined. All cases are shown in Fig. 9. Likewise, after the input current is cut off, short-term memory states that produce action potentials in the output neuron for a while were determined. All cases are shown in Fig. 10. During learning, changes occur in synaptic inputs between neurons. In addition, physical changes occur in the dendritic spines, which are in the connection from the axon tip to the dendrites, in the postsynaptic neuron section. These changes are thought to be significantly related to memory. These spines undergo changes in the form of growth during the learning process. We modelled this growth state by changing the time constant within the synaptic conductivity model. Thus, the memory time of the motif, which has short-term memory characteristics, is extended depending on the time constant. We studied this study on a motif, which is short-term memory, at different values of the time constant. The obtained results are shown in Table 1 and Fig. 11. During learning; the effects of connections between neurons, direction and type of synaptic input (E,I) on memory formation were examined. In the studies conducted in this area, a limited number of motifs have been studied. In most of the studies, neuron models with fewer parameters were preferred. In our study, the Hodgkin-Huxley neuron model, which successfully represents neurons with more parameters, was preferred and all tripartite neuronal network motifs were studied. In some studies, noise signals are generally used instead of synaptic inputs.

In our study, if the cell membrane voltage exceeds a certain threshold value as a result of interneuron communication, synaptic input to the neuron, an action potential is modelled. This is more realistic. Likewise, the effect of neurotransmitters emitted in the space between neurons making chemical synapses on the postsynaptic neuron was modelled as excitatory or inhibitory. For this, two different level voltage values of the equilibrium voltage E_{syn} , which constitutes of the synaptic input current, were used ($E \rightarrow E_{syn} = 10V$, $I \rightarrow E_{syn} = -70V$). All motifs and necessary conditions showing long-term memory behaviour are shown in Fig. 9. All the motives and necessary conditions showing short-term memory behaviour are also presented in Fig. 10. Especially the significant effect on short-term memory behaviour; it has been shown that besides the type of connection, the synaptic input types of neurons have suitable possibilities. In the studies, short-term memory duration was studied in quad neuron network motifs. In our study, this time change was modelled with the synaptic input time constant. This situation was evaluated as a prolongation of the learning process. The effect, which also expresses the physical change in the postsynaptic region, extended the information retention time. We demonstrated this for various values on a motif. In the neuron model we used, the deterministic model was preferred for the ion channels of neurons. The cell membrane is considered homogeneous. However, evaluating the randomness of the ion channels and considering the heterogeneous structure of the cell membrane will create a more realistic model. While the action potential is forming in the neuron, the arrival of new synaptic inputs can be prevented (the refractory period). In the three-neuronal motif structure we created; larger network connections can be created by multiplexing the input, output, driver neurons. Neural coding can be studied on these models.

Authors' Contributions

AT applied the cell software with the determined model, developed the software for the model and network motif structure. He performed all the experiments and analyzed the motifs. TK conducted pattern identification studies on cell modeling and determined motif analysis methods. All authors read and approved the last article.

Competing Interests

We declare that there is no conflict of interest between the authors and with any institution in the study.

Ethical Approval

When our study is a simulation study, it does not require ethical approval since both human and/or animal studies are not done.

References

- [1] R. Milo, S. Shen-Orr, S. Itzkovitz, N. Kashtan, D. Chklovskii, and U. Alon, "Network motifs: Simple building blocks of complex networks," *Science*, vol. 298, no. 5594, pp. 824–827, 2002.
- [2] S. Song, P. J. Sjöström, M. Reigl, S. Nelson, and D. B. Chklovskii, "Correction: Highly nonrandom features of synaptic connectivity in local cortical circuits," *PLOS Biology*, vol. 3, no. 10, 2005.
- [3] H. Kugler, S.-J. Dunn, and B. Yordanov, "Formal analysis of network motifs," *bioRxiv*.
- [4] O. Sporns and R. Kötter, "Motifs in brain networks," *PLOS Biology*, vol. 2, 2004.
- [5] R. J. Prill, P. A. Iglesias, and A. Levchenko, "Dynamic properties of network motifs contribute to biological network organization," *PLOS Biology*, vol. 3, no. 11, 2005.
- [6] S. Song, P. J. Sjöström, M. Reigl, S. Nelson, and D. B. Chklovskii, "Highly nonrandom features of synaptic connectivity in local cortical circuits," *PLOS Biology*, vol. 3, no. 3, 2005.
- [7] C. Li, "Functions of neuronal network motifs," *Phys. Rev. E*, vol. 78, no. 3, p. 037101, 2008.
- [8] C. Bargmann and E. Marder, "From the connectome to brain function," *Nature methods*, vol. 10, pp. 483–90, 2013.
- [9] M. D. Humphries, "Dynamical networks: Finding, measuring, and tracking neural population activity using network science," *Network Neuroscience*, vol. 1, no. 4, pp. 324–338, 2017.
- [10] S. Fornari, A. Schäfer, M. Jucker, A. Goriely, and E. Kuhl, "Prion-like spreading of alzheimer's disease within the brain's connectome," *Journal of The Royal Society Interface*, vol. 16, p. 20190356, 2019.
- [11] M. De Roo, P. Klauser, P. Méndez, L. Poglia, and D. Muller, "Chapter 11 spine dynamics and synapse remodeling during ltp and memory processes," *Progress in brain research*, vol. 169, pp. 199–207, 2008.
- [12] E. Bruel-Jungerman, S. Davis, and S. Laroche, "Brain plasticity mechanisms and memory: A party of four," *The Neuroscientist : a review journal bringing neurobiology, neurology and psychiatry*, vol. 13, pp. 492–505, 2007.
- [13] D. Chao-Yi, J. Lim, Y. Nam, and C. Kwang-Hyun, "Systematic analysis of synchronized oscillatory neuronal networks reveals an enrichment for coupled direct and indirect feedback motifs," *Bioinformatics*, vol. 25, no. 13, pp. 1680–1685, 2009.
- [14] B. Albeni, *ISynaptic Plasticity: New Research*, 2009.
- [15] M. Mayford, S. Siegelbaum, and E. Kandel, "Synapses and memory storage," *Cold Spring Harbor perspectives in biology*, vol. 4, no. 13, 2012.
- [16] N. Chenkov, H. Sprekeler, and R. Kempter, "Memory replay in balanced recurrent networks," *PLOS Computational Biology*, vol. 13, no. 1, pp. 1–36, 2017.
- [17] M. T. Owens and K. D. Tanner, "Teaching as brain changing: Exploring connections between neuroscience and innovative teaching," *CBE—Life Sciences Education*, vol. 16, no. 2, p. fe2, 2017.
- [18] J. Hennig, E. Oby, D. Losey, A. Batista, B. Yu, and S. Chase, "How learning unfolds in the brain: toward an optimization view," *Neuron*, vol. 109, 2021.
- [19] O. Atay, A. Doncic, and J. M. Skotheim, "Switch-like transitions insulate network motifs to modularize biological networks," *Cell systems*, vol. 32, pp. 121–132, 2016.
- [20] J.-R. Kim, Y. Yoon, and K.-H. Cho, "Coupled feedback loops form dynamic motifs of cellular networks," *Biophysical journal*, vol. 94, pp. 359–65, 2008.
- [21] H. Koepl and S. Haeusler, "Motifs, algebraic connectivity and computational performance of two data-based cortical circuit templates," in *Proceedings of the sixth International Workshop on Computational Systems Biology*, 2009, p. 4.
- [22] L. Peris, M. Bisbal, J. Martínez-Hernández, Y. Saoudi, J. Jonckheere, M. Rolland, M. Sebastien, J. Brocard, E. Denarier, C. Bosc, C. Guerin, S. Gory-Fauré, J. C. Deloulme, F. Lanté, I. Arnal, A. Buisson, Y. Goldberg, L. Blanchoin, C. Delphin, and A. Andrieux, "A key function for microtubule-associated-protein 6 in activity-dependent stabilisation of actin filaments in dendritic spines," *Nature Communications*.

- [23] D. Braha, "Patterns of ties in problem-solving networks and their dynamic properties," *Scientific Reports*, vol. 10, p. 18137, 2020.
- [24] S. Patra and A. Mohapatra, "Application of dynamic expansion tree for finding large network motifs in biological networks," *PeerJ*, vol. 7, p. e6917, 2019.
- [25] E. Martorana, G. Micale, A. Ferro, and A. Pulvirenti, "Establish the expected number of induced motifs on unlabeled graphs through analytical models," *Applied Network Science*, vol. 5, p. 58, 2020.
- [26] M. Arbib, *The Handbook of Brain Theory and Neural Network*, 2003.
- [27] D. Bassett and E. Bullmor, "Small-world brain networks," *The Neuroscientist : a review journal bringing neurobiolog, neurology and psychiatry*, vol. 12, pp. 512–23, 2007.
- [28] B. Danielle and B. Edward, "Small-world brain networks revisited," *The Neuroscientist*, vol. 23, 2016.
- [29] H. Schwöbbermeyer, *Network Motifs*. John Wiley and Sons, Ltd, 2008.
- [30] N. Borovok, E. Neshet, Y. Levin, M. Reichenstein, A. Pinhasov, and I. Michalevski, "Dynamics of hippocampal protein expression during long-term spatial memory formation," *Molecular and Cellular Proteomics*, vol. 15, p. mcp.M115.051318, 2015.
- [31] A. Spiegler, E. C. A. Hansen, C. Bernard, A. R. McIntosh, and V. K. Jirsa, "Selective activation of resting-state networks following focal stimulation in a connectome-based network model of the human brain," *eNeuro*.
- [32] A. Mirisis, A. Alexandrescu, T. Carew, and A. Kopeck, "The contribution of spatial and temporal molecular networks in the induction of long-term memory and its underlying synaptic plasticity," *AIMS Neuroscience*, vol. 3, pp. 356–384, 2016.
- [33] R. Staudemeyer and E. Morris, "Understanding lstm – a tutorial into long short-term memory recurrent neural networks," 2019.
- [34] J. Keener and J. Sneyd, *Cellular Homeostasis*. Springer New York, 2009, pp. 49–119.
- [35] B. F. Grewe, J. Gründemann, L. J. Kitch, J. A. Lecoq, J. G. Parker, J. D. Marshall, M. C. Larkin, P. E. Jercog, F. Grenier, J. Z. Li, A. Lüthi, and M. J. Schnitzer, "Neural ensemble dynamics underlying a long-term associative memory," *Nature*, vol. 543, pp. 670 – 675, 2017.
- [36] N. S.R., I. Boybat, M. Gallo, E. Eleftheriou, A. Sebastian, and B. Rajendran, "Experimental demonstration of supervised learning in spiking neural networks with phase-change memory synapses," *Scientific Reports*, vol. 10, 2020.
- [37] Z. Harper and C. Welzig, "Exploring spatiotemporal functional connectivity dynamics of the human brain using convolutional and recursive neural networks," 2019, pp. 1–6.
- [38] T. Gorochowski, C. Grierson, and M. Di Bernardo, "Organization of feed-forward loop motifs reveals architectural principles in natural and engineered networks," *Science Advances*, vol. 4, p. eaap9751, 2018.
- [39] D. Schachinger, "Simulation of extracellularly recorded activities from small nerve formations in the brain," 2003.
- [40] P. Dayan and L. F. Abbott, *Theoretical neuroscience: computational and mathematical modeling of neural systems*. MIT press, 2005.
- [41] E. M. Izhikevich, *Dynamical Systems in Neuroscience: The Geometry of Excitability and Bursting*. The MIT Press, 2006.
- [42] Z. Tian and D. Zhou, "Library-based fast algorithm for simulating the hodgkin-huxley neuronal networks," 2021.
- [43] T. Zhongqi and Z. Douglas, "Design fast algorithms for hodgkin-huxley neuronal networks," 2021.
- [44] S. Navlakha, Z. Bar-Joseph, and A. Barth, "Network design and the brain," *Trends in Cognitive Sciences*, vol. 22, 2017.
- [45] J. M. Bower, D. Beeman, J. M. Bower, and D. Beeman, "Compartmental modeling," *The Book of GENESIS: Exploring Realistic Neural Models with the General NEural Simulation System*, pp. 7–15, 1998.
- [46] W. Gerstner and W. M. Kistler, 2002.
- [47] J. Wang, J. Geng, and X. Fei, "Two-parameters hopf bifurcation in the hodgkin–huxley model," *Chaos, Solitons and Fractals*, vol. 23, no. 3, pp. 973–980, 2005.
- [48] L. Meng and J. Xiang, "Brain network analysis and classification based on convolutional neural network," *Frontiers in Computational Neuroscience*, vol. 12, 2018.
- [49] L. J. Boaz, R. R. A., K. Xiangnan, K. Sungchul, K. Eunye, and R. Anup, "Graph convolutional networks with motif-based attention," in *Proceedings of the 28th ACM International Conference on Information and Knowledge Management*, New York, NY, USA, 2019, p. 499–508.
- [50] K. Patrick, P. Karin, S. Achim, and M. Claus, "Recurrence resonance in three-neuron motifs," *Frontiers in Computational Neuroscience*, vol. 13, p. 64, 2019.
- [51] P. Sabyasachi and M. Anjali, "Application of dynamic expansion tree for finding large network motifs in biological networks," *PeerJ*, vol. 7, p. e6917, 2019.
- [52] —, "Disjoint motif discovery in biological network using pattern join method," *IET Systems Biology*, vol. 13, no. 5, pp. 213–224, 2019.
- [53] H. Li, C. Liu, and J. Wang, "Memory and computing function of four-node neuronal network motifs," in *Proceeding of the 11th World Congress on Intelligent Control and Automation*, 2014, pp. 5818–5823.
- [54] L. Peris, M. Bisbal, and e. Martínez-Hernández, "A key function for microtubule-associated-protein 6 in activity-dependent stabilisation of actin filaments in dendritic spines," *Nature Communications*, vol. 9, 2018.



Research Article

Effect of Open Firing and Electric Furnace Firing on Material Characterization

Erdal Çetintaş^{1a}

¹ Ceramics Department, Faculty of Fine Arts, Akdeniz University, Antalya, Türkiye

ecetintas@akdeniz.edu.tr

DOI : 10.31202/ecjse.1460823

Received: 28.03.2024 Accepted: 19.10.2024

How to cite this article:

Erdal Çetintaş, " Effect of Open Firing and Electric Furnace Firing on Material Characterization", El-Cezeri Journal of Science and Engineering, Vol: 12, Iss: 1, (2025), pp.(66-73).

ORCID: "0000-0002-9814-7574.

Abstract : Ceramic production started with firing earthenware products using fire and has been developed with various techniques and discoveries until today. Although these developments continue, ceramic products produced using traditional methods still exist. Considering today's conditions, it is essential to experimentally examine different firing environments of ceramics, considering both the cost and the sustainability of the products. This study aimed to determine the changes caused by the differences between open firing and electric furnace (800 °C) firing environment in the local pottery production center in Sorkun village of Mihalıççık district of Eskişehir province. For this purpose, water absorption, firing shrinkage, bulk shrinkage, color measurement, chemical analysis (XRF), mineralogical analysis (XRD), differential thermal analysis (DTA) and scanning electron microscopy (SEM) analysis of the samples were performed after two firing process. Based on the obtained results, the values of dry, firing, and bulk shrinkage after open firing suggest that the separation of structural water and/or the complete occurrence of crystal changes in the ceramic sample are not fully achieved compared to electric furnaces. It was determined that whiteness (L^*) and redness (a^*) increased after the electric furnace firing. XRD analysis of results indicated that clinocllore, amphibole, quartz, fluoro-ederite minerals were determined in open firing samples, anorthite, calcium aluminum silicate, magnesiohornblende, quartz minerals were determined in electric furnace firing. The presence of clay minerals in the open firing sample confirms that 800 °C was not fully reached.

Keywords : Ceramic, color, electric furnace, open firing, Sorkun, XRD

1 Introduction

Ceramic production, which started with firing earthenware products using fire, has been developed with various technical solutions and discoveries until today. However, in many ceramic production (pottery) centers located in different geographies, the equipment and tools developed ages ago are used without much change, and this type of production is called "Primitive Pottery" today [1]. Since the beginning of prehistoric research, ceramic production has been one of the most critical indicators in determining social, economic and social differentiation, not only because of technological developments but also because of the form changes they show depending on their functionality [2]. Ceramics are used not only as daily-use items but also as bricks and tiles used in construction, oil lamps, jewelry and ornaments, sarcophagi, and children's toys [3].

The ceramic production cycle consists of raw materials, mud processing, shaping, drying, and firing techniques [4]. Although the clay structure used in ceramic production, shaping techniques and firing methods have changed depending on technological advances, it is known that traditional methods are still maintained. In ancient times, the centers of the ceramic industry were located near clay-rich regions, and the bodies of ceramic pieces were generally prepared from raw materials rich in clay, kaolin, quartz, feldspar, or micaceous formations [5]. In some regions, clay deposits used in antiquity are still used today according to the oldest traditions [6].

Firing is the most critical stage in ceramic production after raw materials', shaping, and drying. The prepared ceramic products' firing process is carried out to gain durability by chemical reactions thanks to heat energy after the drying process. When the studies on firing are examined, it is observed that firing started with open firing, single-chamber firing, firing chamber, and wood-fired kilns, and many alternative firing techniques and kiln (furnace) are used today depending on technological developments [7], [8].

Open firing is an outdoor firing method in which ceramic products are placed side by side and on top of each other, and the fuels (organic materials such as straw, stalks, wood, etc.) are placed in the gaps at the bottom top and between the ceramics and are fired [9]. Since it is open firing, paying attention to weather conditions is necessary. Exposure to wind and contact between ceramic forms and fuel make it difficult to control the atmosphere and the temperature in open firing [10]. Due to the uncontrolled temperature, firing, and color differences are possible [11]. Since the fire in this firing method is in direct contact with the ceramic body, fractures, and cracks can be high during firing. To partially reduce this damage, some regions have been protected the pottery underneath from sudden heat change by stacking previously broken pottery pieces on the upper side of the kiln [12]. In addition to traditional firing methods, electric furnace are widely used to fire ceramic products. Electric furnace are generally square or rectangular fixed kilns. Such furnaces are preferred to easily adjust the maximum temperature, heating rate, and thermal homogeneity.

Since open firing and electric furnace methods affect many properties of ceramic products, the thermal profile of firing including atmospheric conditions (oxydant and reducing atmosphere) can also be considered as a primary factor of ceramic properties. The parameters that characterize the firing thermal profile are maximum temperature, heating rate, heating time, thermal homogeneity, and continuity [13]. The studies have reported that the differences between the thermal profiles of open firings and electrical furnaces are of opposite nature for ceramic production. In kiln firing, the high maximum temperature, low heating rate, and the ability to soaking/firing time are controlled isothermally are controlled, while these properties in open firing are completely variable and uncontrollable [14]–[16]. The thermal profile of open firing cannot be kept constant due to atmospheric conditions. Depending on all these parameters, knowing the reactions that occur during the firing process in ceramic bodies can help determine the firing temperatures.

Considering the previous literature, although firing temperature prediction studies based on phase characterization have been investigated in many studies separately, studies in which the differences in firing environments which are examined together with the structural and phase characterization of the same type of raw materials are a few. This study made inferences about the physical and structural differences that occur after the open firing, which is still traditionally practiced in Sorkun Village and the firing of the same raw material in an electric furnace. In addition, the color change, mineralogical properties, and structural findings obtained after different firing processes were interpreted and discussed.

2 Experimental Methods

This study examined potter's clay and firing in Sorkun Village, one of the important centers of pottery production. Sorkun Village is located 12 km away from the Mihaliççik district of Eskişehir and has a high altitude. The most important source of livelihood of the village is pottery. Two clay mixtures, "red" and "oily soil," are used in pottery making (Figure 1). Ceramic pots in different forms are prepared using mud prepared from these clays and left to dry.



Figure 1: Clay and mud preparation a) red clay, b) oily clay, c) mud mixing device, d) prepared mud.

The open firing process is carried out in an open field outside the village of Sorkun when the wind blows strong from one direction, and ceramic products are fired in one batch (300 to 500 pieces). First, on the straw and sawdust dust laid on the ground in the open field, the ceramic products are lined up with their mouths directed to the ground. A row of firewood and pots are laid and the firewood is lined up in the direction of the wind and burned. It is stated in the literature that the temperature value reaches approximately 750-800 ° during firing [17]. At the end of the firing process, the pots are pulled with a "çeykel" and left to cool (Figure 2).



Figure 2: Open firing process in Sorkun [17].

Since this study aims to determine the differences between open firing and electric kiln firing, a sample of the product obtained from open firing in Sorkun village was taken. The clay obtained from Sorkun village was shaped 30x5x1 cm for the electric furnace. After drying, 800 °C firing was carried out in the electric furnace (Figure 3).

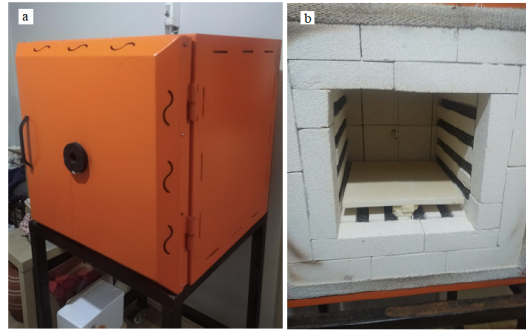


Figure 3: Electric furnace a) View of the furnace b) Inside furnace.

Physical tests such as water absorption, firing shrinkage, bulk shrinkage, and color measurements were performed to examine the changes in ceramic forms in different firing environments. The water absorption, firing shrinkage, bulk shrinkage tests in Table 1 were carried out according to the test methods explained in the section of "Experiments Applied to Clay and Kaolin" in "Ceramic Technology" book written by Arcasoy [18]. Color measurements were performed using a Konica Minolta color meter based on the CIELAB system. L , a , and b color measurements were recorded after open and electric firing. Elemental determination XRF examinations of the ceramic samples used in the study for the characterization tests were carried out on a Rigaku brand device. Semi-quantitative chemical analysis results of the prepared samples regarding weight percent were obtained. Samples taken from different firing environments were ground to a grain size of 100 μm , and XRD analysis was performed with a the Shimadzu brand XRD-6000 model device. The samples were scanned at 2 °/min and analyzed in the range of 2°-70° (2 θ) goniometer diffraction angle and 2000 cps (intensity) peak intensity. Additionally, thermal analysis (DTA/TG) of the raw clay sample was analyzed by SETARAM / labSys Evo device. Scanning electron microscope (SEM) examinations, which are necessary to examine the surface morphology of the ceramic samples and to perform microchemical analysis of the minerals, were carried out on the LEO brand, model 1431-VP SEM at AKU Technology Application Research Center (TUAM).

3 Results and Discussion

The changes occurring in different firing environments after open firing, which has traditionally existed in Eskişehir Province Sorkun Village, and electric furnace applied in today's conditions were examined. The findings and discussions are given in this section.

The water absorption, dry shrinkage, firing shrinkage, and bulk shrinkage of the samples used in this study are presented in Table 1. It was found that the water absorption value for the open firing sample is 15.28%, whereas it is 14.30% for the electric kiln sample. The amount of water absorption is directly proportional to the amount of pores present in the body. According to

these results, the water absorption rate is high in the open firing sample due to the number of pores present in the body. When the values obtained from dry shrinkage, firing shrinkage and bulk shrinkage tests are examined, the values are 5.44%, 0.47% and 5.89% in the open firing sample, while these values are 6.22%, 3.02%, and 9.27% respectively in the electric kiln sample. Based on the obtained results, the values of dry, firing, and bulk shrinkage after open firing suggest that the separation of structural water and/or the complete occurrence of crystal changes in the ceramic sample are not fully achieved compared to other firing conditions.

Table 1: Water Absorption, Dry Shrinkage, Firing Shrinkage, and Bulk Shrinkage values.

Firing Types	Water Absorption (%)	Dry Shrinkage (%)	Firing Shrinkage (%)	Bulk Shrinkage (%)
Open Firing	15.28	5.44	0.47	5.89
Electric Furnace	14.30	6.22	3.02	9.27

The color parameters of the ceramic samples after open firing and electric kiln firing are given in Table 2. Among the parameters used in color measurement, the L^* value is in the range of black-white (0-100), the a^* value shows red-green, and the b^* value shows a yellow-blue scale.

Table 2: Color parameter values obtained from ceramic samples.

Color Parameters	Open Firing	Electric Furnace
L	51.54	53.80
a	9.63	15.13
b	18.06	23.26

L parameter of the color properties expresses lightness. While the L value was 51.54 after open firing, the L value was measured as 53.8 after electric furnace firing. Accordingly, it was determined that the L value increased in the electric furnace firing. The change in the a parameter indicates redness when $a > 0$ and greenness when $a < 0$. When Figure 4 is examined, it is seen that the value of open firing has a value of 9.63 and the value of electric furnace firing has a value of 15.13. According to this, it was determined that the color changed towards redness in electric firing. The b parameter of the color properties expresses yellowness and blueness ($b > 0$ yellow and $b < 0$ blue). When the b parameter is examined, it is seen that it has a value of $b > 0$ after both firing. Accordingly, the change with the highest b value was obtained after electric furnace firing.

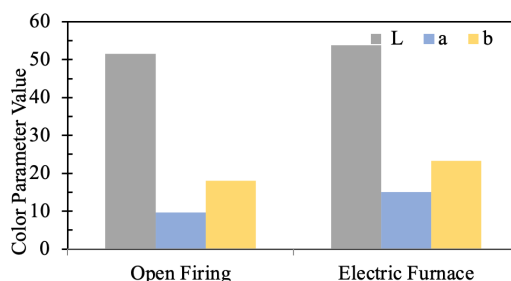


Figure 4: Color change in different firing environments.

In general, it is known that the color of ceramic products is mainly due to the minerals (especially iron oxide) and their amounts in the clay that make up the material and that the firing environment conditions are also adequate [19]–[21]. The terms oxidation and reduction refer to how much oxygen is in the kiln's atmosphere while the kiln is firing. An oxidation atmosphere has plenty of oxygen for the fuel to burn. A reduction atmosphere occurs when the amount of available oxygen is reduced. This may not sound like things that will affect your pottery, but it can. The reduction process, when oxygen is leached out of your kiln atmosphere and pottery, can change the texture or color of clay. In the study, although the ceramic clay was the same in both firings, an increase in color parameters was observed after electric kiln firing. It is thought that this difference in color arises due to the inability to achieve a uniform temperature during the firing process. When clays are fired at high temperatures, the color increases towards dark red. In other words, it shows that the temperature is high in electric kiln firing, but the open firing temperature cannot reach the electric firing temperature.

The chemical analysis results of the ceramic samples after firing are presented in Table 3. Upon examining the obtained chemical results, it was found that SiO₂ is the highest chemical component by weight in the samples. The SiO₂ content of the open hearth firing sample is 46.33%, whereas it is 48.56% in the electric kiln firing sample. Considering the MgO and CaO ratios, which indicate the presence of dolomite and calcite, which are known as carbonates in ceramic samples, it was determined that the MgO ratio was approximately 16.30% in both firing samples. In comparison, the CaO ratio was 9.05% in the open firing and 6.07% in the electric furnace firing. One of the clays that make up the Sorkun mud was named red. It indicates the presence of hematite minerals (Fe₂O₃) in this clay. The Fe₂O₃ ratios after firing are very close to each other and vary between 11.56% and 11.63%.

Table 3: XRF results of ceramic samples.

Chemical Composition (% by weight)	Firing Types	
	Open Firing	Electric Furnace
SiO ₂	46.33	48.56
Al ₂ O ₃	13.30	13.82
Fe ₂ O ₃	11.56	11.63
MgO	16.30	16.32
CaO	9.05	6.07
K ₂ O	1.08	0.99
Na ₂ O	0.64	0.66
TiO ₂	1.03	1.13
Cr ₂ O ₃	0.19	0.19
MnO	0.22	0.24
P ₂ O ₅	0.17	0.26
NiO	0.13	0.13

According to XRD results, clinochlore, amphibole, quartz, fluoro-ederite minerals were detected in the ceramic sample in open firing; anorthite, magnesiohornblende and quartz minerals were detected in the sample during electric furnace firing. Clinochlore is generally a product of hydrothermal alteration of amphibole, pyroxene and biotite and is associated with serpentine, calcite, dolomite etc. As a result of open firing XRD analysis, the presence of clay minerals (clinochlore, amphibole) is seen in the structure and shows that very high temperatures for sintering could not be reached.

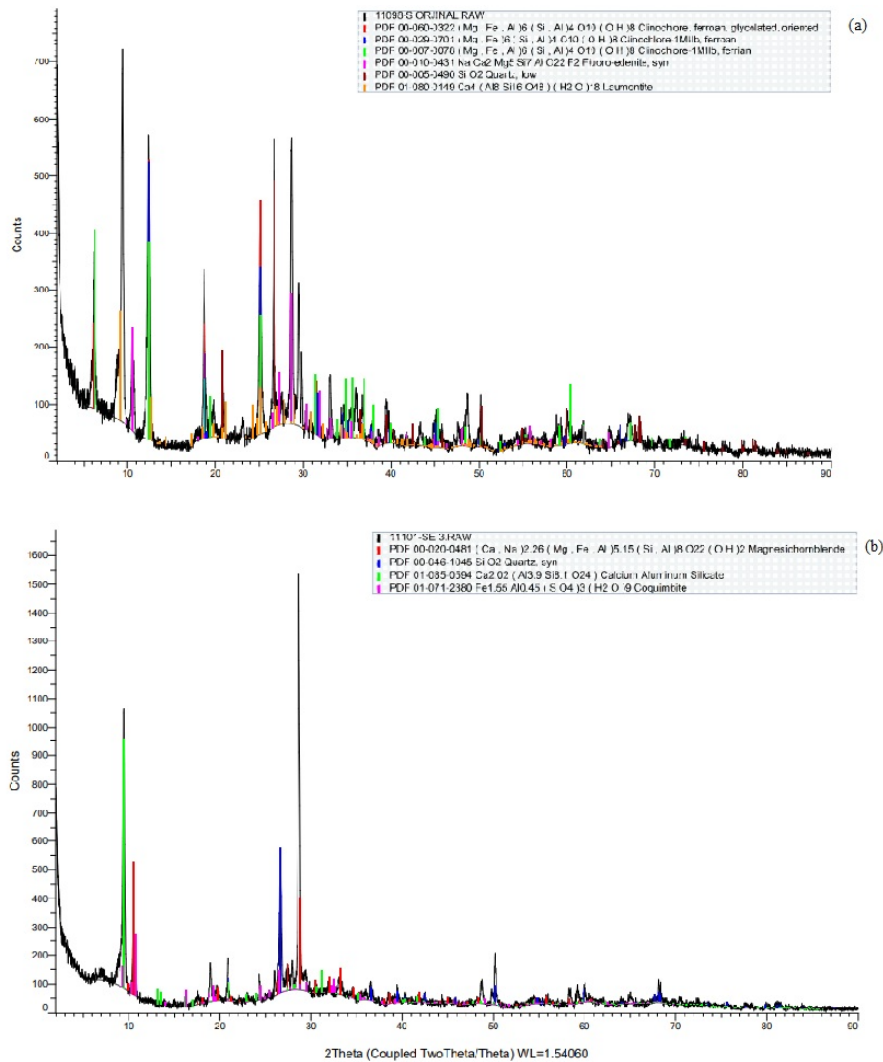


Figure 5: XRD patterns of ceramic a) Open firing (I: illite, In:Indialite, M: Montmorillonite, A: Albite, Q: Quartz,H: Hematite), b) Electric furnace firing (I: illite, In:Indialite, A:Albite, Q: Quartz).

To interpret the structural changes in the sample due to temperature variations, the DTA-TG results of the raw clay sample are presented in Figure 6. The characteristic endothermic and exothermic reactions identified from the TG, DTG (the derivative of the weight loss curve), and DTA curves are indicated on the graphs. The sample exhibits a total weight loss of approximately 10.00% within the temperature range of ~ 30 -900 $^{\circ}\text{C}$. In the temperature range of 30-200 $^{\circ}\text{C}$, the endothermic reaction observed at 110 $^{\circ}\text{C}$ on the DTA curve is attributed to the loss of physical water from the clay minerals. The exothermic reaction at 350 $^{\circ}\text{C}$ observed on the DTA curve within the temperature range of ~ 200 -400 $^{\circ}\text{C}$ is due to the combustion of likely organics present in the structure. The weight loss in the temperature range of 400-600 $^{\circ}\text{C}$ and the endothermic reaction at 500 $^{\circ}\text{C}$ observed on the DTA curve are associated with the loss of crystal water from the clay minerals. The endothermic reaction observed at ~ 650 $^{\circ}\text{C}$ on the DTA curve within the temperature range of ~ 600 -700 $^{\circ}\text{C}$ is thought to be due to the decomposition of the magnesite mineral. The endothermic reaction observed at ~ 740 $^{\circ}\text{C}$ on the DTA curve within the temperature range of ~ 700 -800 $^{\circ}\text{C}$ is attributed to the decomposition of the calcite mineral.

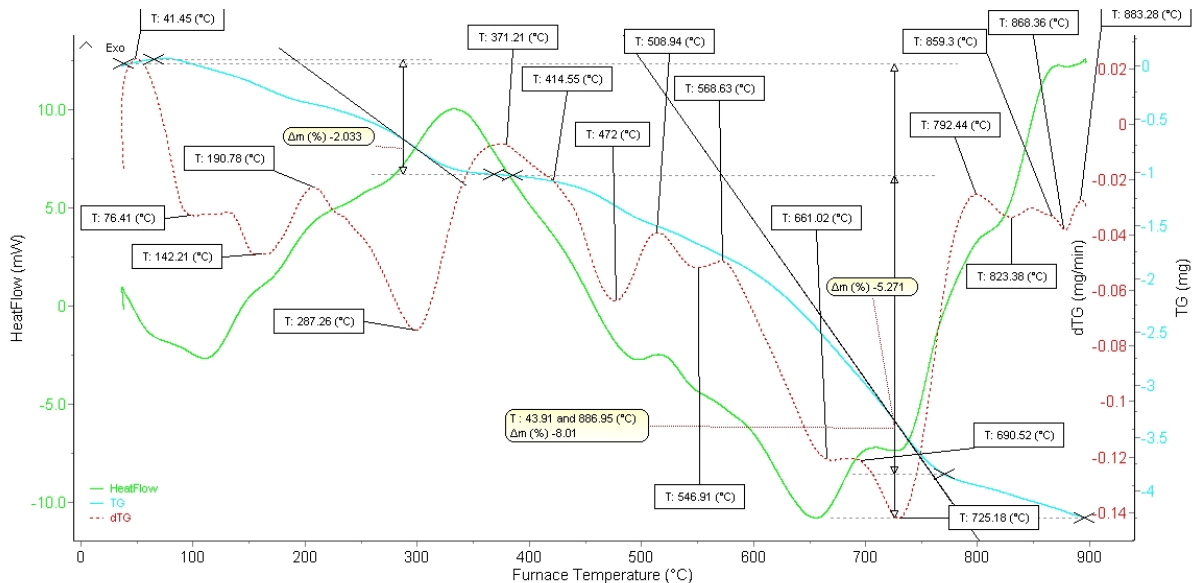


Figure 6: DTA-TG curves of raw clay sample.

Scanning electron microscopy (SEM) was used to examine the microstructure of ceramic samples fired in different firing atmospheres. When the structures of the open firing and electric firing samples are examined in Figure 6, rod-like structures, traces of mineral weathering, and small voids are observed. Since the firing temperature of the electric furnace was 800 $^{\circ}\text{C}$, similar structures are present on the surfaces of the open firing sample and the microstructural properties have not changed much. When the SEM images and EDX analyses are evaluated together with the XRD analysis results obtained, 19.31% O_3 in the mineral ratios in the rod-like structure in the open firing confirms that it is hematite (Figure 7).

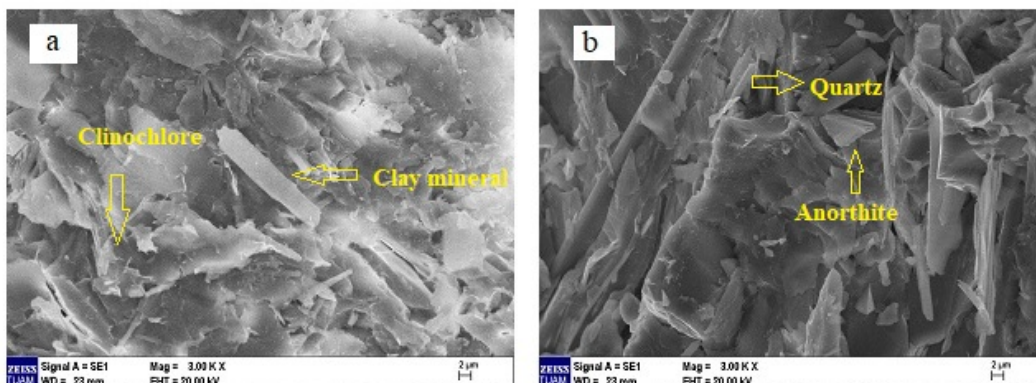


Figure 7: SEM micrographs of firing ceramic samples.

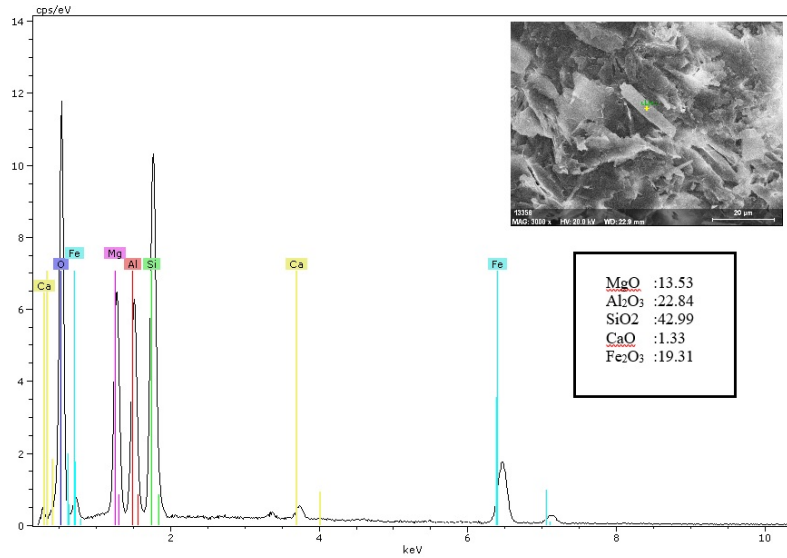


Figure 8: SEM image and EDX analyses of open firing.

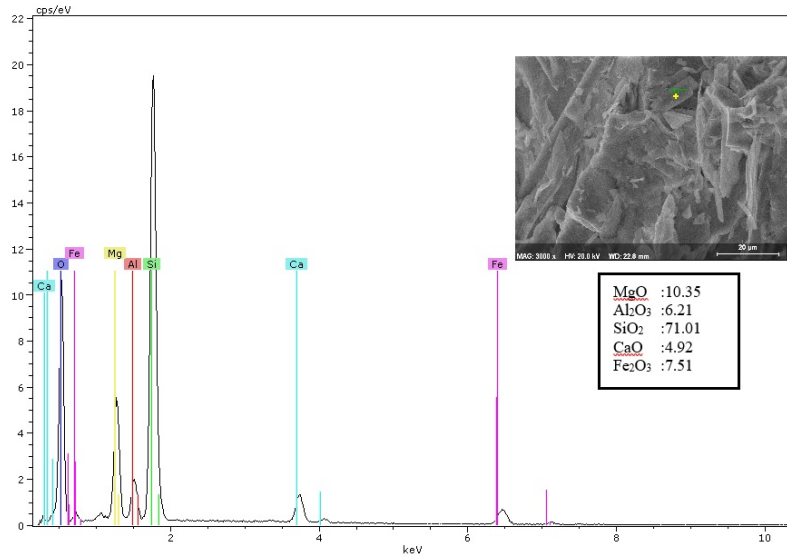


Figure 9: SEM image and EDX analyses of electric furnace firing.

4 Conclusions

Firing of ceramic products made from clay using conventional fire obtained from raw materials has evolved over time with various techniques and discoveries. However, different firing techniques and kilns are used in many ceramic production centers in different geographies today. In today's conditions, it is essential to improve the firing conditions considering both the cost and the sustainability of the products. In this study, the performances of open firing and electric furnace firing were investigated in a local ceramic production place, Sorkun village of Mihalıççık District of Eskişehir.

Accordingly, the water absorption value was found to be higher after open firing. Similarly, dry shrinkage, cooking shrinkage, and bulk shrinkage values were also determined to be higher than those of electric furnace firing. The results obtained show that the separation of crystal water and/or crystal change in the structure of the ceramic sample does not occur completely compared to other firing environments. As a result of the color measurement test, while the *L* value was 51.54 after open firing, the *L* value was 53.8 after electric furnace firing. Similarly, it was determined that the color parameters *a* and *b* increased in electric furnace firing. It was determined that the chemical analysis values obtained after the firing processes of the ceramic samples were very close to each other. The highest chemical composition by weight after different firing processes of the ceramic samples was found to be SiO₂. Both XRD and SEM-EDX analysis results confirmed this high value. According to the XRD results, clinocllore, amphibole, quartz, fluoro-ederite minerals in the ceramic sample under open firing; anorthite, magnesiohornblende and quartz

minerals were detected in the sample under electric furnace firing. As a result of open firing XRD analysis, the presence of clay minerals (clinochlore, amphibole) in the structure shows that very high temperatures are not reached for sintering.

In summary, this research will provide significant benefits in terms of issues such as energy consumption, production speed and sustainability in new studies by bringing together the advanced conditions of the local and industrial environment and determining the changes in different firing environments.

Acknowledgement

I would like to Dr. Hakan Şahin and Pervin Gençoğlu for providing invaluable guidance throughout XRD and DTA-TG analysis.

Authors' Contributions

EÇ designed the structure, carried out the experiments work, the theoretical calculations and wrote up the article.

Competing Interests

The author declares that no inferences have been made.

References

- [1] Ö. Dicle, "Günümüzde anadolu'da kadınlar tarafından yapılan çömlekçilik," Ph.D. dissertation, Dokuz Eylül Üniversitesi, Güzel Sanatlar Enstitüsü, İzmir, 2015.
- [2] Ö. A. Türedi, *Geleneksel Çömlek Sanatı*. Eskişehir: Anadolu Üniversitesi, 2001.
- [3] D. O. Erman, "Türk seramik sanatının gelişimi: Toprağın ateşle dansı," *Acta Turcica*, vol. 4, no. 1, pp. 18–33, 2012.
- [4] R. P. M., *Pottery Analysis: A Sourcebook*. Chicago: University of Chicago Press, 1987.
- [5] R. P.M., "Recent ceramic analysis: 2. composition, production, and theory," *Journal of Archaeological Research*, vol. 4, no. 3, pp. 165–202, 1996.
- [6] G. Montana, "Ceramic raw materials: how to recognize them and locate the supply basins—mineralogy, petrography," *Archaeological and Anthropological Sciences*, vol. 12, no. 8, p. 175, 2020.
- [7] H. Eleni, *Ceramic kilns in ancient greece: technology and organization of ceramic workshops*. University of Cincinnati, 2002.
- [8] S. Cemalettin, "Geleneksel çömlekçilikte değişim ve yüksek pişirim cazibesi," *Art-e Sanat Dergisi*, vol. 10, no. 19, pp. 242–251, 2017.
- [9] —, "İlkel fırınlar," Master's thesis, Anadolu University (Türkiye), 1990.
- [10] M. Marino, N. Ch, and R. Denis, "Temperature evolution inside a pot during experimental surface (bonfire) firing," *Applied Clay Science*, vol. 53, no. 3, pp. 500–508, 2011.
- [11] G. O. P., "Bonfire of the enquiries. pottery firing temperatures in archaeology: What for?" *Journal of Archaeological Science*, vol. 19, no. 3, pp. 243–259, 1992.
- [12] K. A. Cengiz, "İndirgen (redüksiyon) ortamda sırsız seramik pişirim teknikleri ve uygulama yöntemleri," *Ankara Üniversitesi Güzel Sanatlar Fakültesi Dergisi*, vol. 5, no. 1, pp. 360–378, 2023.
- [13] T. R., "Identification of pottery firing structures using the thermal characteristics of firing," *Archaeometry*, vol. 56, pp. 78–99, 2014.
- [14] D. E. Arnold, *Ceramic theory and cultural process*. Cambridge: Cambridge University Press, 1988.
- [15] O. C., T. P., and V. A. G., *Pottery in archaeology*. Cambridge: Cambridge University Press, 1993.
- [16] M. J. G., "Pyrotechnology," in *Handbook of Archaeological Sciences*, D. R. Brothwell and A. M. Pollard, Eds. Chichester: John Wiley & Sons, Ltd, 2001, pp. 493–506.
- [17] Eskişehir Valiliği İl Kültür ve Turizm Müdürlüğü, "Sorkun Çömlekçiliği," <https://eskisehir.ktb.gov.tr/Eklenti/35598,sorkunr2014.pdf>, (Accessed Jan. 10, 2024).
- [18] A. Ates, *Seramik Teknolojisi*. Marmara University., 1983.
- [19] J. Molera, P. T, and V.-S. M., "The colours of ca-rich ceramic pastes: origin and characterization," *Applied clay science*, vol. 13, no. 3, pp. 187–202, 1998.
- [20] R. C and P. Yiannis, "Effect of firing temperature and atmosphere on ceramics made of nw peloponnese clay sediments. part i: Reaction paths, crystalline phases, microstructure and colour," *Journal of the European Ceramic Society*, vol. 30, no. 9, pp. 1841–1851, 2010.
- [21] G. Elisabetta, "Ceramic technology. how to reconstruct the firing process," *Archaeological and Anthropological Sciences*, vol. 12, no. 11, p. 260, 2020.

Research Article

Classification of Dementia Levels by Using Different Convolutional Neural Network Architectures

Iclal Cetin Tas^{1a}, Murat Simsek^{2b}

¹ Electrical-Electronics Engineering Department, Ostim Technical University, Ankara, Türkiye

² Artificial Intelligence Engineering Department, Ostim Technical University, Ankara, Türkiye

icetintas@baskent.edu.tr

DOI : 10.31202/ecjse.1512362

Received: 08.07.2024 Accepted: 24.12.2024

How to cite this article:

Iclal Cetin Tas, "Classification of Dementia Levels by Using Different Convolutional Neural Network Architectures", El-Cezeri Journal of Science and Engineering, Vol: 12, Iss: 1, (2025), pp.(74-85).

ORCID: ^a0000-0002-1101-9773, ^b0000-0002-8648-3693.

Abstract : Dementia or Alzheimer is a disease that causes symptoms such as forgetfulness and loss of physical ability, which will add to the individual's life in later stages, along with morphological changes in the brain. Unfortunately, a definitive treatment for these diseases has not yet been found. However, it is aimed at slowing down the progression of the disease to ensure that the patient is less affected by these adverse conditions and to protect living standards with early diagnosis of the disease. In addition, a complete diagnosis of the disease requires a series of tests and a tiring diagnostic phase to be evaluated by an experienced specialist. High-resolution magnetic resonance imaging is used to make this determination. This study tries to determine the stage of the disease or whether the individual is healthy by using MR.MR images of individuals in 4 stages of the disease, one of which is a healthy individual, were described as a classification problem and tried to be solved using VGG, Resnet, and Mobilenet architectures. Over %95 success has been achieved by supporting the proposed architecture with feature analysis and classical architectures.

Keywords : Alzheimer, dementia levels, CNN, SMOTE, classification.

1 Introduction

Nowadays, many diseases seriously affect daily life and quality of life for a long time. Dementia types of especially Alzheimer's is one of the most important ones. Generally, there may be age-related memory problems called dementia. To summarize the relationship between dementia and Alzheimer's, dementia is a general term for a set of diseases characterized by cognitive decline, and then Alzheimer's disease is the most common type of dementia under this generalization. According to the World Health Organization, %60- %80 of dementia cases result in Alzheimer's. Alzheimer's disease (AD), which is the most common type of dementia, causes memory loss in the brain and disruption of daily life, especially in elderly individuals. AD is a common type of dementia and neurological disease in which the steps in the progression process that destroy brain cells are critical. This disease causes a decrease in thinking, memory, and behavioral functions, and symptoms appear gradually with age. The transition between the stages of the disease can take a long time [1]. The disease has profound physical and psychological effects on individuals, their families, and their social environments [2]–[5]. As population growth slows down and the elderly population gradually increases throughout the world, especially in developed countries, the number of Alzheimer's patients is increasing, and it is predicted that it will increase annually. Fig. 1 and 2 also contain information on the two patient populations. Although many clinical studies continue to be conducted worldwide, no treatment has yet been provided to stop the disease [6]. Fig. 1 shows the distribution of patients by age. We observe that the incidence of the disease increases with advancing age. It should not be forgotten that one of the determining criteria here is that not all individuals live to the age of 85 and above.

When the graph in Fig. 2 is examined, unfortunately, it is predicted that the number of patients will increase every year. Many reasons leading to this result are mentioned in the literature. Cerebral vascular occlusions, brain infections, vitamin deficiencies, excessive alcohol use, brain tumors, active ingredients of some drugs, and metabolic or psychological problems can be listed. Under current conditions, it is not possible to eliminate the disease through the treatment process. As with many diseases, early diagnosis is essential in dementia and Alzheimer's. Currently, only the rate of progression can be slowed down, and patients' relative quality of life can be kept constant. With early diagnosis and starting treatment in the early stages of the disease, significant progress can be made before permanent damage occurs in the brain. Analysis of MRI images is widely used

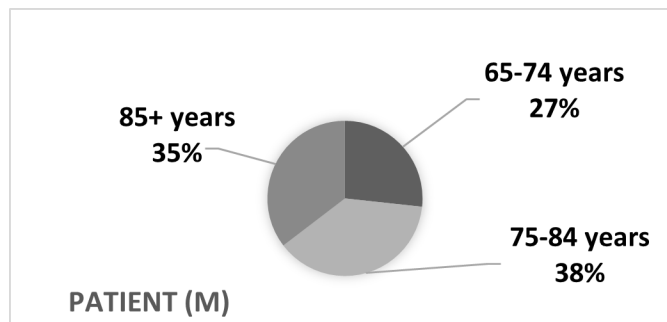


Figure 1: Distribution of patients by age [7]

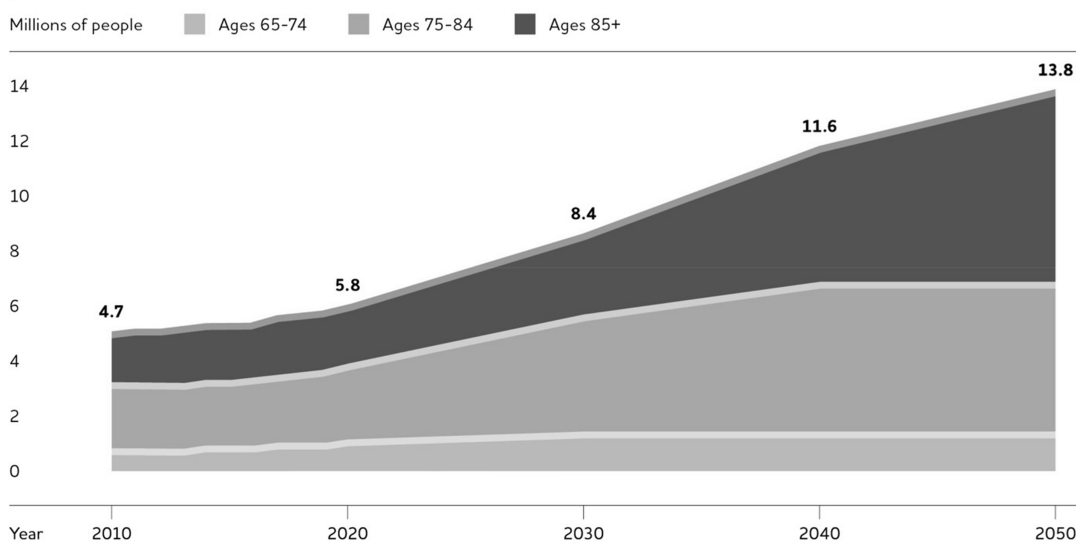


Figure 2: Distribution of patients by age in years [7]

in diagnosing AD [8]. With these analyses, it is possible to determine and classify the stages of the disease. Short information on symptoms and durations depending on the stages of the disease is shown in Fig. 3.

Studies based on traditional machine learning and, especially in recent years, deep learning-based techniques have focused on developing models for detecting physical, anatomical, and functional disorders due to types of dementia and Alzheimer’s disease in the human brain [10]–[16].

The studies started by making binary classification, which is the basis of classification. Binary classification is a method that produces one of two outputs for input data. Binary classification is divided into positive class and negative class. These are “1” and “0”. For this reason, the classification process was carried out by grouping the data groups labeled as very mild demented, mild demented, and moderate demented among the classes in the data set as non-demented, which is at risk of disease, and the data as healthy. There are approaches applied for similar datasets in the literature [3], [17], [18].

In their approach, Nguyen et al. aimed to investigate the ability to detect AD during the first visit of patients with suspected Alzheimer’s disease. For this reason, they stated that all the data used for the test included only the initial and first visit scans. They used the Extreme Gradient Boosting method with 5-fold cross-validation. They achieved an average AUC of %100 during training and %96 in testing. They evaluated machine learning methods from a temporal perspective. They tried to prioritize the prediction of the 3D-ResNet model through the heat map [19].

Venugopalan et al. study showed that deep models outperformed shallow models, including support vector machines, decision trees, random forests, and k-nearest neighbors, by using the AD neuroimaging initiative (ADNI) dataset. Integrating multimodal data outperforms single-mode models in terms of performance evaluation criteria (accuracy, precision, recall, and average F1 scores). It is seen that approximately %88 success was achieved in the analyses made with the proposed method [20]

Ahmed et al. examined both the left and right hippocampus regions on MRI images. They analyzed feature extraction and softmax cross-entropy in convolution neural network (CNN) structures in their study. The analyses used the Gwangju Alzheimer and Related Dementia (GARD) cohort dataset from the National Dementia Research Center (GARD) in Gwangju, South Korea. The results obtained achieved an accuracy of %88 [10].

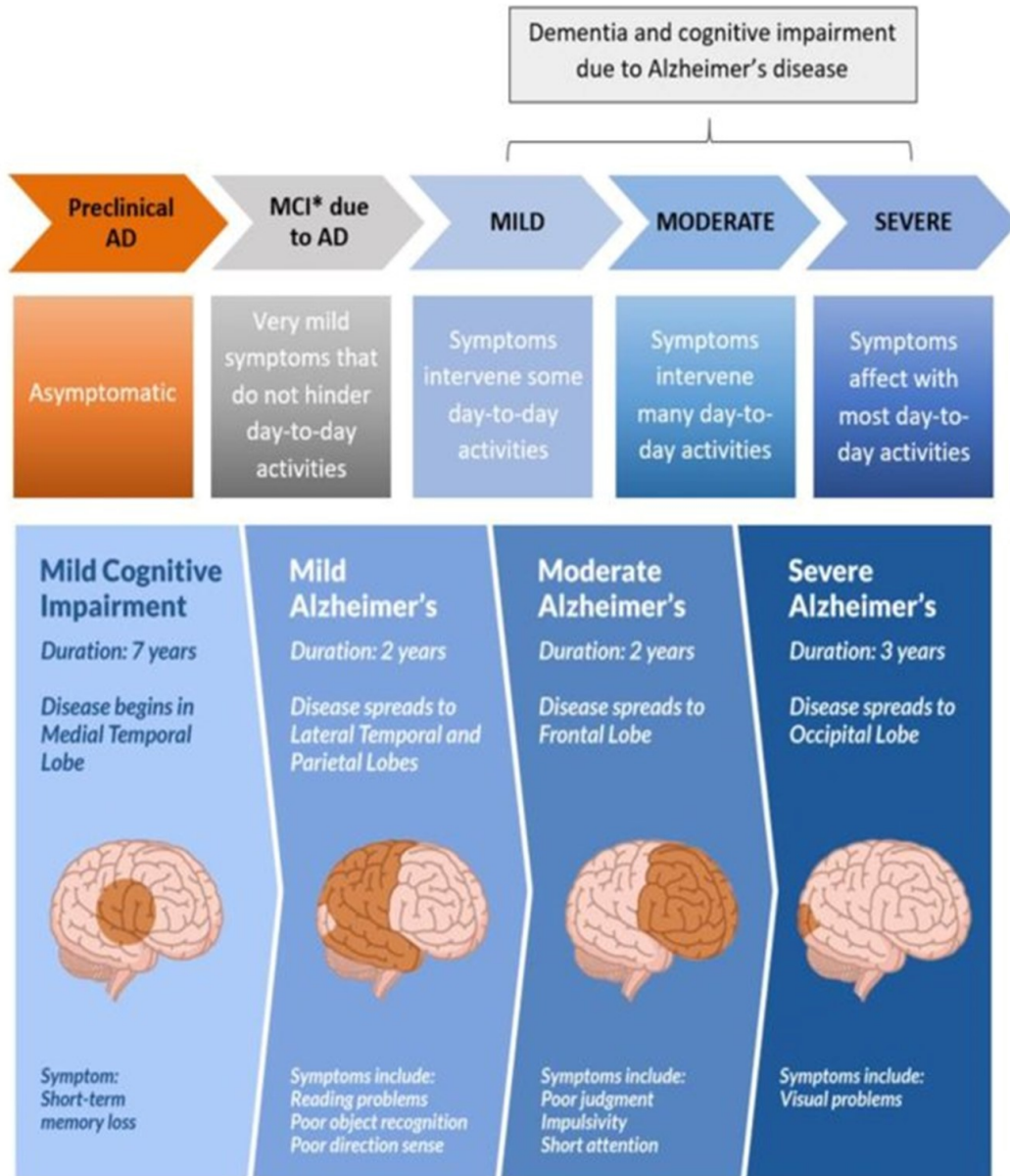


Figure 3: Changes caused by Alzheimer's disease in the brain and its [9]

In this study, dementia levels, including Alzheimer's, were classified with different CNN architectures using MRI data. The study is constructed as follows: Section II presents information about the dataset containing MRI images frequently used in the diagnosis of dementia and Alzheimer's disease and the CNN methods applied to it. Section III includes the data obtained from the analysis and discusses the data in question. The section mentions conclusions and predictions for future studies, which are given in Section IV.

2 Materials

The dataset used in the study was obtained from Kaggle [21]. The dataset contains 6400 MRI images. These images contain images of patient groups belonging to 4 different classes. Sample images are shown in Fig. 4. In all steps carried out within the scope of this study, a computer with an Intel i5 processor (2.5 GHz Turbo), four cores and 8 MB memory was used. Software development was done using the Python programming language. All software operations performed in this study used PyCharm 022.2.2 (Professional Edition). Python is a dedicated Python Integrated Development Environment that provides essential tools in various areas. (IDE). Python-based deep learning tools also offer various advantages in biomedical image analysis. These tools offer a powerful ability to understand, analyze, and extract features from complex biomedical data sets. These tools can analyze data from medical imaging devices, classify diseases, and recognize critical anatomical structures. Python-based deep learning tools offer a robust set of tools to obtain more effective, faster, and accurate results in biomedical image analysis.

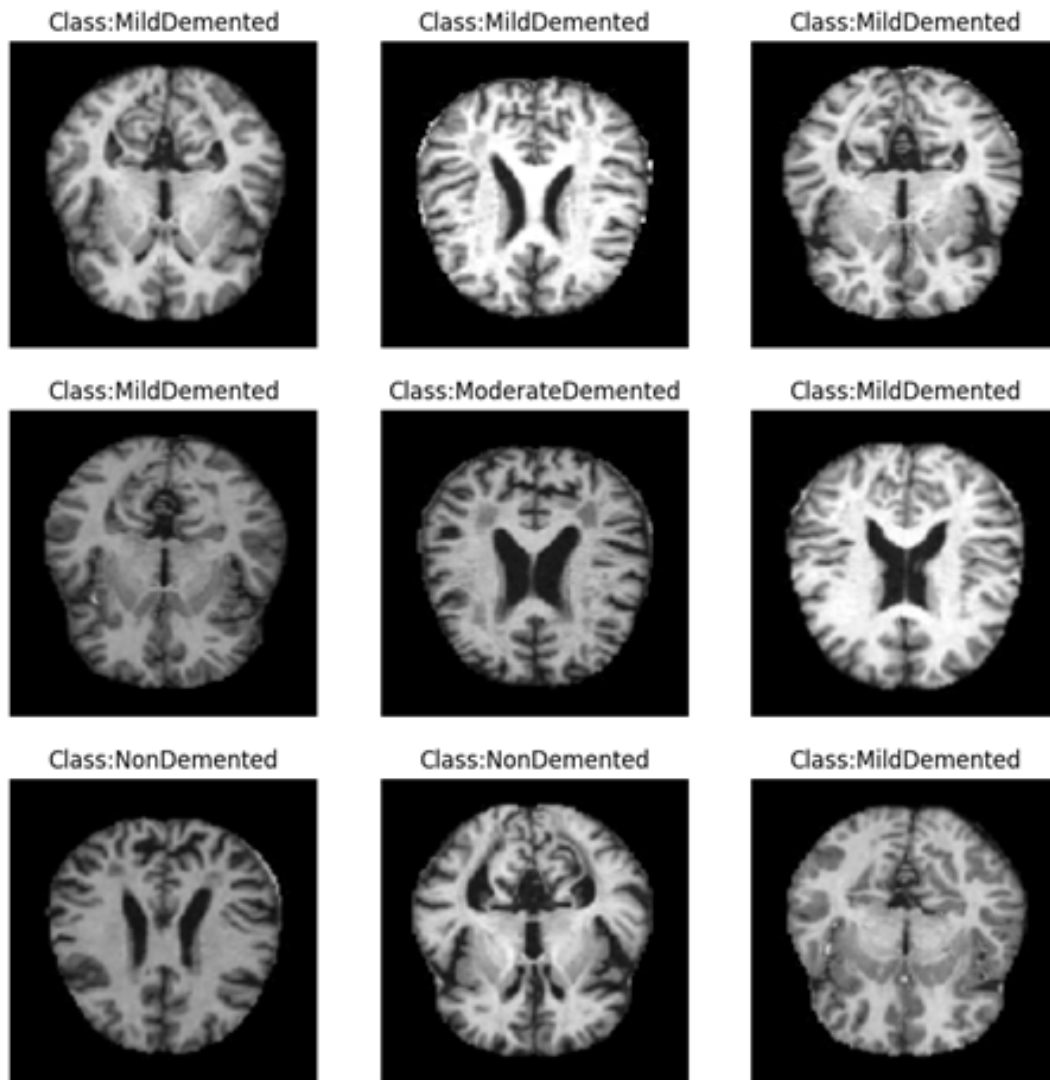


Figure 4: Sample images for different classes

Fig. 5 shows the block diagram of the methodology applied for the multiclass classification of dementia disease. Sub-steps for each step are included in the diagram.

3 Methods

3.1 Convolutional Neural Networks

CNNs are deep learning models that have been successfully used in visual data analysis tasks such as computer vision, image recognition, and processing. They have been shown to be very effective in detecting patterns and features in images, especially in studies. The layers of CNN and their properties are summarized below.

- **Convolutional Layers:** Convolutional layers are the basic components that help detect features in the input data (for example, edges, shapes, patterns in images). They perform convolution on the input using filters or kernels. This allows specific patterns and features to be identified. Each convolution layer can contain multiple filters, each used to identify different features. The convolution operation transforms the data into smaller and particularly more representative feature maps.
- **Pooling Layers:** Pooling layers shrink and summarize the feature maps produced by the convolution layers. They usually work with operations such as maximum pooling or average pooling. Reducing the size of feature maps is important to reduce computational cost and sensitivity to translations.
- **Fully Connected Layers:** Fully connected layers are the traditional structures found at the end of the CNN. These layers take a flattened version of the feature maps and are often used for output tasks such as classification or regression.

These layers help to learn higher-level representations of features. CNN's main purpose is to recognize complex features in images or visual data and perform certain tasks (e.g., object recognition, face recognition) using these features. The convolution

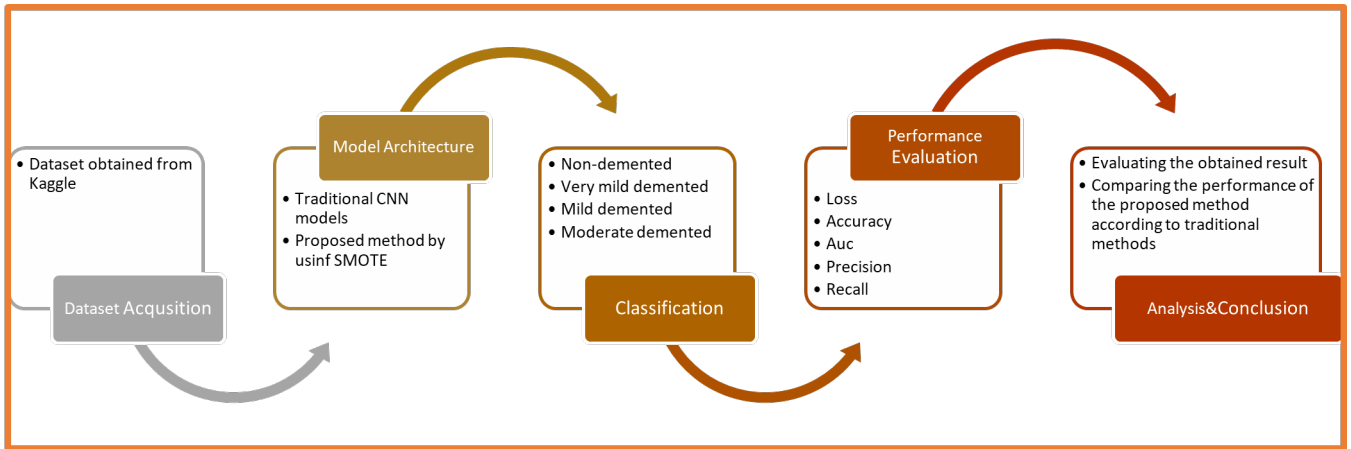


Figure 5: This study flowchart for multi-class classification analysis

and pooling layers help to learn these features in a hierarchical way, while the fully connected layers translate these features into task results. An attractive alternative to training from scratch is fine-tuning a deep network (especially a CNN architecture) via transfer learning. Through transfer learning, these trained networks can be used with smaller datasets by fine-tuning only the fully connected final layers of the CNN. Studies have proven that transfer learning is successful in applications with medical images [22]–[24].

The performance of traditional approaches was measured using the pre-trained network architectures used in the study. Visual geometry group (VGG) architecture based Vgg16, Vgg19, residual network (Resnet) based Resnet50, Resnet101 and mobile network (Mobilenet) based Mobilenet, Mobilenetv2 architectures were used for this study’s analysis. VGG, ResNet, and MobileNet are three important convolutional neural networks that are considered important building blocks in the field of deep learning. They have architectures suitable for different tasks. This text will examine the common and different aspects of these three architectures, focusing on their advantages and application areas.: VGG, ResNet, and MobileNet share convolutional neural network (CNN) principles. This provides specifically designed building blocks for visual recognition, object detection, and classification tasks. Transfer Learning Ability: All three models have a common feature in that they can share pre-trained weights and are suitable for transfer learning applications. This allows them to be used effectively in tasks with limited data.

VGG generally has a simple structure consisting of deep and consecutive layers. ResNet contains blocks spliced together to solve the vanishing gradient problem that occurs in deep networks. MobileNet, on the other hand, offers a lightweight and fast architecture for use in mobile and embedded systems. VGG generally has more parameters and higher computational power. ResNet requires fewer parameters than VGG due to its block structure, which is designed to work more effectively.

MobileNet, on the other hand, is optimized especially for devices with low computing power and storage space. It is designed to provide high performance on mobile devices and embedded systems. The other two generally require larger computational resources and, therefore, have broader application areas.

3.2 Proposed Methods

Table 1 contains the layer information of the proposed CNN architecture. After preprocessing, the input dataset will pass the convolution, dropout, and maximum 2D pooling layers. In the convolution layer, which gives CNN architectures its name, there are several filters (or kernels) whose parameters must be examined as it progresses. The first and second convolution layers consist of 16 filters with a kernel size of 128*128. After the next layer, we apply dropout layers in this model to prevent all neurons from converging toward the same target [25]. We periodically utilize dropout layers to reduce overfitting and increase generalization error in the entire deep neural network with different architectures. Dropout layers are preferred because their generalization performance in many datasets outperforms neural networks that do not use dropouts [26].

The CNN architecture proposed in the study was supported by the Synthetic Minority Over-sampling Technique (SMOTE) approach. Although deep learning is a powerful tool for training complex model structures on large data sets, it may present some challenges, such as unbalanced class distributions. One of several techniques developed to overcome these difficulties is called SMOTE. SMOTE alleviates the problem of class imbalance by creating synthetic instances to empower the minority class. When combined with deep learning, the positive features of SMOTE come to the fore. This approach can help the model generalize better, better represent minority class samples, and avoid overfitting. It can also optimize the performance of deep learning models by increasing their learning ability, allowing the model to learn rare cases in the minority class better. Therefore, the SMOTE approach in deep learning can be considered an effective strategy to combat class imbalance and improve the model’s overall performance.

Table 1: Proposed model CNN architecture

Model: cnn model Layer (type)	Output size	Parameter numbers
conv2d (Conv2D)	[128 128 16]	448
conv2d_1 (Conv2D)	[128 128 16]	2320
max_pooling2d (MaxPooling2D)	[64 64 16]	0
sequential (Sequential)	[32 32 16]	14016
sequential_1 (Sequential)	[16 16 64]	55680
sequential_2 (Sequential)	[8 8 128]	221952
dropout (Dropout)	[8 8 128]	0
sequential_3 (Sequential)	[4 4 256]	886272
dropout_1 (Dropout)	[4 4 256]	0
flatten (Flatten)	4096	0
sequential_4 (Sequential)	512	2099712
sequential_5 (Sequential)	128	66176
sequential_6 (Sequential)	64	8512
dense_3 (Dense)	4	260

In this study, the hyperparameters were tuned to optimize the performance of the convolutional neural network (CNN) architectures. The learning rate, batch size, and optimizer were systematically adjusted based on performance metrics observed during validation. The Adam optimizer was selected for its efficiency in converging the model during training. A learning rate of 0.001 was chosen after testing multiple configurations, ensuring a balance between convergence speed and performance. The batch size was set to 32, which allowed for efficient use of computational resources while maintaining the stability of the gradient updates. These hyperparameters were fine-tuned through iterative testing to maximize classification accuracy and minimize loss across training and validation datasets. The CNN model was constructed with multiple convolutional layers followed by max-pooling layers to extract spatial features from the input data progressively. The model architecture includes two initial convolutional layers with 16 filters and 3x3 kernel sizes, followed by convolutional blocks with 32, 64, 128, and 256 filters. Each convolutional block is followed by a max-pooling layer to reduce the dimensionality of the feature maps and improve computational efficiency. Dropout layers with a 0.2 dropout rate were employed after the deeper convolutional blocks to prevent overfitting. The fully connected layers included 512, 128, and 64 units, which progressively reduced the dimensionality of the feature vector before the final classification layer. The final output layer, with a softmax activation function, consisted of 4 units corresponding to the four classes in the dataset. This architecture was selected to balance computational efficiency with the need for deep feature extraction and classification accuracy.

4 Results and Discussion

The dataset contains 6400 images in total. Images belong to four different classes: 'NonDemented,' 'VeryMildDemented,' 'MildDemented,' and 'ModerateDemented.' The image dimensions were rescaled to 128x128. The parameter numbers used for parameter analysis of the images are given in Table 2.

Table 2: Parameter numbers

Model: Parameter Type	Number
Non-trainable	2368
Trainable	3352980
Total	3355348

When using multi-class classification performance of dementia disease, comparisons were made on five criteria: accuracy rate, the area under the curve, loss, precision, and recall. All tables and visualizations are presented in a way to emphasize these features. Loss is a metric that measures how far a model's predictions are from the actual values during training. The loss function is used to set the parameters of the model. The model tries to minimize the outcome of this function. Common loss functions use cross-entropy calculation. In multiple classification problems, cross-entropy measures the probabilities between multiple classes. Each class has a probability estimate, and the sum of these estimates must be 1.

Accuracy defines the ratio of correctly classified samples to the total number of samples. It is usually expressed as a percentage (%). However, accuracy may be an inadequate performance measure in dataset situations with unbalanced class distribution.

AUC generally refers to the area under the ROC (Receiver Operating Characteristic) curve. This curve shows the change of false positive rate (FPR) with response value, while it shows the change of true positive rate (TPR). AUC takes a value between 0 and 1. An AUC value closer to 1 indicates better classification performance of the model.

Precision refers to the ratio of samples predicted as positive to those that are positive. It aims to reduce the number of false positives, which are cases where true negatives are incorrectly predicted as positives. Precision measures how much of the samples classified as true positives are correctly predicted as positive. It aims to ensure that the model does not miss all instances of positives. False negatives are cases where true positives are incorrectly predicted as negatives.

The proposed model compares transfer learning by employing pre-trained CNN architectures, specifically VGG16, VGG19, ResNet50, and MobileNet. During transfer learning, the convolutional layers of the pre-trained models were frozen, preserving

the weights learned from extensive datasets like ImageNet. Only the fully connected layers at the end of the model were fine-tuned to adapt to the Alzheimer’s dataset. This approach capitalizes on the general feature extraction capabilities of the pre-trained models while allowing for specialization in the final layers. The fine-tuning process involved adjusting the weights of the last few layers to better represent the characteristics of the MRI images used for dementia classification, enhancing the model’s ability to differentiate between the various stages of the disease.

In the first experiment, classification was applied using the data of non-demented and three-stage demented individuals. Pre-trained network architectures were used for this analysis. Results are obtained using this method, which is shown in Table 3..

Table 3: Traditional pre-trained networks classification result for four classes.

	Vgg16	Vgg19	Resnet 50	Resnet 101	Mobilenet	Mobilenetv2
Loss	0.7175	0.7000	0.8709	0.8767	1.2799	1.8565
Accuracy	0.6873	0.6919	0.6231	0.6067	0.6719	0.6489
AUC	0.9065	0.9121	0.8630	0.8626	0.8798	0.8481
Precision	0.7312	0.7193	0.6811	0.6493	0.6830	0.6551
Recall	0.6145	0.6411	0.4926	0.5152	0.6740	0.6474

VGG19 architecture has a very deep network structure and a wide learning capacity. This increases the network’s ability to learn more complex features and relationships. When dealing with a complex and multidimensional problem such as Alzheimer’s disease, this depth appears to allow the extraction of high-level features and these features to classify disease levels more accurately. VGG19 architecture can provide better results than other pre-trained network architectures as it can better extract feature maps using smaller filter sizes and consecutive convolution layers, ensuring that the features derived from previous layers represent lower-level and general features. In addition, with the transfer learning advantage, it can be said that VGG19 is an architecture with better generalization ability since it has been trained on a large dataset before. The VGG19 architecture includes various convolution layers and fully connected layers, resulting in more parameters in the model’s learning process. This allows the model to gain more flexibility and better adapt to the data set. These aspects can explain why the approaches performed can perform better.

The model, which started with Conv2D layers, captured the spatial relationships in the input data. In these layers, feature maps were created through filters and essential patterns and building blocks in the data were detected. Conv2D layers performed deep feature extraction using different filter numbers and kernel sizes. After these convolution layers, the MaxPooling2D layer was added. The MaxPooling2D layer reduced the computational load of the model by performing dimensionality reduction and selecting the most significant information in the feature maps. With this layer, the complexity of the model was kept under control, and overfitting was prevented during the learning process. In addition, multiple Sequential layers were used in the model to efficiently organize the layers and optimize their interactions with each other. Sequential layers were formed by the combination of layers added in a certain order, and this structure was intended to increase the modularity and reusability of the model. Dropout layers were strategically placed to prevent over-learning of the model and to increase its overall performance. In these layers, certain neurons were randomly disabled during training, making the model more robust and generalizable. A flatten layer was used to combine and flatten the features. Multidimensional feature maps obtained from the flatten layer and convolution layers were converted to a one-dimensional vector and transferred to fully connected layers. The model classification process was performed with Dense layers. In Dense layers, learned features were used to increase the classification performance and it was concluded whether there was Alzheimer’s in the output layer.

Callback mechanisms such as early stopping and learning rate reduction were incorporated into the model’s training process to prevent overfitting and ensure optimal training performance. Early stopping was used to monitor the validation accuracy, halting the training if no significant improvement was observed after a patience threshold of five epochs. This strategy helped mitigate overfitting by ensuring that the model did not continue training beyond the point of diminishing returns. Additionally, a dynamic learning rate adjustment mechanism was implemented, reducing the learning rate when the validation accuracy plateaued. These callbacks not only improved the training efficiency but also ensured that the model converged to an optimal solution without unnecessary iterations, thereby enhancing the overall performance and generalizability of the model.

Callbacks were used in the model implemented using the proposed architecture. Callbacks are functions that are called when certain events or conditions occur during training. They can perform a few tasks, such as controlling the model’s training, preventing overfitting, adjusting the training pace, or performing different functions. Early stopping and learning rate adjustment methods were used in this study. Early stopping is a standard callback used to prevent the model from being overfitting. If a particular metric (for example, accuracy) does not improve during training, it can automatically stop training. Learning rate is a vital hyperparameter that determines the training speed. Adjusting the learning rate during training enables faster or slower learning. In this way, an attempt was made to reduce the possibility that the results obtained from the model would be misleading. The callback parameters used in the study are shown in Table 4.

Fig. 6 visualizes the model’s success rates during the training process and its performance on the validation set. The achievements without the SMOTE method support the robustness and general applicability of the deep learning-based dementia classification model, highlighting the model’s ability to deal with the minority class in the dataset.

Table 4: Callback parameters values

Callback parameters	Value
Epoch Number	50
Monitor	Accuracy
Min_delta	0.01
Patience	5
Mode	“max”

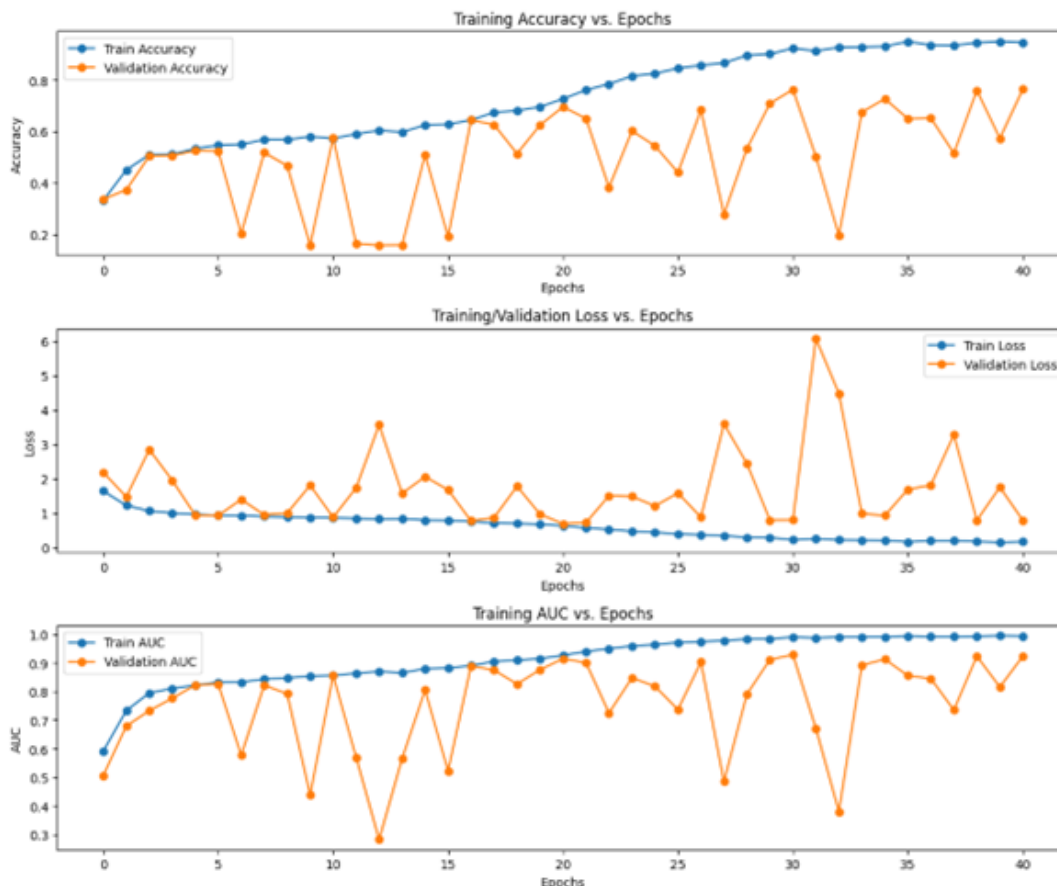


Figure 6: Training without SMOTE algorithm for four classes

The last step of the proposed model is aimed at preventing the imbalance between the data by using the SMOTE algorithm and reducing the error rates by increasing the inter-class predictive ability of the model. SMOTE algorithm was applied to eliminate data imbalance. The purpose of using this algorithm is to eliminate the imbalance of the dataset by ensuring that all classes contain equal numbers of data. With this approach, the number of data was 12800. The graphics are given in Fig. 7 in the analysis, and the test size was determined to be 0.2.

SMOTE was applied to address the inherent class imbalance in the dataset. SMOTE creates synthetic samples for the minority classes, thus increasing their representation within the dataset. This method was critical in enhancing the model’s ability to generalize to minority classes, such as "Moderate Demented" and "Very Mild Demented," which were underrepresented in the original dataset. The SMOTE algorithm was applied before model training, and its effects were evident in the improved classification metrics, particularly in precision and recall for the minority classes. By balancing the dataset, the model could learn more robust feature representations for all classes, ultimately leading to a more reliable classification performance across the board.

Since the transition between phases of the disease and knowing which stage the patient is at the time of diagnosis are essential, the classification was first made for very mildly demented, mildly demented, and moderately demented classes. The results obtained for the four-class and three-class classification problems are shown in Table 5. and Table 6., respectively.

However, when the results obtained from three-class and four-class analyses are evaluated together, classification ability decreases as the number of classes increases and the nature of the added data changes. The values obtained in the four-class results are worse for all criteria than the three. Information about the literature studies is shown using the same dataset in Table 7.

The contrastive learning method used by Shu et al. [27] provided an accuracy rate of %92. This rate is considerably higher

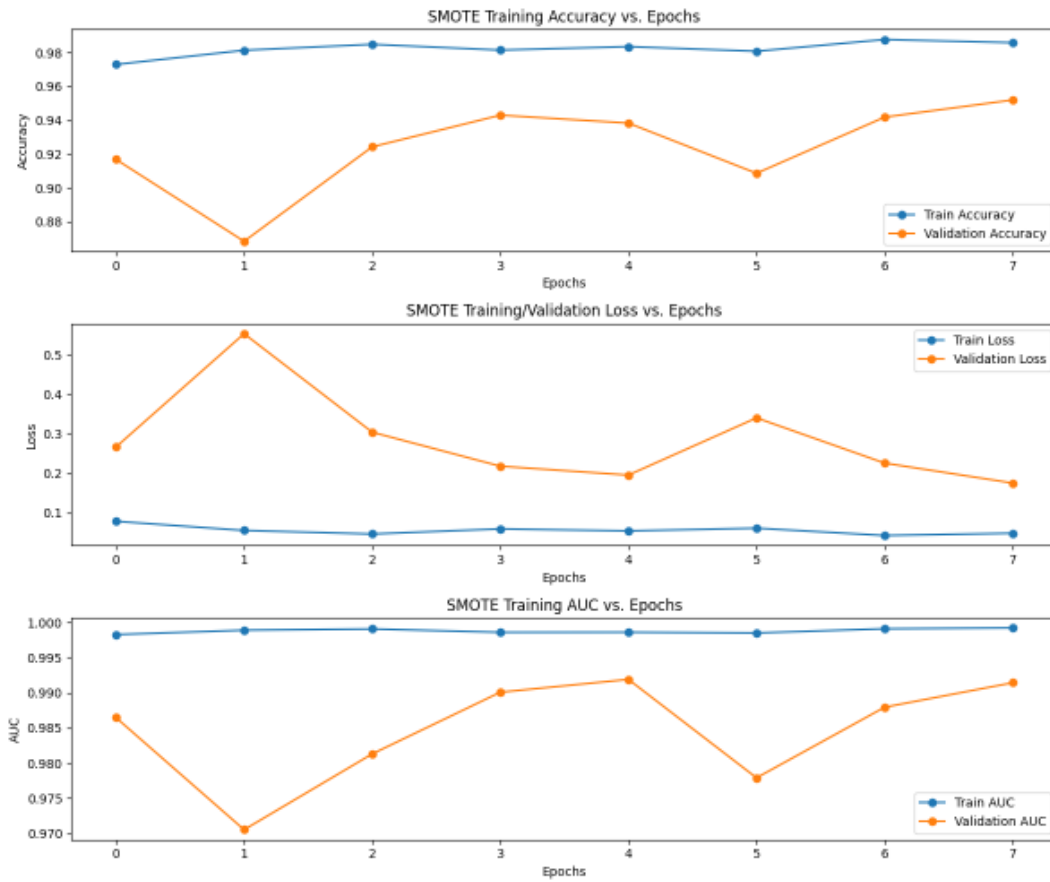


Figure 7: Training without SMOTE algorithm for four classes

Table 5: Results for multiclass classification for four classes

	Without SMOTE Model	SMOTE Model
Loss	0.7870	0.175
Accuracy	0.7641	0.9520
AUC	0.9236	0.9914
Precision	0.7674	0.9519
Recall	0.7602	0.9512

Table 6: Results for multiclass classification for three classes

	Without SMOTE Model	SMOTE Model
Loss	0.7684	0.9341
Accuracy	0.7011	0.7500
AUC	0.8309	0.8998
Precision	0.7011	0.7547
Recall	0.7011	0.7485

than the 70.%30 accuracy rate obtained by Mggdadi et al. [28] using the VGG16-based 2D CNN. In the study conducted by Ajagbe et al. [29], %71.02 and %77.66 accuracy rates were achieved with the VGG16 and VGG19 models, respectively, which shows that different CNN configurations can create significant differences in terms of performance. In this study, it is seen that similar results are obtained when the traditional methods in question are applied.

The DEMNET model proposed by Murugan et al. [30] reveals that special network configurations can be effective. In another study, conducted with AlexNet and ResNet-based models, the AlexNet + SVM combination stood out with an accuracy rate of %94.80 [31]. It shows that integrating traditional machine learning algorithms such as SVM with deep learning models can improve performance. The hybrid CNN model proposed by Techa et al. [32] and including DenseNet196, VGG16 and ResNet50, achieved an accuracy rate of %89. Sharma et al. [34] emphasize that transfer learning can be a powerful tool in Alzheimer’s detection with %94.92 accuracy using the Transfer learning and Inception model. When the results are examined for proposed method, it is shown that the model’s errors during training have significantly decreased, and it has undergone a better learning process. While the accuracy rate of the model before SMOTE was applied was %76.41, this rate increased to %95.20 after SMOTE was applied. This increase shows that the SMOTE method has significantly increased the model’s overall

Table 7: Literature summary for the same dataset

Reference	Method	Year	Accuracy (%)
Shu et al. [27]	Contrastive learning	2018	92.00
Mggdadi et al. [28]	2D CNN	2021	67.50
	VGG16	2021	70.30
Ajagbe et al. [29]	CNN	2021	71.02
“	VGG16	2021	77.04
“	VGG19	2021	77.66
Murugan et al. [30]	DEMNET(Dementia Networks)	2021	95.23
Mohammed et al. [31]	AlexNet	2021	92.20
	ResNet	2021	93.10
	AlexNet+SVM	2021	94.80
	ResNet-50+SVM	2021	94.10
Techa et al. [32]	A proposed convolution neural network (included DenseNet196, VGG16 and ResNet50)	2022	89.00
Sharma et al. [33]	Transfer learning, SVM, and permutation based machine learning	2022	91.75
Sharma et al. [34]	Transfer based Inception model	2022	94.92
Hussain et al. [35]	Random Forest	2023	91.25
	SVM	2023	80.70
	CNN	2023	93.96
Proposed method*	With SMOTE (three classes)	2024	75.00
“	With SMOTE (four classes)	2024	95.20

performance. The AUC value was %92.36 before SMOTE was applied, while it became %99.14 after SMOTE was applied. This shows that the classification ability of the model has been significantly improved with SMOTE and provides more reliable results. It shows that the model's ability to catch true positives has increased and produces fewer false negative results. This study aims to contribute to the literature by including a more comprehensive classification framework targeting the stages of dementia. While focusing on the binary or quadruple-class classification of Alzheimer's diagnosis using machine learning and deep learning models, this study applied a three- and four-class classification to guide decision-makers in making decisions about stage transitions and to provide a similar contribution to the initial diagnosis. Although the proposed method shows lower accuracy in the three-class classification than the four-class one, it highlights the importance of correctly defining different disease stages. This finer level of detail can provide valuable clinical insights not emphasized in previous studies that focused mainly on broader classifications. It offers potential benefits for more detailed diagnostic processes to improve patient care.

In this part, let's briefly summarize the restrictive reasons and performance criteria. A research limitation is that the data set used in the analysis cannot be tested on real data. In addition to this situation, the long duration of the analyses can be considered another limiting factor.

5 Conclusions

This research presented multiple classifications of medical images of Alzheimer's disease with the proposed CNN, VGG16, VGG19, Resnet50, Resnet101, Mobilenet, and Mobilenetv2 and demonstrated that deep convolutional neural network approaches for multiple classifications are possible.

This study aims to contribute to developing effective treatment strategies for the current stage by focusing on the classification of different dementia stages, including Alzheimer's disease, by using CNN architectures, providing early diagnosis and stage determination of the disease. MRI is the most critical imaging method that contributes to this process. The results show that new approaches reinforced CNN architectures as a powerful tool for diagnosing and classifying dementia levels. In this study, MRI images containing three and four different classes were classified using different deep learning architectures. The performance of the obtained classification results was compared through metrics. The study obtained the highest classification performance using the proposed method. The proposed method achieved the best performance regarding accuracy, area under the curve, loss, recall, and precision. VGG-19 closely followed it, while Resnet 50 had a lower performance.

When the results obtained for the CNN architecture were compared, it was seen that the dimensionality reduction and feature acquisition methods applied in the study were effective in detecting dementia levels through MRI images. In subsequent studies, the performances of different CNN architectures and the features obtained from these architectures can be evaluated in classical classifiers to detect dementia levels. Performance evaluations of hybrid models can be made by combining new architectures with classical methods. It is envisaged that this study will provide a basis for future studies based on image analysis and that approaches can be used to reduce the mentioned limitations.

Ethical Declarations

The dataset used in the study is a dataset that has been previously used in the literature and is published publicly. Access link:<https://www.kaggle.com/datasets/tourist55/alzheimers-dataset-4-class-of-images>

Authors' Contributions

Iclal Cetin Tas: Conceptualization, Methodology, Writing - original draft, Data, Software. Murat Simsek: Data curation, Software, Writing - original draft.

Competing Interests

The authors have no conflict of interest to report.

References

- [1] S. Al-Shoukry, T. H. Rassem, and N. M. Makbol, "Alzheimer's diseases detection by using deep learning algorithms: A mini-review," *IEEE Access*, vol. 8, pp. 77 131–77 141, 2020.
- [2] A. W. Salehi, P. Baglat, B. B. Sharma, G. Gupta, and A. Upadhyay, "A CNN Model: Earlier Diagnosis and Classification of Alzheimer Disease using MRI," in *Proceedings - International Conference on Smart Electronics and Communication, ICOSEC 2020*, 2020.
- [3] W. Salehi, P. Baglat, G. Gupta, S. B. Khan, A. Almusharraf, A. Alqahtani, and A. Kumar, "An Approach to Binary Classification of Alzheimer's Disease Using LSTM," *Bioengineering 2023, Vol. 10, Page 950*, vol. 10, no. 8, p. 950, aug 2023.
- [4] E. Hanbay and A. Ari, "Özel Blok Yapıları Kullanarak Tasarlanan Derin Öğrenme Mimarileri ile Alzheimer Hastalık Tespiti," *Firat Üniversitesi Mühendislik Bilimleri Dergisi*, vol. 35, no. 2, pp. 745–752, sep 2023.
- [5] K. Aderghal, A. Khvostikov, A. Krylov, J. Benois-Pineau, K. Afdel, and G. Catheline, "Classification of Alzheimer Disease on Imaging Modalities with Deep CNNs Using Cross-Modal Transfer Learning," *Proceedings - IEEE Symposium on Computer-Based Medical Systems*, vol. 2018-June, pp. 345–350, jul 2018.
- [6] M. Ü. ÖZİÇ and S. ÖZŞEN, "3B Alzheimer MR Görüntülerinin Hacimsel Kayıp Bölgelerindeki Voksel Değerleri Kullanılarak Sınıflandırılması," *El-Cezeri Fen ve Mühendislik Dergisi*, 2020.
- [7] "Alzheimer's Facts and Figures Report | Alzheimer's Association." [Online]. Available: <https://www.alz.org/alzheimers-dementia/facts-figures>
- [8] Y. Eroglu, M. Yildirim, and A. Cinar, "mRMR-based hybrid convolutional neural network model for classification of Alzheimer's disease on brain magnetic resonance images," *International Journal of Imaging Systems and Technology*, vol. 32, no. 2, 2022.
- [9] S. Dan, D. Sharma, K. Rastogi, Shaloo, H. Ojha, M. Pathak, and R. Singhal, "Therapeutic and diagnostic applications of nanocomposites in the treatment Alzheimer's disease studies," *Biointerface Research in Applied Chemistry*, vol. 12, no. 1, pp. 940–960, feb 2022.
- [10] S. Ahmed, K. Y. Choi, J. J. Lee, B. C. Kim, G. R. Kwon, K. H. Lee, and H. Y. Jung, "Ensembles of Patch-Based Classifiers for Diagnosis of Alzheimer Diseases," *IEEE Access*, vol. 7, pp. 73 373–73 383, 2019.
- [11] D. Shen, C. Y. Wee, D. Zhang, L. Zhou, and P. T. Yap, "Machine learning techniques for AD/MCI diagnosis and prognosis," *Intelligent Systems Reference Library*, vol. 56, pp. 147–179, 2014.
- [12] Y. Wang, M. Liu, L. Guo, and D. Shen, "Kernel-based multi-task joint sparse classification for Alzheimer'S disease," *Proceedings - International Symposium on Biomedical Imaging*, pp. 1364–1367, 2013.
- [13] J. Escudero, J. P. Zajicek, and E. Ifeachor, "Machine Learning classification of MRI features of Alzheimer's disease and mild cognitive impairment subjects to reduce the sample size in clinical trials," *Proceedings of the Annual International Conference of the IEEE Engineering in Medicine and Biology Society, EMBS*, pp. 7957–7960, 2011.
- [14] A. Ortiz, J. M. Górriz, J. Ramírez, and F. J. Martínez-Murcia, "LVQ-SVM based CAD tool applied to structural MRI for the diagnosis of the Alzheimer's disease," *Pattern Recognition Letters*, vol. 34, no. 14, pp. 1725–1733, oct 2013.
- [15] S. T. Yang, J. D. Lee, T. C. Chang, C. H. Huang, J. J. Wang, W. C. Hsu, H. L. Chan, Y. Y. Wai, and K. Y. Li, "Discrimination between Alzheimer's disease and mild cognitive impairment using SOM and PSO-SVM," *Computational and Mathematical Methods in Medicine*, vol. 2013, 2013.
- [16] K. R. Gray, P. Aljabar, R. A. Heckemann, A. Hammers, and D. Rueckert, "Random forest-based similarity measures for multi-modal classification of Alzheimer's disease," *NeuroImage*, vol. 65, pp. 167–175, jan 2013.
- [17] A. B. Tufail, Y. K. Ma, and Q. N. Zhang, "Binary Classification of Alzheimer's Disease Using sMRI Imaging Modality and Deep Learning," *Journal of Digital Imaging*, vol. 33, no. 5, pp. 1073–1090, oct 2020.
- [18] R. Prajapati, U. Khatri, and G. R. Kwon, "An Efficient Deep Neural Network Binary Classifier for Alzheimer's Disease Classification," *3rd International Conference on Artificial Intelligence in Information and Communication, ICAIIC 2021*, pp. 231–234, apr 2021.
- [19] D. Nguyen, H. Nguyen, H. Ong, H. Le, H. Ha, N. T. Duc, and H. T. Ngo, "Ensemble learning using traditional machine learning and deep neural network for diagnosis of Alzheimer's disease," *IBRO Neuroscience Reports*, vol. 13, pp. 255–263, dec 2022.
- [20] J. Venugopalan, L. Tong, H. R. Hassanzadeh, and M. D. Wang, "Multimodal deep learning models for early detection of Alzheimer's disease stage," *Scientific Reports 2021 11:1*, vol. 11, no. 1, pp. 1–13, feb 2021.
- [21] "Alzheimer's Dataset (4 class of Images) | Kaggle." [Online]. Available: <https://www.kaggle.com/datasets/tourist55/alzheimers-dataset-4-class-of-images>
- [22] M. Hon and N. M. Khan, "Towards Alzheimer's disease classification through transfer learning," *Proceedings - 2017 IEEE International Conference on Bioinformatics and Biomedicine, BIBM 2017*, vol. 2017-January, pp. 1166–1169, dec 2017.
- [23] J. Plested and T. Gedeon, "Deep transfer learning for image classification: a survey."
- [24] J. Yosinski, J. Clune, Y. Bengio, and H. Lipson, "How transferable are features in deep neural networks?" *Advances in Neural Information Processing Systems*, vol. 4, no. January, pp. 3320–3328, nov 2014.
- [25] "Classification of Alzheimer ' s disease subjects from MRI using hippocampal visual features To cite this version : HAL Id : hal-00993379," *Computerized Medical Imaging and Graphics*, vol. 44, no. 1, 2015.
- [26] J. Brownlee, "A Gentle Introduction to Dropout for Regularizing Deep Neural Networks," 2018.
- [27] F. Shu and L. Tian, "Deep Learning Methods for Alzheimer's Disease Prediction Project Category: Computer Vision."
- [28] E. Mggdadi, A. Al-Aiad, M. S. Al-Ayyad, and A. Darabseh, "Prediction Alzheimer's disease from MRI images using deep learning," in *2021 12th International Conference on Information and Communication Systems, ICICS 2021*, 2021.
- [29] S. A. Ajagbe, K. A. Amuda, M. A. Oladipupo, O. F. AFE, and K. I. Okesola, "Multi-classification of alzheimer disease on magnetic resonance images (MRI) using deep convolutional neural network (DCNN) approaches," *International Journal of Advanced Computer Research*, vol. 11, no. 53, 2021.
- [30] S. Murugan, C. Venkatesan, M. G. Sumithra, X. Z. Gao, B. Elakkiya, M. Akila, and S. Manoharan, "DEMNET: A Deep Learning Model for Early Diagnosis of Alzheimer Diseases and Dementia from MR Images," *IEEE Access*, vol. 9, pp. 90 319–90 329, 2021.
- [31] B. A. Mohammed, E. M. Senan, T. H. Rassem, N. M. Makbol, A. A. Alanazi, Z. G. Al-Mekhlafi, T. S. Almurayziq, and F. A. Ghaleb, "Multi-Method Analysis of Medical Records and MRI Images for Early Diagnosis of Dementia and Alzheimer's Disease Based on Deep Learning and Hybrid Methods," *Electronics 2021, Vol. 10, Page 2860*, vol. 10, no. 22, p. 2860, nov 2021.
- [32] C. Techa, M. Ridouani, L. Hassouni, and H. Anoun, "Alzheimer's Disease Multi-class Classification Model Based on CNN and StackNet Using Brain MRI Data," *Lecture Notes on Data Engineering and Communications Technologies*, vol. 152, pp. 248–259, 2023.
- [33] S. Sharma, S. Gupta, D. Gupta, A. Altameem, A. K. J. Saudagar, R. C. Poonia, and S. R. Nayak, "HTLML: Hybrid AI Based Model for Detection of Alzheimer's Disease," *Diagnostics*, vol. 12, no. 8, 2022.

- [34] S. Sharma, S. Gupta, D. Gupta, S. Juneja, A. Mahmoud, S. El-Sappagh, and K. S. Kwak, "Transfer learning-based modified inception model for the diagnosis of Alzheimer's disease," *Frontiers in Computational Neuroscience*, vol. 16, 2022.
- [35] M. G. Hussain and Y. Shiren, "Identifying Alzheimer Disease Dementia Levels Using Machine Learning Methods," *Medical Research Archives*, vol. 11, no. 7.1, nov 2023.